

A Nano-Tensile Testing System for Studying Nanostructures inside an Electron Microscope: Design, Characterization and Application

THÈSE N° 4605 (2010)

PRÉSENTÉE LE 1^{ER} MARS 2010

À LA FACULTÉ SCIENCES ET TECHNIQUES DE L'INGÉNIEUR
LABORATOIRE DE SYSTÈMES ROBOTIQUES 2
PROGRAMME DOCTORAL EN SYSTÈMES DE PRODUCTION ET ROBOTIQUE

ÉCOLE POLYTECHNIQUE FÉDÉRALE DE LAUSANNE

POUR L'OBTENTION DU GRADE DE DOCTEUR ÈS SCIENCES

PAR

Dongfeng ZHANG

acceptée sur proposition du jury:

Prof. M.-O. Hongler, président du jury
Prof. R. Clavel, Dr J. Michler, directeurs de thèse
Dr J.-M. Breguet, rapporteur
Prof. H. Shea, rapporteur
Prof. U. Staufer, rapporteur



ÉCOLE POLYTECHNIQUE
FÉDÉRALE DE LAUSANNE

Suisse
2010

Abstract

Mechanical properties of nanostructures could be remarkably different from their bulk counterparts owing to scale effects, which have attracted considerable research interest in recent years. However, nanomechanics studies are hindered by the difficulties of conducting well-instrumented mechanical testing. The objective of this thesis is to develop a novel tensile stage that can be used to probe mechanical properties of universal one-dimensional (1D) nanostructures, like nanowires and nanotubes, inside a scanning/transmission electron microscope (SEM/TEM).

The main challenges of performing tensile tests at the nanoscale are: (1) specimen alignment and fixation on the tensile stage; (2) application and measurement of tensile force with nano-Newton resolution; (3) measurement of specimen elongation with nanometer resolution. Previous studies have shown that micro-electromechanical system (MEMS) technology combined with advanced microscopy (e.g. SEM and TEM) provides promising perspectives to address these challenges.

Two types of nano-tensile stages, fabricated in a silicon on insulator (SOI) wafer, were developed in this thesis, which consisted of a comb-drive actuator and either a differential capacitive force sensor or a double clamped beam force sensor. The optimized comb-drive actuators could output an in-plane force of about 210 μN at a drive voltage of 120 V, and the force sensors achieved resolutions of better than 50 nN. Individual 1D nanostructures were placed on the MEMS device by *in-situ* nanomanipulations and fixed at their two ends via focused electron beam induced deposition (FEBID). A strategy of modifying device topography, e.g. in the form of trenches or pillars, was proposed to facilitate the specimen preparation by *in-situ* manipulation that could achieve a high yield of about 80%. The mechanical testing function of the developed micro devices was demonstrated by tensile tests on individual Co and Si nanowires (NWs) inside an SEM. The average apparent Young's modulus, tensile strength and fracture strain of the electrochemically deposited Co NWs were measured to be (75.3 ± 14.6) GPa, (1.6 ± 0.4) GPa and (2.2 ± 0.6) %, respectively. The measured Young's modulus is significantly lower than that of Co in the bulk form (209 GPa), which is likely caused by structural defects (e.g. pores) and surface effects (e.g. surface contaminations and surface oxide layers). The phosphorous-doped SiNWs grown bottom up by the vapor-liquid-solid (VLS) technique showed an average Young's modulus of (170.0 ± 2.4) GPa and a tensile strength larger than 8.3 GPa. This finding confirms that materials strength increases as their sizes scale down. The top down electroless chemically etched Si $\langle 100 \rangle$ NWs show a tensile strength of 5.4 GPa.

The developed MEMS devices and experimental techniques enable an alternative way of *in-situ* nanomechanical characterization based on electron microscopy. The design methodology and learning presented in this thesis would be useful to develop nano-tensile stages of other configurations with more advanced functions.

Keywords: Nanomechanics, MEMS, tensile test, nanostructure, comb drive, capacitive sensor, in-situ, electron microscope.

This page intentionally left blank

Version abrégée

Les propriétés mécaniques de structures nanométriques peuvent être très différentes de leurs analogues à plus grande échelle. Ce phénomène a engendré beaucoup d'intérêt dans la recherche ces dernières années. Cependant, l'étude de la nano-mécanique est freinée par les difficultés d'effectuer de bons tests avec des instruments appropriés. L'objectif de cette thèse est de concevoir et mettre en oeuvre une nouvelle plateforme d'essai de traction utile pour tester les propriétés mécaniques de structures nanométriques universelles à une dimension, ex.: nano-fils et nano-tubes, à l'intérieur d'un microscope électronique à balayage (MEB) ou à transmission (MET).

Les principaux défis pour faire des essais de traction standards à une échelle nanométrique sont : (1) aligner l'échantillon et le fixer sur la platine d'essai de traction; (2) appliquer et mesurer des forces de traction avec une résolution de l'ordre du nano-Newton; (3) mesurer l'allongement de l'échantillon avec une précision nanométrique. Les études précédentes ont montré que la technologie des systèmes micro-électromécaniques (MEMS) combinée avec des techniques de microscopie avancée (ex.: MEB et MET) fournit des perspectives prometteuses en réponse à ces défis.

Dans cette thèse, deux nouveaux types de plateformes d'essai de traction ont été fabriqués à partir d'un wafer de silicium sur isolant (SOI). Ils consistent en un actuateur « comb-drive » combiné avec un capteur de force ; celui-ci est ou de type capacitif différentiel, ou réalisé par une poutre micro-mécanique travaillant en flexion encastrée à ses deux extrémités. Cet actuateur combiné peut produire des forces dans le plan d'environ 210 μN avec une tension de 120 V. Le capteur de force peut atteindre une résolution meilleure que 50 nN. Des structures nanométriques individuelles à une dimension ont été placées dans l'appareil MEMS par des nano-manipulateurs *in-situ* et fixées à leurs deux extrémités par déposition induite d'un faisceau d'électron concentré (FEBID). Une stratégie pour modifier la topographie de l'appareil a été proposée, par exemple sous la forme de tranchée ou de piliers, dans le but de faciliter la préparation de l'échantillon. Ce procédé permet d'avoir un rendement d'environ 80%. La fonction des tests mécaniques du micro-dispositif développé a été testée par des essais de traction sur des nano-fils de cobalt et de silicium à l'intérieur d'un MEB. La moyenne apparente du module de Young, la résistance à la traction et la rupture de nano-fils de cobalt déposés par électrochimie ont donné les valeurs respectives de (75.3 ± 14.6) GPa, (1.6 ± 0.4) GPa, et (2.2 ± 0.6) %. La valeur mesurée du module de Young est significativement plus basse que celle du cobalt sous forme massive (209 GPa). Ceci est sans doute dû à la présence de défauts structuraux (ex : pores) et des effets de surface (ex : contaminations de surface ou couche d'oxyde en surface). Les nano-fils de silicium dopés au phosphore qui croissent par la technique de vapeur-liquide-solide (VLS) montrent un module de Young moyen de (170.0 ± 2.4) GPa et une résistance à la traction supérieure à 8.3 GPa. Cette valeur est beaucoup plus grande que celle du silicium massif, ce qui confirme que la résistance des matériaux augmente à plus petite échelle. Les nano-fils de silicium produits par attaque chimique, avec un axe aligné avec la direction $\langle 100 \rangle$ d'une plaque de silicium, montrent une résistance à la traction d'environ 5.4 GPa.

L'appareil MEMS et les expériences techniques développées offrent une nouvelle alternative à la caractérisation nano-mécanique MEB/MET *in-situ*. La conception et l'utilisation de la plateforme d'essai de traction nanométrique présentée dans cette thèse sont utiles pour développer d'autres appareils d'essai de traction avec une configuration différente ou avec des fonctions plus avancées.

Mots-clés: nano-mécanique, MEMS, essai de traction, structures nanométriques, actuateur combiné, capteur capacitif, in-situ, microscope électronique.

Acknowledgments

I thank you for your interest in reading this thesis. It would not have been possible without the help and support from several people.

First, I would like to thank Dr. Jean-Marc Breguet for introducing me into this exciting topic, followed by supervision of my work in the first year of my PhD study at EPFL, and for evaluating my thesis as a jury. I am grateful to Dr. Johann Michler for his finally able guidance and advice, for providing me the facilities, and for the freedom and trust granted to me in conducting the work at EMPA. My special gratitude also goes to Prof. Reymond Clavel for supervising my thesis after Jean-Marc's departure from EPFL, for the inspiring discussions on the subject matter and final thesis writing.

I want to thank Prof. Urs Stauer (TU Delft, Netherland) and Prof. Herbert Shea (EPFL) for participating in the jury and evaluating my work, as well as Prof. Max-Olivier Hongler (EPFL) for chairing the jury.

I am thankful to the staff of CMI for their support during the micro fabrication work at EPFL, to Dr. Walter Drissen for the helpful discussions on the device design and calibration experiments, to Dr. Ivo Utke for the assistance and discussions on focused electron/ion beam induced processing, and to Gerhard Bürki for introducing me the electron microscopy and providing assistance during my laboratory work at EMPA. The wire bonding was performed in the Laboratoire de Production Microtechnique (LPM) at EPFL. The tungsten and Pt-Ir tips used in this thesis were fabricated by electrochemical etching with the setup constructed by Dr. Roland Widmer (EMPA). I am grateful to Dr. Xavier Maeder and Dr. Kilian Wasmer (EMPA) for their kind assistances in writing the abstract of this thesis in French. I also acknowledge the support of mechanical workshops and the administrative offices at EMPA and EPFL.

I have had the pleasure to share the office ME B3435 (EPFL) and L201 (EMPA-Thun) with many colleagues. I really enjoyed the friendly atmosphere and spells of stimulating discussions on science and some other funny things. I thank them all.

Finally I would like to thank my wife, parents and sisters for their love, support and understanding, which provide me courage and power to tide over frustrations and finally succeed.

This page intentionally left blank

Contents

Abstract	i
Acknowledgments	v
1 Introduction.....	1
1.1 Scale effects on mechanical properties of materials.....	1
1.1.1 External length scale effects.....	2
1.1.2 Internal length scale effects	3
1.2 Overview of experimental techniques for nanomechanical characterization.....	4
1.3 Requirements for <i>in-situ</i> nanotensile measurements.....	8
1.4 State of the art of <i>in-situ</i> nanotensile testing	9
1.4.1 AFM tip-based nanotensile testing	10
1.4.2 MEMS-based nanotensile testing	11
1.5 Motivation, originality and main contributions of this thesis.....	16
1.6 Thesis outline	17
2 System design	19
2.1 Functions of the system	19
2.1.1 Research of solutions for designed functions	21
2.1.2 General concept of the system	28
2.2 Design of comb-drive actuator	29
2.3 Design of force sensor	32
2.3.1 Suspensions of force sensors.....	33
2.3.2 Triplate differential capacitive force sensor	35
2.4 Modeling of the whole system	41
2.4.1 Static analysis.....	41
2.4.2 Dynamic analysis.....	44
2.5 Summary	46

3	Microfabrication and packaging	47
3.1	Layout design issues	47
3.2	Microfabrication process	53
3.3	Packaging	57
3.4	Summary	59
4	Device characterization	61
4.1	Stiffness calibration	61
4.2	Voltage-displacement characteristic of actuator	63
4.3	Displacement-capacitance characteristic of capacitive sensor	65
4.4	Noise analysis for capacitive sensor	68
4.5	Pull-in voltage of capacitive sensor	71
4.6	Summary	72
5	<i>In-situ</i> nanotensile and electrical measurements	73
5.1	<i>In-situ</i> nanomanipulation	73
5.1.1	Challenges of <i>in-situ</i> nanomanipulation	74
5.1.2	Experimental setup	78
5.1.3	Manipulation procedure	79
5.2	Nanowelding	81
5.2.1	Focused electron beam induced deposition	81
5.2.2	Mechanical characterization of FEBID	82
5.2.3	NW contamination during nanowelding by FEBID	84
5.3	Nanotensile measurements	88
5.3.1	Si <111> nanowires	88
5.3.2	Si <100> nanowires	91
5.3.3	Co nanowires	93
5.4	<i>In-situ</i> electrical measurement.....	98
5.5	Summary	102
6	Conclusion and outlook	105
6.1	Conclusion	105

6.2 Outlook	107
6.2.1 Clamping mechanism.....	107
6.2.2 Alternative specimen alignment methods.....	108
6.2.3 Integration of a piezo-actuator into silicon based MEMS.....	108
6.2.4 Micro force sensor with tunable stiffness.....	109
A Effective mass of a double clamped beam.....	111
B Verification of doping in SiNWs by electron beam induced current imaging	113
B.1 Principle of EBIC imaging.....	113
B.2 Doping of SiNWs.....	114
B.2.1 SiNWs doped by CVD during VLS growth.....	115
B.2.2 SiNWs doped by PLD during VLS growth.....	116
B.3 Experimental results and discussion.....	118
B.3.1 Experimental setup.....	118
B.3.2 Results and discussions.....	119
B.4 Conclusions.....	122
Bibliography	123
Curriculum Vitae	135
List of Patents and Publications	137

This page intentionally left blank

1.

Introduction

Due to scale effects, nanostructures are expected to show different mechanical properties from their bulk counterparts. In this chapter, several experimental techniques that could be used to measure mechanical properties of nanostructures are briefly reviewed, which include tensile, bending, and resonance tests, as well as nanoindentation. The main advantages and limitations of each technique are outlined. Tensile testing is straightforward and reliable, as the stress state in the specimen tends to be uniform. The main requirements for tensile testing at the nanoscale are discussed, and the state of the art is reviewed with an emphasis on MEMS-based nanotensile tests. The motivation, originality, and major contributions of this thesis are presented, followed by a thesis outline.

1.1 Scale effects on mechanical properties of materials

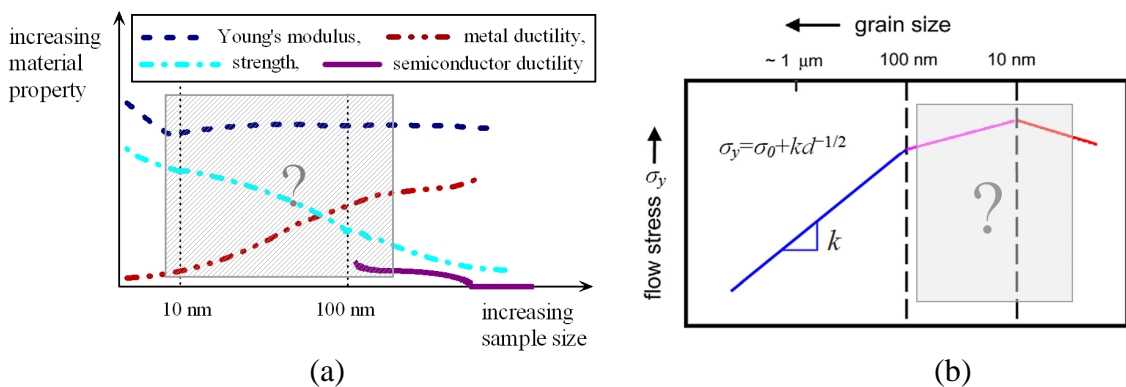


Figure 1.1: Schematics showing (a) external length scale effects: material mechanical properties versus material size in the nanometer range, and (b) internal length scale effects: relationship between yield strength and grain size [Kumar et al., 2003] of materials.

The effects of scale on material mechanics can be classified into two categories, namely, external length scale effects due to the sample size and internal length scale effects due to the grain size. The overall external length scale effects in the nanometer range can be approximately described by the curves shown in [figure 1.1\(a\)](#). For instance, material (metal and semiconductor) strength increases as its size scales down. [Figure 1.1\(b\)](#) shows the internal length scale effects, i.e. the relationship between yield strength and grain size. These scale effects and their probable origins are discussed in the following. It should be noted that the mechanisms that govern these scale effects are still not well understood, in particular when the material sizes are smaller than 200 nm and the grain sizes are smaller than 100 nm (i.e. the shadowed regions in [figure 1.1](#)).

1.1.1 External length scale effects

The material properties of thin films and small structures, with typical dimensions in the range of microns or below, can not simply be extrapolated from the properties of bulk samples. This is due to two major effects [[Kraft et al., 2001](#)]: First, samples used for bulk mechanical testing usually have dimensions which are much larger than the microstructural features (e.g. grains and particles), whereas in thin films the geometrical and microstructural dimensions are typically on the same order of magnitude. Second, mechanical behavior is controlled by certain fundamental length scales. For example, elastic properties are determined by the atomic bonds, with lengths in the range of 1 Angstrom. Plasticity in metals involves the motion of dislocations, which are hindered when they try to pass between obstacles spaced closer than about 100 nm. During fatigue in metals, complicated dislocation structures are formed, with typical dimensions of a few micrometers. And in brittle materials, fracture is initiated at defects with a critical size of several tens of micrometers. As a result, it is expected that the mechanical properties of a material will fundamentally change as the sample dimensions become smaller than these various intrinsic lengths. Note that MEMS and microelectronics fall in the range where fundamental changes in material properties (such as fracture, fatigue, and plasticity) are expected to occur [[Kraft et al., 2001](#)].

At room temperature, some brittle materials have been experimentally found to show *brittle-to-ductile transition* at certain length scales [[Gerberich et al., 2009](#)]. For example,

Si pillars with diameters ranging from 1 mm down to 200 nm show a transition from predominantly brittle to ductile behavior at room temperature [Östlund et al., 2009]. The relatively sharp transition was observed for samples having diameters in the range of 310 to 400 nm. Monocrystalline Gallium Arsenide pillars of 1 μm diameter were reported to deform plastically through uniaxial compression in [Michler et al., 2007].

As the sizes of 1D nanostructures decrease, their surface-to-volume ratios increase, and thus surface status could have significant influences on their mechanical properties. These *surface effects* could originate from surface oxide layers, surface contaminations, and the surface stiffness effects [Jing et al., 2006]. Atoms at or near a free surface have reduced coordination relative to interior lattice atoms. This reduced coordination gives rise to surface energy and the associated surface relaxations, which influence the mechanical behavior of nanostructures. Some atomistic studies show that surface stress and surface energy produce a change in both the elastic modulus and strength of nanowires as their sizes decrease to around 10 nm [McDowell et al., 2008]. However, a significant increase of the Young's modulus has been observed experimentally for larger characteristic sizes. For example, the elastic modulus of ZnO nanowires increase from 140 to 160 GPa as their diameters decrease from 80 to 20 nm [Agrawal et al., 2008], and the elastic modulus of Te nanowires that are thinner than 30 nm is about two times of that for bulk Te [Stan et al., 2008].

1.1.2 Internal length scale effects

In many microcrystalline (grain size >1 μm) and nanocrystalline materials with grain size >100 nm, a material's *yield strength* can be described by the well-known Hall-Petch relation ($\sigma_y = \sigma_0 + kd^{-1/2}$, σ_y : yield strength, d : grain size, k : coefficient) as shown in figure 1.1(b) [Courtney, 2000]. It is seen that the strength increases as grain size decreases, which is most likely owing to the retarded dislocation sliding by grain boundaries. In addition, the defects that can be accommodated in smaller grains are smaller, which also lead to higher strength. However, when the grain size is smaller than 100 nm, the scenario is markedly different. With further grain refinement ($d < 10$ nm), the yield stress decreases with grain size, which is called the inverse Hall-Petch effect. This has been verified by experiments and molecular dynamics based simulations [Meyers et

al., 2006; Diao et al., 2004; Agrawal et al., 2008]. The underlying mechanisms of the inverse Hall-Petch effect are still not well understood. One of the explanations is that the dislocation activity (nucleation and glide) no longer dominates the plastic deformation of ultrafine-grained materials. It is speculated that deformation in such cases are governed by either grain boundary sliding or grain rotation, thereby rendering the mechanical properties to be varied [Kumar et al., 2003]. The *ductility* is small (<5%) for most metals with grain sizes of <25 nm (the tensile ductility of their conventional counterparts at large grain sizes is >10%). This limited ductility in nanocrystalline materials could be attributed to three major sources [Meyers et al., 2006], namely: (1) artifacts from processing (e.g., pores); (2) tensile instability; (3) crack nucleation or shear instability.

The *elastic modulus* of many nanostructured metals was found to be somewhat lower than those of the coarse-grained bulk materials, and this could be attributed to the grain boundary compliance [Meyers et al., 2006].

1.2 Overview of experimental techniques for nanomechanical characterization

Many kinds of 1D nanostructures (e.g. nanotubes, nanowires and nanobelts) have been synthesized and demonstrated to exhibit superior mechanical, electrical, thermal, and optical properties over the past decade [Wang, 2006]. 1D nanostructures are promising for the applications in material reinforcement, biological and chemical sensing, and as building blocks in micro/nano electromechanical systems (MEMS/NEMS). Understanding mechanical properties of those nanostructures is essential for their practical applications. Recently, a variety of experimental techniques for nanomechanical characterization have been developed, including tensile, bending, resonance and nanoindentation testing.

Tensile testing is an established and widely used method for mechanical characterization of bulk materials owing to the fact that data interpretation is easier and fewer parameter assumptions are needed than in other mechanical testing methods. A stress-strain curve is obtained in a tensile test, from which Young's modulus, tensile strength, work hardening coefficient, and failure strain of the specimen can be determined. The schematic of a tensile testing is shown in figure 1.2(a). Assuming that

the measured nanowire has a diameter D , original gauge length L_0 , and elongated gauge length L , Young's modulus E can be calculated from

$$E = \frac{4F}{\pi D^2} \frac{L_0}{L - L_0} \quad , \quad (1.1)$$

where F is the applied tensile force.

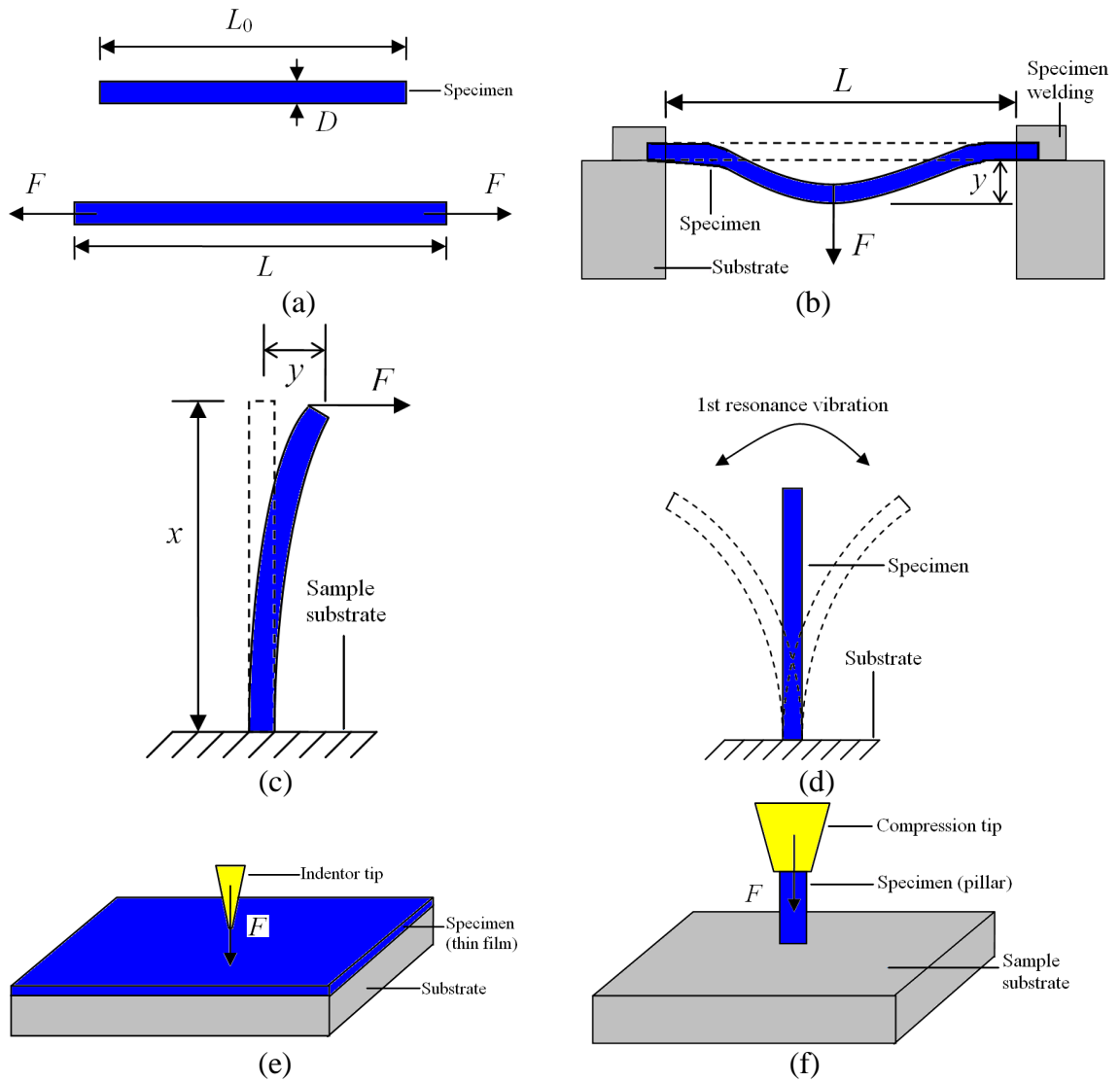


Figure 1.2: Schematics of (a) tensile testing, (b) three point bending, (c) free cantilever beam bending, (d) mechanical resonance testing, (e) nanoindentation, and (f) compression testing.

Bending tests have been carried out on a single clamped [Hoffmann et al., 2006; Gordon et al., 2009] or a double clamped (also called three point bending) [Varghese et

al., 2008] nanowire. These nanowires are either vertically grown on a substrate or dispersed randomly on a flat substrate with many pores (e.g. a TEM grid), such that many nanowires can bridge the pores. From the standpoint of sample preparation, a bending test is much easier to conduct than a tensile test at the nanoscale. In addition, the bending deformation is usually large enough to be measured with SEM images or an optical microscope. In practice, an AFM cantilever with a small spring constant (several N/m to several tens of N/m) is usually adopted to bend an individual nanowire, and the bending force is measured from the deflection of the cantilever. This AFM cantilever should have comparable stiffness to the bending stiffness of the nanowire tested. For a clamped-clamped nanowire with a length L subjected to a point load F at its mid-point, as schematically shown in figure 1.2(b), the elastic modulus E is given by

$$E = \frac{L^3}{y} \frac{F}{3\pi D^4} . \quad (1.2)$$

For a single clamped nanowire as schematically shown in figure 1.2(c), the elastic modulus E can be determined using the following expression

$$E = \frac{x^3}{y} \frac{64F}{3\pi D^4} , \quad (1.3)$$

where x and y are the distance of the point load F from the nanowire foot and the nanowire deflection at the loading point, respectively.

The main limitations of bending tests are [Johnson et al., 2000; Haque et al., 2006]: (1) a more stringent force resolution is required than in tensile tests since the nanowire bending stiffness is much smaller than its tensile stiffness; (2) the bending test is more sensitive to uncertainties in beam cross section (i.e. diameter D) than the tensile test in terms of elastic modulus measurement; (3) it is not straightforward as tensile test, especially during the large deformation and/or owing to the stress concentration at the boundary.

Mechanical resonance testing, as schematically shown in figure 1.2(d), can be carried out on nanowire cantilevers that are excited into resonance by electrical or mechanical methods. It's a non-destructive and dynamic method. Relying on SEM or TEM images, the fundamental frequency of a nanowire can be easily determined, which makes this testing method particularly suitable for *in-situ* testing. In addition, other

micro devices except for the resonance excitation instrument (macroscopic) are not required for such experiments. However, this technique can only measure the bending modulus of a specimen. Assuming that the vibrating nanowire is a cantilever beam with a small oscillation amplitude, the relationship between the first resonance frequency and the bending modulus in a low damping environment (which is ensured by the high vacuum in a SEM/TEM chamber) can be derived from Euler-Bernouli equation [Meirovich 1986] and given by

$$f = \frac{1.875^2}{8\pi} \frac{D}{L^2} \sqrt{\frac{E}{\rho}}, \quad (1.4)$$

where f is the first resonance frequency and ρ is the nanowire density.

Figure 1.2(e) shows a schematic of *nanoindentation testing*, where an indenter tip is pushed into the surface of a thin film and the penetration depth as a function of the applied load during loading and unloading are recorded. From the indentation load-displacement curve, the hardness and elastic modulus of the specimen can be determined. The specimen hardness H can be calculated with the peak load F_{\max} from

$$H = \frac{F_{\max}}{A}, \quad (1.5)$$

where A is the projected contact area. The elastic modulus E can be calculated using the Oliver-Pharr analysis procedure as presented in [Li et al., 2003]. The relationship among the unloading stiffness K_u , A , and E is given by

$$K_u = 2\beta \sqrt{\frac{A}{\pi}} E_r, \quad (1.6)$$

where β is a constant depending on the geometry of the indenter tip. $K_u = \frac{dF}{dh}$ can be obtained from the slope of the initial portion of the unloading curve, here h is the indentation depth. E_r is the reduced elastic modulus that accounts for the fact that elastic deformation occurs in both the sample and the indenter, which is given by

$$\frac{1}{E_r} = \frac{1-\nu^2}{E} + \frac{1-\nu_i^2}{E_i}, \quad (1.7)$$

where E_i and ν_i are the elastic modulus and Poisson's ratio of the indenter, and ν is the Poisson's ratio of the specimen. For diamond, $E_i = 1141$ GPa and $\nu_i = 0.07$. It is clear that the indentation results highly depend upon the local structures of the tested specimen.

The main drawback of nanoindentation is the large stress and strain gradient that form beneath the tip in addition to the hydrostatic component of the stress tensor, which make data interpretation problematic.

Compression testing, as schematically shown in [figure 1.2\(f\)](#), can be performed using a similar instrument as for nanoindentation. The main difference between compression testing and nanoindentation is that the whole specimen is uniaxially stressed in compression testing while only a small portion of the specimen is loaded in indentation. However, 1D nanostructures having large aspect ratio (length to diameter) are not suitable for compression test since they can easily buckle. In addition, a regular geometry (e.g. a cylinder) of the specimen is normally required for easy interpretation of the results in compression testing. Therefore, compression testing is suitable for testing pillars down to sub-micrometer size, but not applicable for most 1D nanostructures.

1.3 Requirements for *in-situ* nanotensile measurements

Ideally, a nanotensile stage for *in-situ* SEM/TEM study should meet the following requirements:

1) *compatibility with SEM/TEM*: First, the device should be accommodated on the SEM/TEM stage. Second, the instrument and the electrical conducting wires should be vacuum compatible [[Rouki et al., 2003](#)]. Third, the operation of the device should not disturb the primary electron beam (e-beam) of the SEM/TEM. For most SEMs, a setup with a volume of $<10^3 \text{ cm}^3$ can be installed on the stage. However, for TEM applications the device volume is strictly limited to $<100 \text{ mm}^3$. In addition, an opening beneath the specimen in the testing device is needed to allow the transmission of electron beams in a TEM.

2) *measurement of specimen elongation with nanometer resolution, where resolution is defined as the minimum signal that can be measured, which is given by noise level/sensitivity*: The elongation percentage of a nanowire at failure is generally less than 10%, which corresponds to a total elongation of $<800 \text{ nm}$ at failure for a specimen with an initial gauge length of $8 \text{ }\mu\text{m}$ (see [Chapter 5](#)). Therefore, a displacement resolution of better than 50 nm is usually required in nanotensile testing.

3) *actuator that can exert a uniaxial tensile load with a small step increment (nano-Newton level)*: A tensile stage can work in two different modes depending on the types of actuators employed, namely, displacement-controlled mode and load-controlled mode. Piezoelectric and microfabricated thermal actuators are working in the displacement-controlled mode, because they have very large stiffness compared to that of the specimen and the force sensor. These actuators should have a sufficiently large range of movement (typically a few micrometers) to allow for stretching a specimen to failure, and should have a fine moving resolution (i.e. the smallest moving step) of several nanometers to several tens of nanometers to allow for stepwise increment of strain in a specimen. A tensile stage with an electrostatic actuator works in a load-controlled mode owing to their low stiffness. Then the actuator is desired to output tensile forces that could fracture the specimen (typically in the range from 1 μN to a few hundreds of micro-Newtons), and to have a controlled stepwise increment of the output force with a resolution of tens of nano-Newtons. Detailed analysis for the actuator design in a nanotensile stage is presented in [Chapter 2](#).

4) *force sensor with a resolution of several tens of nano-Newtons*: Force sensors that meet this requirement and suit SEM/TEM environment include capacitive sensors, microfabricated compliant beams (with a small spring constant), and piezoresistive cantilevers. In addition, a force sensor connected to a specimen in series can measure the tensile load directly. Detailed analysis of the sensor design in a nanotensile stage is presented in [Chapter 3](#).

1.4 State of the art of *in-situ* nanotensile testing

In spite of the significant challenges encountered in nanotensile testing, remarkable progress has been made in the last decade. According to the configurations of the testing apparatus, these studies fall into two categories, namely AFM tip-based and MEMS-based tests.

1.4.1 AFM tip-based nanotensile testing

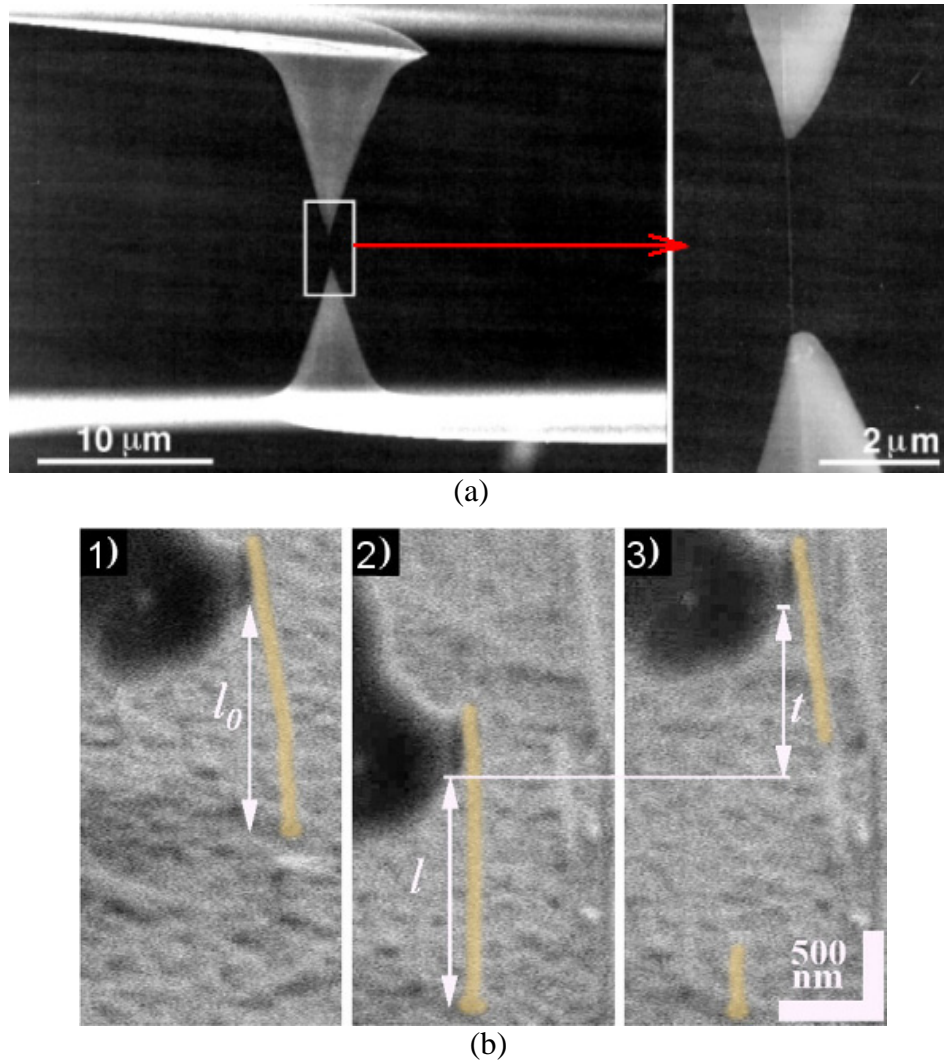


Figure 1.3: (a) A MWCNT clamped between two opposing AFM tips [Yu *et al.*, 2000]. (b) Sequence of a tensile experiment on ZnO nanowire [Hoffmann *et al.*, 2007].

Yu *et al.* performed the first *in-situ* SEM tensile testing of multiwalled carbon nanotubes (MWCNTs) with a home-built nanomanipulator [Yu *et al.*, 2000]. The two ends of a single CNT were clamped to two opposing AFM tips by localized FEBID of carbonaceous material. One of the AFM tips was very soft (spring constant less than 0.1 N/m) and was used as a load sensor. The other rigid AFM tip (either a Digital Instruments TESP probe tip or a NT-MDT cs12 noncontact mode probe) acted as an actuator, which was driven by a linear motor. The clamped CNT was loaded in tension

when the rigid cantilever moves away from the soft cantilever, as shown in [figure 1.3\(a\)](#). The CNT elongation was measured by SEM images analysis. The Young's modulus and failure strength of the MWCNTs were measured to be 270-950 GPa and 11-63 GPa, respectively. Ding *et al.* also performed *in-situ* SEM tensile tests on crystalline boron nanowires using a similar setup of double AFM tips, where an average Young's modulus of ~320 GPa and a ultimate strength of 2-8 GPa were reported [[Ding et al., 2006](#)].

Hoffmann *et al.* conducted tensile tests on individual ZnO nanowires inside a SEM with a home-built nanomanipulator [[Hoffmann et al., 2007](#)]. An AFM tip (spring constant of 45 N/m) was mounted on a piezoelectric manipulator, and a sample substrate, with vertically grown ZnO nanowires, was glued on a second piezoelectric manipulator that is of sub-nanometer resolution. The AFM tip was brought into contact with the top of a nanowire interested, and a nanoscale welding was made at this contact by FEBID of carbonaceous contamination inside a SEM. By moving the sample substrate away from the AFM tip, the ZnO nanowires were stretched as shown in [figure 1.3\(b\)](#). The deflection of the AFM tip was used to measure the tensile force on the specimen and the specimen elongation was obtained by image analysis. The measured Young's modulus of single crystal ZnO nanowires (growth along [0001]) was found to be about 100 GPa.

The major advantage of an AFM tip-based tensile test is that tedious manipulations of nanowires could be avoided. However, a uniaxial tensile force is difficult to maintain owing to the 2-D projection of the SEM image system [[Li et al., 2005](#)]. Hence, the loaded nanowires are susceptible to bending owing to the deflection of the cantilever end.

1.4.2 MEMS-based nanotensile testing

Microfabricated devices are very attractive for *in-situ* applications due to their small volumes and high resolutions. In addition, by integrating micro actuators and micro sensors on the same chip, a uniaxial tensile load on the specimen can be safely obtained. Several kinds of MEMS-based nanotensile stages have been developed in the last decade, which are briefly reviewed in the following.

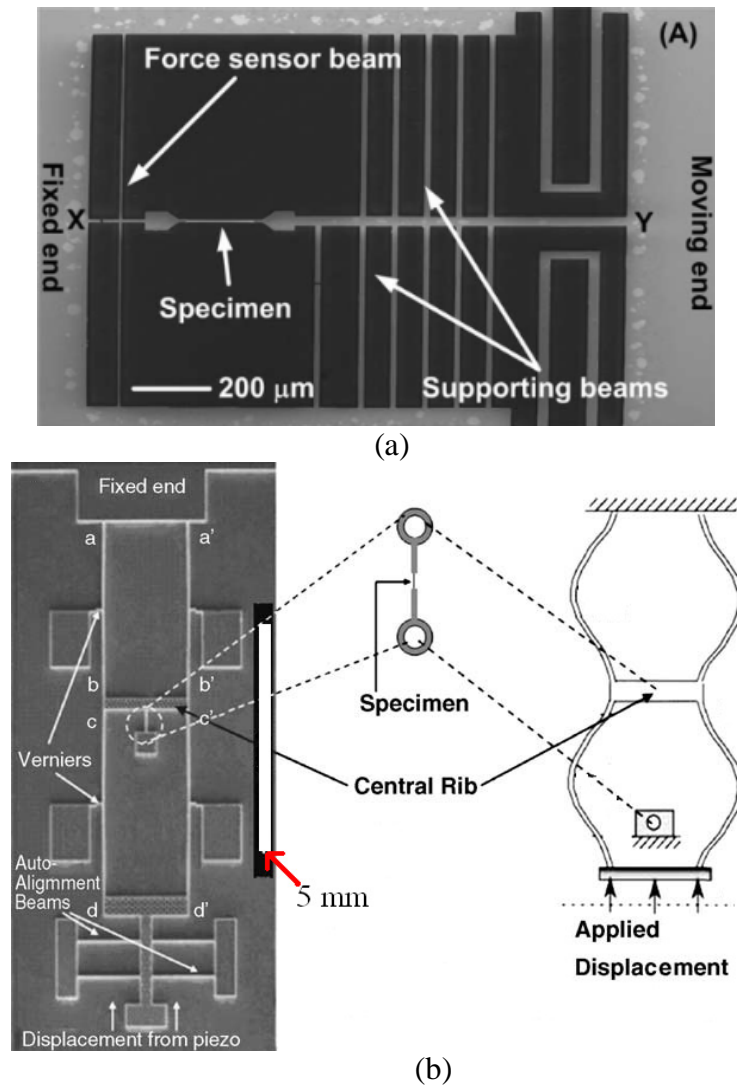


Figure 1.4: (a) SEM image of a fixed-fixed beam force sensor with co-fabricated specimen (Aluminum) [Haque et al., 2005]. (b) SEM image of slender Si columns and schematic of the buckled device [Samuel et al., 2006].

Haque *et al.* designed two types of *in-situ* SEM/TEM nano-tensile stages, where flexible beams were employed as force sensors, as shown in figure 1.4(a) [Haque et al., 2005] and (b) [Samuel et al., 2006], respectively. In their first stage, double clamped beams were used as a force sensor. Several supporting beams located between the actuator and the specimen were designed to absorb any off-axis component of the externally applied displacement through a piezo actuator. In their second design, they adopted non-linear post-buckling mechanics to achieve an ultra-low stiffness to enhance the force sensing resolution (pico-Newton resolution was achieved). For both of their

designs, a commercial miniature piezo-actuator was assembled with the MEMS device. The on-chip integration of a piezoelectric actuator with a force sensor is a possible solution towards furthering the compactness of their systems, but the fabrication of piezoelectric functional layer onto a silicon substrate is still a technical challenge [Wang et al., 2008]. In addition, the first design (figure 1.4a) has a high probability of sample failure during fabrication and the force sensor could only be calibrated by cleaving the stage after sample testing.

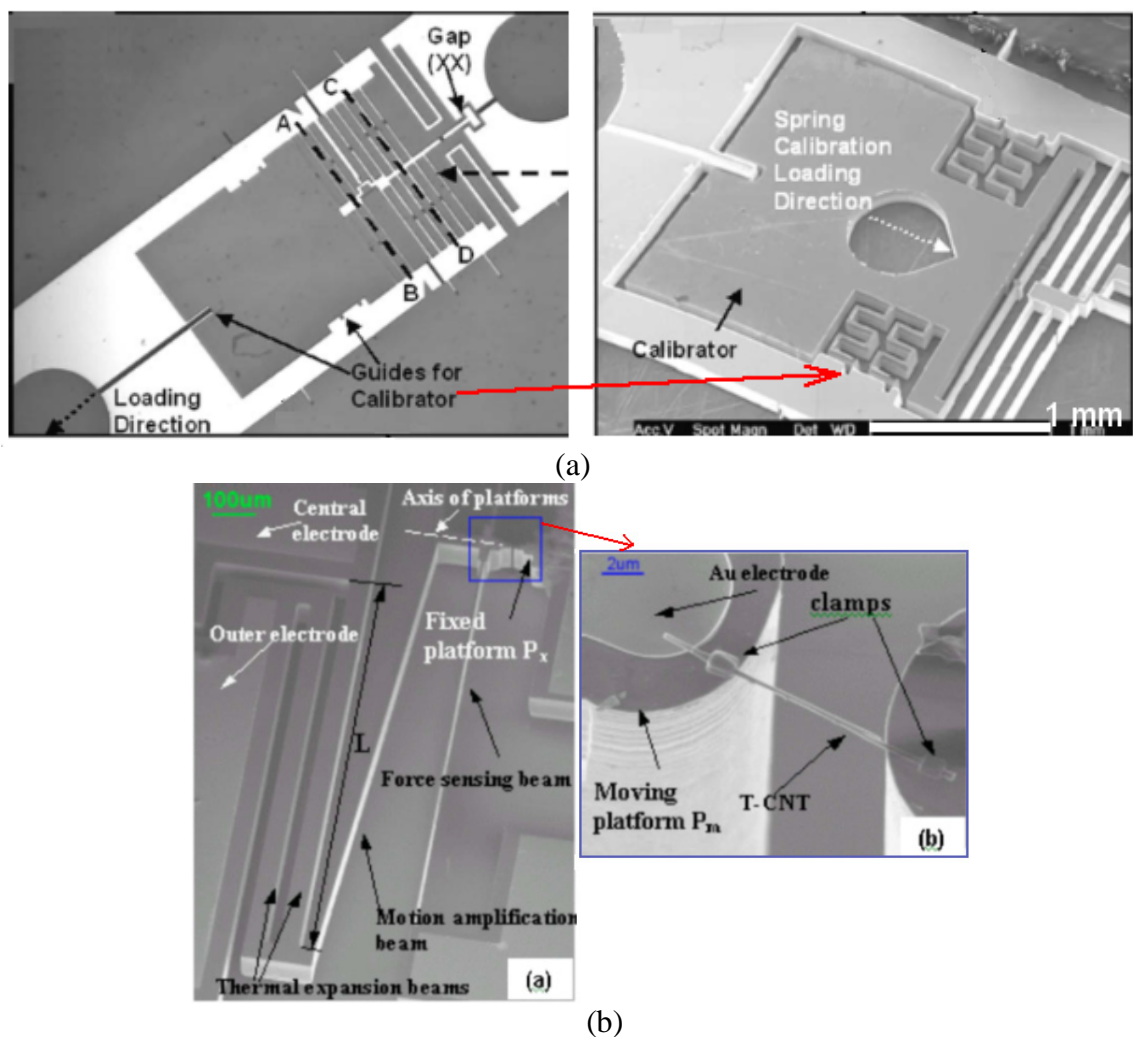
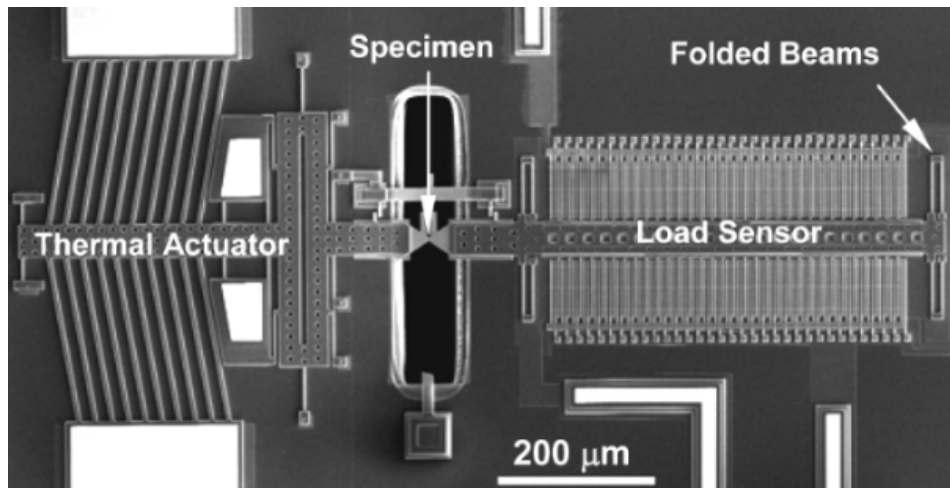


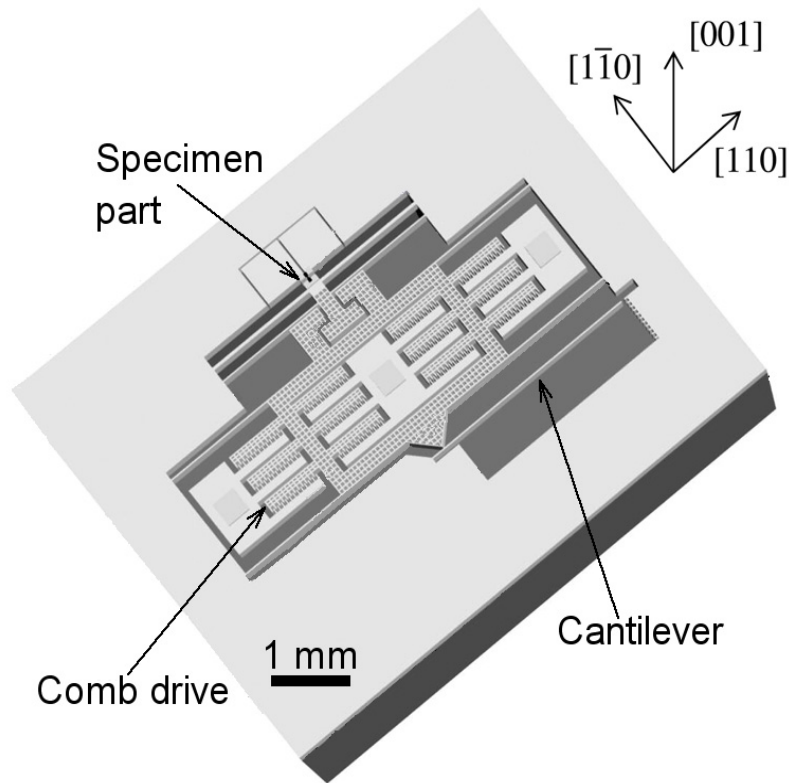
Figure 1.5: (a) SEM images of a fixed-fixed beam force sensor with co-fabricated calibrator [Han et al., 2006]. (b) SEM images of a thermal actuator and an aligned CNT on the device [Lu et al., 2006].

To overcome these limitations, Han *et al.* redesigned the stage as shown in [figure 1.5\(a\)](#), which enabled the sensor stiffness calibration prior to testing without cleaving and resistivity measurement of the nanoscale freestanding metal film at different temperatures, in addition to the stress-strain measurements under uniaxial tension [[Han et al., 2006](#)]. The basic idea was to fabricate another force sensor (flexible beams) that could be broken off from the tensile stage and calibrated independently by nanoindentation. The tensile stage was placed on a hot plate during the resistivity measurement under various temperatures.

Lu *et al.* designed a nanotensile stage consisting of a thermal actuator and a flexible beam force sensor as shown in [figure 1.5\(b\)](#) [[Lu et al., 2006](#)]. Integrated motion amplification structures (V-shaped compliant beams) were designed in the thermal actuation to increase its moving range. The specimen could be aligned on the device by an electric-field guided assembly in a liquid (dielectrophoretic alignment), which was then welded on the MEMS device by FEBID of carbonaceous material. Espinosa *et al.* adopted a thermal actuator in their MEMS-based tensile testing system, as shown in [figure 1.6\(a\)](#), but a surface micromachined capacitive sensor was integrated to measure the load electronically, which offers the possibility of continuous observation of the specimen at a high magnification during testing [[Espinosa et al. 2007](#)]. The best resolution of their fabricated capacitive sensor is 0.05 fF, and the corresponding displacement resolution is 1 nm. For a load sensor with stiffness of 11.8 N/m designed for testing carbon nanotubes and thin nanowires, the corresponding load resolution is 12 nN. Thermal actuators have a large stiffness and can provide much higher actuation force than electrostatic actuators. However, special care has to be taken to the possible heat conduction to the specimen and the out-of-plane displacements of the thermal actuator. These deleterious effects could be eliminated by integrating micro heat sinks and optimizing device geometries as discussed in [[Zhu et al., 2006](#)]. For the testing stages with surface micro-machined comb-drive actuators and/or capacitive sensors, the levitation effect [[Tang et al., 1992](#)] arising from the electrostatic force between the suspended structures and the substrate is deleterious, and this could introduce an out-of-plane force in the specimen. Another potential problem of the surface micromachining is that residual stress could be created in thin films bending flexible structures.



(a)



(b)

Figure 1.6: (a) SEM image of a thermal actuator with a surface micromachined capacitive sensor [Espinosa *et al.* 2007]. (b) Schematic of a comb-drive actuator and a motion amplification cantilever [Kiuchi *et al.*, 2007].

Using a bulk micro-machined comb-drive actuator, Kiuchi *et al.* reported a tensile testing system with a cantilever as the lever motion amplification system [Kiuchi *et al.*, 2007], as shown in figure 1.6(b). The tested specimen (carbon nanowire) was directly

deposited on the MEMS device by FIBID using phenanthrene as the precursor gas. The tensile force on the specimen is calculated from the displacement differences of the cantilever end with and without a specimen residing on the device.

1.5 Motivation, originality and main contributions of this thesis

Various experiments and atomistic modeling have shown that the mechanical behavior of nanostructured materials could be remarkably different from their bulk counterparts [Diao et al., 2004; Wu et al., 2006; He et al., 2008; McDowell et al., 2008]. However, exploring material behavior at the nanoscale is hindered by the difficulties of conducting well-instrumented mechanical testing. Nanotensile testing is more straightforward and precise than the other testing methods, but it encounters significant challenges. The motivation of this thesis is to develop a nanotensile testing instrument for characterizing 1D nanostructures, aiming at revealing novel material behavior at the nanoscale, validating atomistic computational predictions, and understanding the underlying material deformation mechanisms.

The main originality of this thesis is the realization of a novel MEMS-based nanotensile stage that can be used for *in-situ* electron microscopy mechanical testing of individual 1D nanostructures. The developed testing stage is composed of a comb-drive actuator and either a differential capacitive force sensor [Zhang et al., 2009a] or a clamped-clamped beam force sensor [Zhang et al., 2009b], which is fabricated in a SOI wafer by an optimized DRIE based process. The device architecture is optimized based on analytical modeling and numerical simulation with FEA to achieve the desired performance [Zhang et al., 2009c]. The fabricated electrostatic actuator can output a voltage-controlled force up to 210 μN at a drive voltage of 120V, and the force sensors have a resolution of better than 50 nN. The realization of electrostatically actuated nanotensile stages in this thesis is an important development in the field of experimental nanomechanics.

A novel strategy of modifying device topography, e.g. in the form of trenches and pillars, was proposed to facilitate *in-situ* SEM pick-and-place nanomanipulation, which could achieve a high yield of about 80%. This strategy, significantly reduces the

difficulties of specimen preparation for nanotensile testing, and will therefore be helpful for *in-situ* nanomanipulations in the nanoengineering community.

One of the major contributions in the device design is the establishment of a complete analytical model to study the influence of the electrostatic force (it is called “parasitic force” in this thesis) induced by the excitation signal of the triplate differential capacitive sensor on the sensor’s performance, i.e. sensor’s stability, linearity and sensitivity (see [Section 2.3.2](#)). This analytical modeling is useful for design optimization and performance examination of triplate differential capacitive sensors.

The tensile properties of electrochemically deposited Co nanowires were determined for the first time. The average Young’s modulus, tensile strength and fracture strain of these Co nanowires were measured to be (75.3 ± 14.6) GPa, (1.6 ± 0.4) GPa and (2.2 ± 0.6) %, respectively. These values represent higher tensile strength and lower fracture strain than their bulk polycrystalline counterparts (~ 0.8 GPa, 6%-19%) [[Karimpoor et al., 2006](#)]. This can be partly attributed the small grain size of the nanowires. The measured apparent Young’s modulus and tensile strength are significantly lower than the bulk modulus and the theoretical strength of monocrystalline samples, respectively. This is likely caused by the structural defects (e.g. pores) and surface effects (e.g. surface oxide layer and surface contaminants).

The tensile properties of two different types of SiNWs, i.e. from top down chemical etching and bottom up VLS growth, were also measured by the developed tensile stages. The phosphorous-doped SiNWs grown bottom up by the VLS mechanism show an average Young’s modulus of (170.0 ± 2.4) GPa and a tensile strength larger than 8.3 GPa. This finding confirms that the material’s strength increases as their sizes scale down [[Courtney, 2000](#)]. The top down electroless chemically etched SiNWs with their long axis along the $\langle 100 \rangle$ direction of the starting silicon wafer show a tensile strength of 5.4 GPa.

1.6 Thesis outline

This thesis can be divided into three major topics dealing with design and fabrication of the MEMS devices, characterization, and the application of the devices in testing individual nanowires, which are contained within the following six chapters.

The current chapter presents an overview of scale effects on the mechanical properties of materials, experimental techniques for nanomechanics study, the requirements in a nanotensile testing, and its state of the art.

[Chapter 2](#) introduces the design methodology of the proposed nanotensile stages, which are based on analytical modeling and numerical simulations by FEA.

[Chapter 3](#) introduces the fabrication and packaging methods of the MEMS devices. Several important issues related to the fabrication process are discussed in detail.

[Chapter 4](#) presents the experimental techniques used to calibrate the device performance and the characterization results, which consists of stiffness calibration, voltage-displacement characteristics of the actuator, displacement-capacitance characteristic of the capacitive sensor, noise analysis and pull-in voltage estimation for the capacitive sensor.

[Chapter 5](#) demonstrates the device capabilities of mechanical testing by *in-situ* SEM tensile tests on individual SiNWs and Co nanowires. The challenges and proposed strategy for *in-situ* nanomanipulation are discussed. The main difficulties of conducting *in-situ* electrical tests with the developed MEMS devices are also discussed.

[Chapter 6](#) revisits the major results, conclusions and perspectives for the future work.

2.

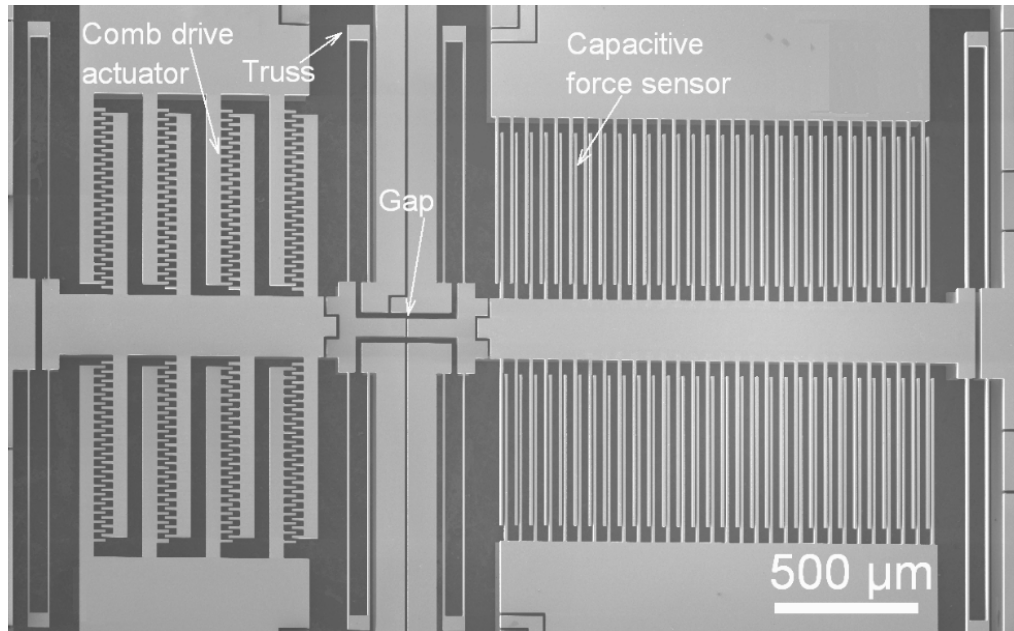
System design

Two types of MEMS-based nanotensile stages are designed, as shown in [figure 2.1\(a\)](#) and [\(b\)](#). One consists of a comb-drive actuator and a capacitive sensor with folded flexures. The other one is composed of a comb-drive actuator and a clamped-clamped beam force sensor. First, the selection criteria and design strategies of the employed actuators and force sensors are presented according to the designed functions of the testing system, namely, tensile testing and on-chip electrical testing. Analytical expressions for studying the influence of the parasitic force on capacitive sensor's stability, linearity and sensitivity are derived and discussed. Tensile force deposited in a specimen and the corresponding sensor displacements at different drive voltages are derived from the lumped force-displacement model of the system. The system dynamics is studied from a spring-mass model to determine the necessary relaxation time between each increment of the drive voltage.

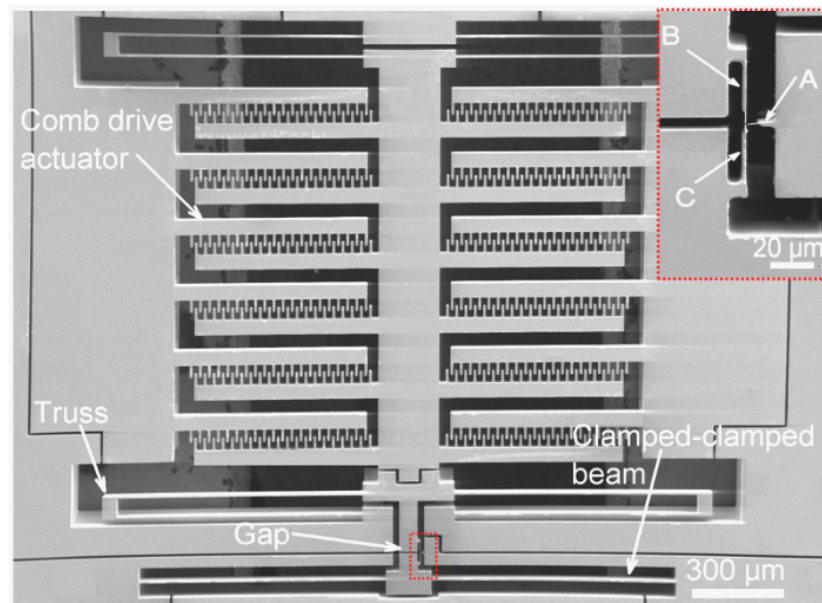
2.1 Functions of the system

Two basic functions are designed in the nanotensile testing system, namely, mechanical tensile testing and on-chip electrical testing. The goal of the mechanical tensile testing is to apply a uniaxial tensile load and to measure the engineering stress and engineering strain of a specimen, from which mechanical properties of the specimen, such as Young's modulus, tensile strength, failure strain, and/or yield strength, can be determined. The electrical testing is intended to measure the specimen resistivity or direct piezoelectric effect (i.e. the electrical charge induced by strain) in a single nanowire (this function was not successfully executed during to some experimental challenges, see [Section 5.4](#)). The mechanical and electrical measurements can be conducted independently or concurrently. The novel electromechanical properties of various 1D nanostructures, e.g. the giant piezoresistance effect in SiNWs [[He et al., 2006](#)]

and the direct piezoelectric effect in BaTiO₃ nanowires [Wang et al., 2007], are possibly measured with the developed device.



(a)



(b)

Figure 2.1: SEM images of (a) a tensile stage consisting of a comb drive and a capacitive sensor and (b) another stage consisting of a comb drive and a clamped-clamped beam force sensor. Inset of (b) shows the designed “three-beam structure” for concurrent measurement of specimen elongation and tensile force (see Section 3.1C).

2.1.1 Research of solutions for designed functions

For *in-situ* SEM/TEM tests, specimen elongation can be measured from SEM/TEM images with up to sub-nanometer resolution. The major concern in the system design is the actuator, force sensor, and on-chip electrical circuit.

A. Selection of an actuator

As specified in [Section 1.3](#), the main requirement of the actuator in a nanotensile stage is that it can exert a uniaxial in-plane tensile load with a small step increment (nano-Newton level).

The commonly employed actuation schemes in MEMS are electrostatic [[Tang et al., 1989](#)], electrothermal [[Sehr et al., 2001](#)], and piezoelectric [[Wang et al., 1999](#)] actuations. Electrostatic actuators are seldom used in the macro scale, but widely employed in MEMS due to the nature of scaling laws of electrostatic force and the ease of micro-fabrication. Electrostatic actuators have small force output lying at 10^{-6} - 10^{-3} N, but can offer relatively large displacements of up to 200 μm [[Bell et al., 2005](#)]. Electrothermal actuators utilize bent beam amplification to generate relatively large displacement from the thermal expansion of resistively-heated actuator elements, which are particularly promising for delivering large displacements (1-100 μm) and/or high forces (10-100 μN) [[Prasanna et al., 2007](#)]. The out-of-plane actuation can be easily obtained by thermal bi-material actuators, which is otherwise difficult to achieve. Piezoelectric micro-actuators in general, are capable of delivering relatively large forces (10 μN - 1 mN) but are limited to small displacements (0.1-10 μm). Ferroelectric piezoceramics such as BaTiO₃, PZT, PZN-PT, PMN-PT, and PYN-PT are generally used in thin-film piezoelectrics [[Prasanna et al., 2008](#)] due to their high d coefficients (i.e. the piezoelectric constants, which relate the mechanical strain produced by an applied electric field) and reasonably high Curie temperatures. However, the micro-fabrication of these materials is technically challenging today.

Compared to electrostatic actuators, thermal actuators have larger stiffness and can provide higher output force, which allows for testing stiffer nanostructures. However, the specimen is mechanically connected to the actuator, which reaches a temperature of up to 300-600 °C during actuation [[Zhu et al., 2006](#); [Hazra et al., 2009](#)] in the tensile

stage. Hence, thermal conduction from the actuator to the specimen can be high, which might influence specimen properties to some extent. This effect can be more pronounced for *in-situ* tests in the vacuum chamber of a SEM/TEM, since the thermal convection is minimized and thermal conduction dominates the heat dissipation. To limit the heating of the specimen, micro heat sinks must be designed between the thermal actuator and specimen as reported in [Zhu et al., 2006].

Electrostatic actuators were adopted in this thesis due to the attributes of easy fabrication, process compatibility with other MEMS structures, and no heat generation. Among various designs of electrostatic actuators [Tang et al., 1989; Ye et al., 1998; Seeger et al., 2003], comb drives and parallel plate actuators, as schematically shown in figure 2.2(a) and (b), are the two most common configurations used in MEMS.

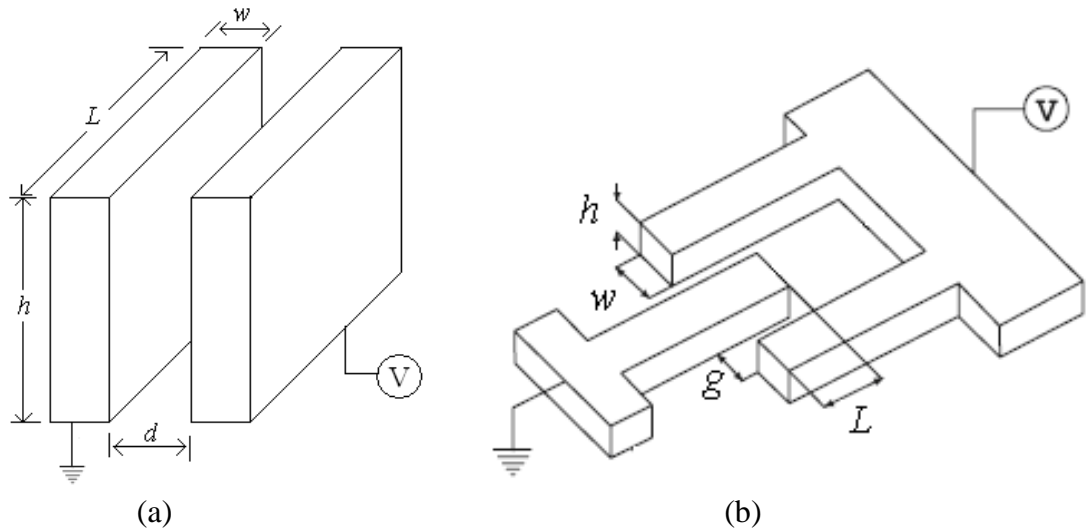


Figure 2. 2: Schematics of (a) a parallel-plate electrostatic actuator and (b) a comb drive.

If the fringing electric field is negligible (which is valid when the thickness h of the parallel plates is much larger than their widths w), the electrostatic force between parallel plates can be given by

$$F_{para} = \frac{\partial \left[\frac{\epsilon_0 A}{2(d-x)} V^2 \right]}{\partial x} = \frac{\epsilon_0 h L}{2(d-x)^2} V^2, \quad (2.1)$$

where V is the DC drive voltage applied to the actuator, d is the original gap between the plates, and A is the overlapping area. The commonly used formula describing the electrostatic force of a comb-drive actuator is

$$F_{comb} = 2 \frac{\partial [\frac{\epsilon_0 h (L \pm x)}{2g} V^2]}{\partial x} = \frac{\epsilon_0 h}{g} V^2, \quad (2.2)$$

where h and L are the thickness and the original overlapping length of the comb fingers, and g is the gap between comb fingers. Note that [equation 2.2](#) is deduced under the following assumptions [[Johnson et al., 1995](#); [Yeh et al., 2000](#)]: (1) the electrostatic fringing field is neglected; (2) the length of comb fingers is much larger than the gaps; (3) the length of comb fingers is much larger than the width; (4) the overlapping length is much larger than the gap.

From [equation 2.2](#), it can be seen that a comb-drive actuator exerts displacement-independent linear force with respect to the voltage squared. In contrast, the output force of a parallel plate actuator depends on the drive voltage and also the displacement. Hence, the tensile force is easier to be controlled in a comb-drive actuated tensile stage. Furthermore, comb drives generally have larger moving range than parallel actuators. It's well known that the parallel plate actuator has a maximum stable working range of $d/3$ [[Seeger et al., 2003](#)]. Beyond that range ($x \geq d/3$), electrostatic force can not be overcome by the restoring force of the actuator flexures, and thus “pull-in” occurs. It should be noted that the comb drives can also have two other instabilities, which are called “side pull-in” and “front pull-in”. The side pull-in happens when the movable fingers move laterally and snap into the fixed fingers. The front pull-in happens when the far-ends of the movable fingers stick to the roots of the fixed set of the comb fingers. Detailed analysis of these two pull-in instabilities of comb drives can be found in [[Jaecklin et al., 1992](#)].

B. Selection of a force sensor

As specified in [Section 1.3](#), a force measurement resolution of tens to few hundreds of nano-Newtons is required in nanotensile testing.

To measure such small force, micro-fabricated flexible beams with small spring constants are often adopted, where the force can be calculated from the beam deflection.

Depending on the techniques of detecting beam deflection, force measurement can be classified into three categories, namely, optical (e.g. in AFM), capacitive (e.g. in a capacitive inertial sensor), and piezoresistive (e.g. in a piezoresistive cantilever) types. In this thesis, tensile stages are designed for *in-situ* electron microscopy testing, the optical technique is difficult to be implemented since additional large-volume instruments are typically needed in this case. The flexible beams can be observed directly in SEM/TEM images, which have been frequently adopted in various nanomechanical tests [Yu et al., 2000; Haque et al., 2005; Hoffmann et al., 2006; Kiuchi et al., 2007]. Piezoresistive cantilevers can electronically measure force with nano-Newton resolution [Duc et al., 2006], but they are prone to suffer from large thermal drift. This effect can be more serious for *in-situ* tests since the electron-specimen interaction could generate considerable heat. A temperature compensation structure has to be included in the application of piezoresistive sensing. Furthermore, the traditional surface piezoresistive detecting method can only be used to measure out-of-plane force (i.e. force normal to the surface of a silicon wafer). To measure in-plane force, as required in tensile testing, the piezoresistors have to be fabricated at the sidewall of the cantilevers [Sun et al., 2008], which is a significant fabrication challenge.

A MEMS capacitive sensor is highly attractive for nanomechanical testing applications due to the high sensitivity, low temperature drift, process compatibility with other functional structures, and low power dissipation. Compared with the image-based complaint beams, the employment of the capacitive sensor also provides an advantage of continuous observation of the specimen at high magnification during testing. Among various designs of MEMS capacitive sensors, bulk micro-machined differential capacitive sensors [Despont et al., 1993; Brosnihan et al., 1997; Driehuisen et al., 1997; Ishihara et al., 1999; Sun et al., 2005; Suster et al., 2006] made from single crystal silicon (SCS) do not suffer from residual stress in thin solid films that are difficult to be controlled in surface micromachining. The high aspect ratio structures by DRIE allow for higher sensitivity and lower off-axis sensitivity due to the larger overlapping area of sensing electrodes and higher stiffness ratio between axial and lateral directions than achievable with surface micromachining. Also, the linearity is increased significantly by a differential sensing scheme. However, the high-density electrical interconnections and

isolations that are normally required in capacitive sensors remain as a technical challenge. Recently, Sun *et al.* proposed a novel triplate capacitance sensing configuration [Sun *et al.*, 2005] that is free of complex interconnections. This configuration gives promising perspectives for designing testing systems with self-actuating and self-sensing functions to characterize nanostructures.

C. Design of on-chip electrical circuit

The on-chip electrical circuit has two functions: (1) providing electrical traces for comb drive and capacitive sensor; (2) enabling on-chip electrical measurements of a nanostructure residing on the device.

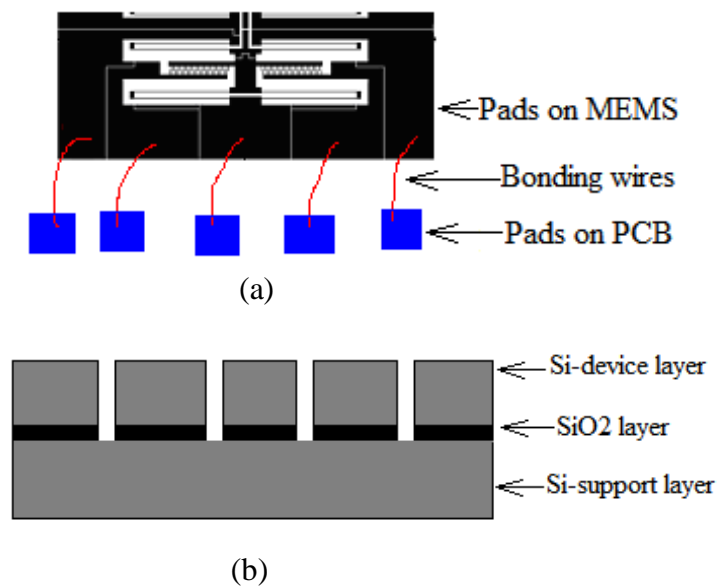


Figure 2.3: Schematics of the electrical connections for a comb-drive actuator: (a) top view and (b) side view.

IC and surface micro-machined MEMS devices generally have 2D architectures. Complex electrical interconnections and insulations can be realized by stacking of multiple dielectric (e.g. SiO_2 , Si_3N_4) and conductive layers (e.g. Al, doped polysilicon) connected by vertical conduction parts. However, the bulk micro-machined MEMS devices have a large size in the third dimension (i.e. high depth), which makes the on-chip electrical connections and insulations quite challenging. For electrostatic MEMS devices, vertical trench isolation is commonly adopted in a SOI or a Si-on-glass (SOG)

wafer to electrically insulate different functional parts, as schematically shown in [figure 2.3\(a\)](#) and [\(b\)](#). In this case, all the electrical traces can not cross, which remains a main limitation of designing high-density on-chip electrical interconnections in MEMS.

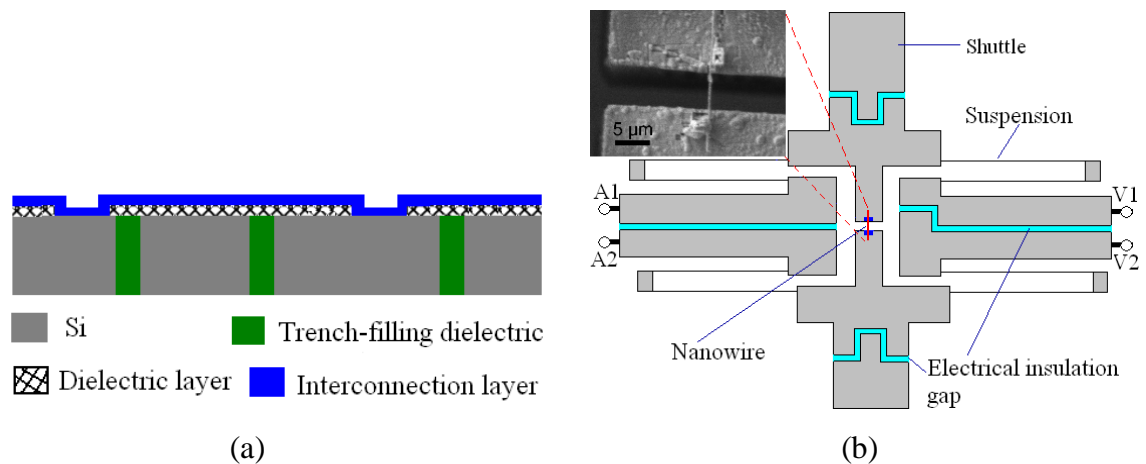


Figure 2.4: (a) Schematic of isolating trenches serving as a mechanical support for the electrical interconnects. (b) Electrical connections for the electrical measurement on sample in the designed tensile testing device. Inset: SEM image of a Co nanowire bridging a gap.

Filling trenches with dielectrics (e.g. SiO_2 , Si_3N_4 and polysilicon) is a promising technique to address the above issue, by enabling stacking of multiple dielectric and conductive layers on device surface and realizing MEMS devices with multiple level electrical interconnects from a single conductive wafer (not using an expensive SOI wafer). [Figure 2.4\(a\)](#) is a schematic of using isolating trenches as mechanical supports for the electrical interconnections in a standard Si wafer. This technique has attracted a great deal of interest in recent years. Incomplete refill leaves a void or a keyhole in these trenches, which could cause a degradation of the mechanical strength of the refilled trenches. The refilling process is closely related to the size and shape of the vertical trenches, and the process conditions of the dielectrics. In practice, a small trench width is preferable to avoid an excessive deposition time during the refill step. However, trenches of small opening are difficult to achieve high depth from DRIE. To completely refill a trench, a layer with thickness of at least half of the trench width must be deposited. At the interconnection of two trenches, a width is larger and the deposited layer must be even thicker [[Sarajlic, 2006](#)]. In such cases, not only the deposition time increases, but

the time to remove a layer from the top surface increases as well. Furthermore, a very thick deposited layer with a high intrinsic stress can make further processing difficult or even impossible. In practice, the maximum width of the isolation trenches should be limited to 5 μm [Boer et al., 2000].

Figure 2.4(b) shows the electrical connections designed in the tensile stages for electrical measurement of nanostructures. Deep trenches that have the same thickness as the device layer of a SOI wafer serve as electrical insulation between electrodes. Chromium and gold films are deposited on the topside of the device serving as the electrodes. The two terminals of a fixed nanowire are electrically connected to four pads A1, A2, V1 and V2, which are mechanically connected to the support layer of the wafer through the buried SiO_2 layer. To measure the piezoresistance effect in a single nanowire, a constant current is injected into the sample through A1 and A2, and the voltage drop is measured between V1 and V2. Since the uniaxial tensile stress σ is longitudinal and along the same direction as the current flow, the longitudinal piezoresistance coefficient π_l^ρ can be calculated from [He et al., 2006]

$$\pi_l^\rho = \frac{1}{\sigma} \frac{\rho - \rho_0}{\rho_0} \approx \frac{4F_t}{\pi D^2} \left(\frac{V_{1'2'}}{V_{12}} \frac{L}{L'} - 1 \right), \quad (2.3)$$

where ρ_0 and ρ are the sample resistivity under zero and tensile load F_t ($F_t > 0$, measured by the capacitive sensor), and L and L' are the corresponding gauge length of the sample, respectively. V_{12} and $V_{1'2'}$ are the corresponding voltage drops between V1 and V2, respectively. D is the nanowire diameter. During tensile testing, the silicon suspensions and the metal films on top of them are all stretched and both show piezoresistance effects. Their piezoresistance contribution to the value of $V_{1'2'}$ cannot be excluded if only two electrical connections (e.g. A1 and A2) were used to perform a standard I-V measurement. Four electrical connections were therefore designed in this work.

To measure the direct piezoelectric effect in a single nanowire, only two electrical connections (A1 and A2 or V1 and V2) will be used, through which the strain induced charges are measured by a high-sensitivity fast-response charge amplifier. The strain rate of the sample can be controlled through the frequency of the AC drive signal of the comb drive. Considering only the charges induced by the strain in the longitudinal

direction, the short-circuit current i of a piezoelectric nanowire is given by [Wang et al., 2007]

$$i = d_{cc} \frac{\partial F_t}{\partial t}, \quad (2.4)$$

where d_{cc} is the piezoelectric coefficient, and t is the time. Assuming that there is no internal current leak through the nanowire (i.e. the resistance of the nanowire is infinite) and the open loop gain of the amplifier is infinite, the relationship between the input current i and the voltage output V_0 of a charge amplifier is given by

$$i = C_F \frac{\partial V_0}{\partial t} \quad (2.5)$$

where C_F is the feedback capacitance used in the charge amplifier. The piezoelectric coefficient of the nanowire can be calculated from

$$d_{cc} = C_F \frac{\partial V_0}{\partial t} \left(\frac{\partial F_t}{\partial t} \right)^{-1} = C_F \frac{\partial V_0}{\partial F_t}. \quad (2.6)$$

To avoid any injected charges from the primary beam of the SEM/TEM, the electron beam should be blanked during the piezoelectric measurement.

2.1.2 General concept of the system

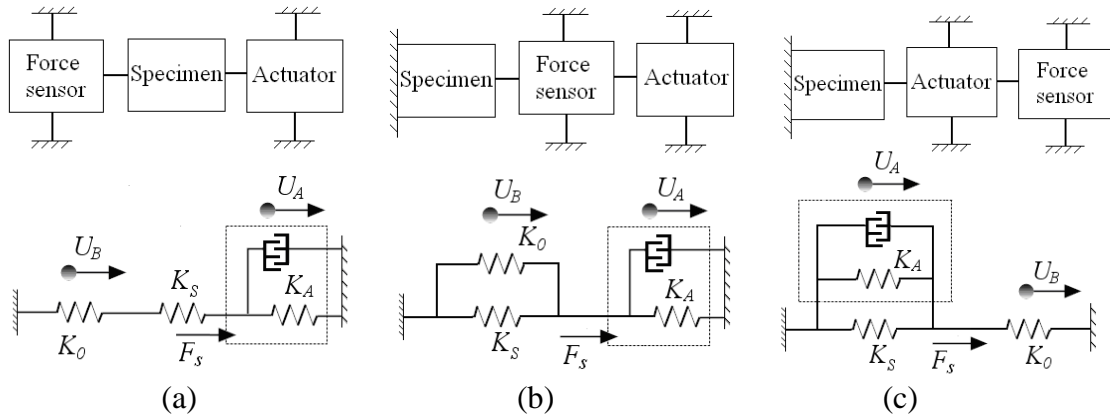


Figure 2.5: Three possible system configurations and their lumped force-displacement models.

Figure 2.5 shows three possible system configurations and their lumped force-displacement models of a tensile stage. The first configuration was adopted in this thesis since the force sensor can measure the tensile load directly; as it connects to the specimen in series. Detailed analytical analysis of this configuration will be given in Section 2.4.1. In the system configurations shown in figure 2.5(b) and (c), the actuator, force sensor and specimen have the same displacements under actuation. When there is no specimen residing on this stage, the sensor displacement is

$$x_1 = \frac{F_e}{K_A + K_0}, \quad (2.7a)$$

where K_S , K_A and K_0 are the stiffness of the specimen, actuator and sensor, respectively, F_e is the electrostatic force generated in the actuator. When a specimen is mounted on the stage and connected to the force sensor, the sensor displacement (under the same drive voltage) is

$$x_2 = \frac{F_e}{K_A + K_0 + K_S}. \quad (2.7b)$$

Combining equations 2.7a and 2.7b, the tensile force F_s deposited in the specimen can be calculated as

$$F_s = K_S x_2 = (x_1 - x_2)(K_A + K_0). \quad (2.8)$$

The configurations in figure 2.5(b) and (c) are not adopted in our design since they are not as straightforward as the first one.

2.2 Design of comb drive actuator

According to equation 2.2, increasing the aspect ratio (i.e. h/g) and number of comb fingers n can increase F_e , and therefore F_s . In our design, actuators with $h/g = 20$ ($h = 100 \mu\text{m}$, $g = 5 \mu\text{m}$) and $n = 240$ and 160 were designed to achieve different force outputs. Another way to increase F_e without increasing the device footprint is to decrease the size of each finger. However, when the size of comb fingers scales down, the basic assumptions for equation 2.2 may lose validity. For such cases, more comprehensive electrostatic models such as those proposed in [Johnson et al., 1995] and [Yeh et al., 2000] have to be adopted. However, extraction of the dependence of all the geometrical parameters on F_e from these models tends to be complicated and indirect.

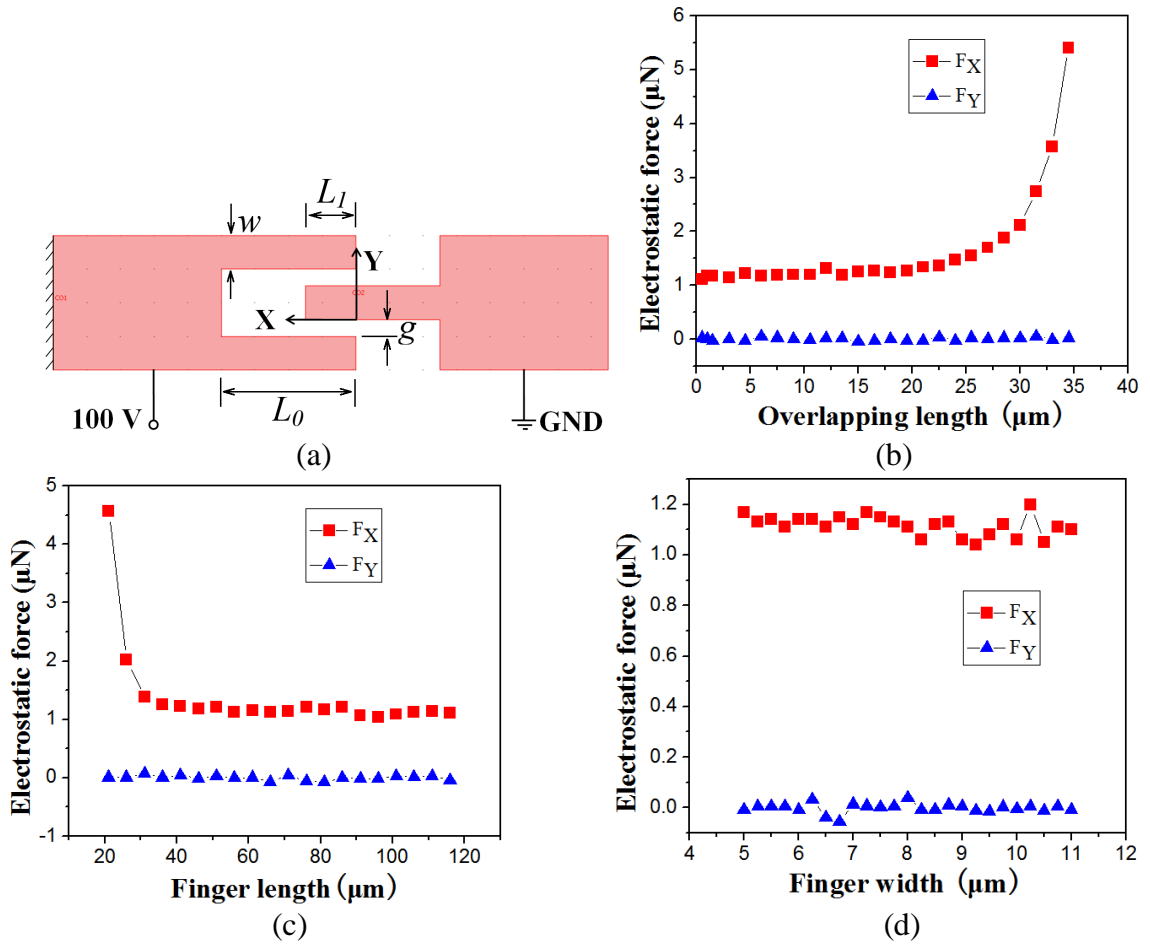


Figure 2.6: FEA model and results for the electrostatic force of a comb-drive actuator. (a) 2D model of one finger pair (the bounding box around the fingers is omitted). (b) Calculated electrostatic force versus overlapping length at $w = 10 \mu\text{m}$, $g = 5 \mu\text{m}$ and $L_0 = 40 \mu\text{m}$. (c) Calculated electrostatic force versus finger length at $w = 10 \mu\text{m}$, $g = 5 \mu\text{m}$ and $L_I = 15 \mu\text{m}$. (d) Calculated electrostatic force versus finger width at $g = 5 \mu\text{m}$, $L_I = 15 \mu\text{m}$ and $L_0 = 40 \mu\text{m}$. The height of the comb fingers is $100 \mu\text{m}$ and the drive voltage is 100 V .

FEA using COMSOL Multiphysics was executed to calculate the electrostatic force at various geometries of comb fingers (i.e. at different finger lengths, widths, and overlapping lengths) to implement the geometry optimization. A 2D model for one finger pair was constructed in COMSOL as shown in [figure 2.6\(a\)](#). There are three types of boundary conditions in the electrostatic model: zero charge/symmetry boundary condition on the bounding box (not shown), electrical potential of 100 V on the fixed fingers, and the ground boundary condition on the movable fingers. The 2D model was partitioned into triangular elements with a predefined mesh size of “Extra fine”. The

relative permittivity (isotropic) of Si and the surrounding air used in this model were 11.7 and 1, respectively. MATLAB was used to program the model, for different overlapping lengths L_l , finger lengths L_0 and widths w , by adding repetitive loops and arrays around the code created by COMSOL. This arrangement allowed faster data capture without having to construct new models every time.

The calculated electrostatic forces along the X- and Y-directions are plotted in [figure 2.6\(b\)](#), [\(c\)](#) and [\(d\)](#). [Figure 2.6\(b\)](#) shows that F_e does not change with respect to L_l until $\sim 30 \mu\text{m}$ (the other parameters are fixed as $w = 10 \mu\text{m}$, $g = 5 \mu\text{m}$ and $L_0 = 40 \mu\text{m}$) position. Note that a sharp increase of F_e may result in front pull-in [[Jaecklin et al., 1992](#)] of the actuator, which should be avoided in the operation of a tensile stage. [Figure 2.6\(c\)](#) shows that when $L_0 < 25 \mu\text{m}$, F_e becomes quite large due to the fringing field (the other parameters are fixed as $w = 10 \mu\text{m}$, $g = 5 \mu\text{m}$ and $L_l = 15 \mu\text{m}$) and the front pull-in might occur. As indicated in [figure 2.6\(d\)](#), w ranging from 5 to 11 μm has little influence on F_e (the other parameters are fixed as $g = 5 \mu\text{m}$, $L_l = 15 \mu\text{m}$ and $L_0 = 40 \mu\text{m}$). Taking into account the under-etching of comb fingers during DRIE, the in-plane bending stiffness of individual fingers [[Elata et al., 2007](#)], and simplicity of the layout design, the comb finger geometry were set to $w = 10 \mu\text{m}$, $L_0 = 40 \mu\text{m}$ and $L_l = 15 \mu\text{m}$. $g = 5 \mu\text{m}$ was fixed as the minimum feature size of the fabrication process.

It is worth noting that micro-leverage based force amplification mechanism could be used to increase the actuation force in comb drives [[Krijnen et al., 2003](#)]. However, this mechanism is not as suitable for the designed stage configuration here because: (1) the output system of the micro-lever, i.e. the specimen and the force sensor connected in series, has low axial stiffness (which equals $1/(K_S^{-1} + K_0^{-1}) \approx K_0$) that will decrease the amplification factor dramatically [[Su, 2001](#)] compared to that of an ideal lever; (2) the force amplification is at a cost of actuator displacement that needs much longer comb fingers and thus increases the device foot-print; (3) the flexure pivots of a micro-lever will consume a portion of the electrostatic force. Therefore, force amplification mechanisms are not adopted in this work.

Levitation effect is a typical (normally unwanted) phenomenon in surface micromachined comb drives, which describes the out-of-plane movement of the movable fingers due to an unbalanced electric field distribution around the suspended structures

[Tang et al., 1989]. The imbalance in the field distribution results in a net vertical force, which levitates the structure away from the substrate. Whether this force causes significant static displacement or excites a vibration mode of the structure depends on the compliance of the suspension and the quality factor for vertical displacements. Levitation effects should be eliminated in tensile testing, since the out-of-plane movement induces bending in the specimen. To eliminate the levitation effect, the substrate beneath the comb drives is removed completely by DRIE in our fabricated MEMS devices. Figure 2.7(a) and (b) show the electric field around the comb fingers with and without a ground plane beneath the structure, respectively, obtained by an electrostatic analysis based on FEA (COMSOL multiphysics). It is clearly seen that the electric field around the movable fingers are symmetric in figure 2.7(a), which demonstrates that removing the substrate eliminates the vertical levitation force efficiently.

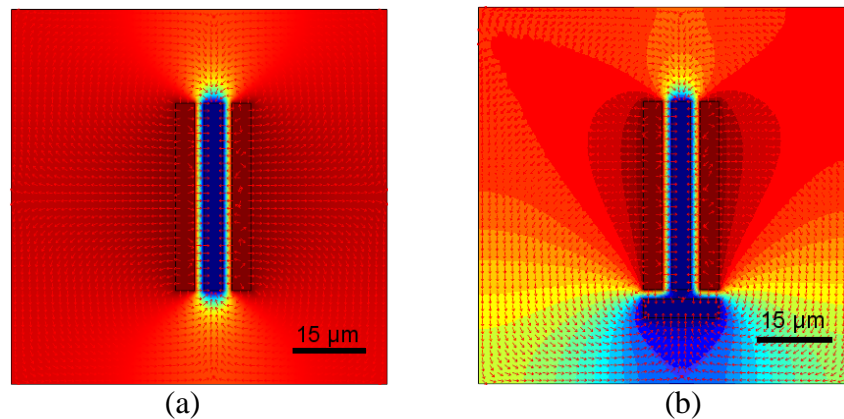


Figure 2.7: Simulation of electronic field around comb fingers ($L_0 = 40 \mu\text{m}$, $w = 10 \mu\text{m}$, $g = 5 \mu\text{m}$, the ground plane is $5 \mu\text{m}$ far away from movable fingers, and the drive voltage is 50 V). Electric field of comb fingers (a) without a ground plane and (b) with a ground plane.

2.3 Design of force sensor

Two kinds of force sensors are designed in the developed nanotensile stages, namely, a clamped-clamped beam force sensor and a triplate differential capacitive sensor. The suspensions' stiffness of the clamped-clamped beams and folded flexures are analytically determined by selecting beam sizes according to the small deflection elastic

beam theory. During the operation of a capacitive sensor, an electrical excitation signal is needed to detect the capacitance change. The parasitic force has direct influence on the sensor's stability, linearity and sensitivity. Analytical expressions for studying these effects are derived and discussed.

2.3.1 Suspensions of force sensors

A properly designed flexure should not only have a specified stiffness in the intended direction, but also constrain the motion in all of the other directions. The selection of a clamped-clamped beam as a load sensor in the tensile stage is mainly due to its simple architecture and the high stiffness ratio of axial to lateral directions. Folded flexures are incorporated in the capacitive sensor owing to their low stiffness. Figure 2.8(a), (b) and (c) show the schematics of a guided-end cantilever beam, clamped-clamped flexures, and folded flexures, respectively. The analytical formulas for describing their stiffness are presented in the following.

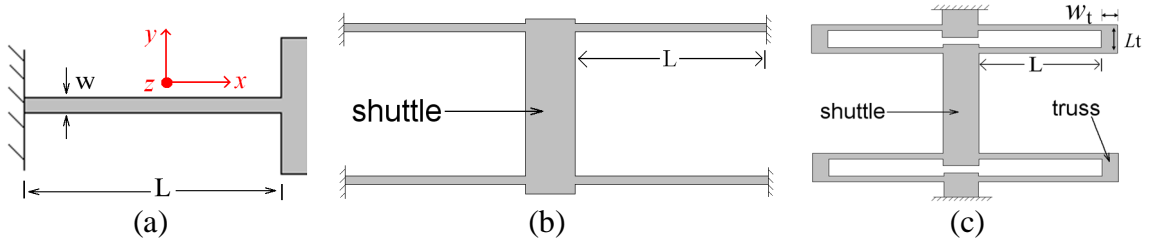


Figure 2.8: Schematics of (a) a guided-end cantilever, (b) clamped-clamped beams, and (c) folded flexures.

A. Guided-end cantilever

Based on the small deflection elastic beam theory for a slender beam (generally length/width>10), the spring constants of a guided-end cantilever, as shown in figure 2.8(a), in three directions are given by

$$K_{y,beam} = \frac{12EI_{z,beam}}{L^3} = \frac{Ehw^3}{L^3} \quad (2.9a)$$

$$K_{x,beam} = \frac{Ehw}{L} \quad (2.9b)$$

$$K_{z,beam} = \frac{12EI_{y,beam}}{L^3} = \frac{Ewh^3}{L^3}, \quad (2.9c)$$

where E is the Young's modulus of the structural material, L , w , h are the length, width and thickness of the beam, respectively; $I_{z, beam}$ and $I_{y, beam}$ are the second moment of inertias for the rectangular beam cross sections about the z- and y-directions.

B. Clamped-clamped beams

The spring constants of the clamped-clamped flexures with a very rigid shuttle, as shown in [figure 2.8\(b\)](#), in three directions are given by

$$K_{y,clamped} = 4 \times k_{y,beam} = \frac{4Ehw^3}{L^3} \quad (2.10a)$$

$$K_{x,clamped} = 4 \times K_{x,beam} = 4Ehw/L \quad (2.10b)$$

$$K_{z,clamped} = 4 \times K_{z,beam} = \frac{4Ewh^3}{L^3} \quad (2.10c)$$

According to the designed geometry of the clamped-clamped beams ($w=5-10 \mu\text{m}$, $h=100 \mu\text{m}$, and $L=750-850 \mu\text{m}$), the relationship of $K_{x,clamped} \ll K_{y,clamped} \ll K_{z,clamped}$ is valid, which ensures that the specimen is loaded uniaxially. Note that the above equations are only valid for small deflection, which is generally defined as the regime of beam deflection/length < 5%. However, the linearity of the clamped-clamped beam can also be related to the beam thickness h . It is found that the small deflection theory is not valid for deflections more than a quarter of the beam thickness (i.e. $h/4$) in [[Legtenberg et al., 1996](#)]. For large displacements, extensional axial forces develop in the beams, resulting in a nonlinear effect which strongly increases the stiffness of the beam with increasing deflection. A derivation of the large deflection behavior of double clamped beams can be found in [[Frisch-Fay, 1962](#)].

C. Folded flexures

The spring constants of folded flexures with a very rigid shuttle, as shown in [figure 8\(c\)](#), in three directions are given by [[Allen, 2005](#); [Huang et al., 2002](#); [Fedder, 1994](#)]

$$K_{y,folded} = \frac{12EI_{z,beam}(2\alpha L + L_t)}{\alpha L^4 + 2L_t L^3} = \frac{Ehw^3}{L^3} \frac{2\alpha L + L_t}{\alpha L + 2L_t} \quad (2.11a)$$

$$K_{x,folded} = 12EI_{z,beam} \times \frac{\alpha}{L_t^2(L_t + 6\alpha L)} = \frac{Ehw^3}{L_t^2} \frac{\alpha}{L_t + 6\alpha L} \quad (2.11b)$$

$$K_{z,folded} = \frac{48}{\frac{8L^3(\beta^2 L^2 + \beta LL_t + L_t^2)}{EI_{y,beam}(2\beta L + L_t)^2} + \frac{L_t^3}{EI_{x,truss}} + \frac{6LL_t^2}{GJ} + \frac{12\beta^2 L^4 L_t}{GJ_{truss}(2\beta L + L_t)^2}}, \quad (2.11c)$$

where $\alpha = I_{z,truss} / I_{z,beam} = (w_t / w)^3$, L_t and w_t are the length and width of the truss, respectively; $I_{z,truss}$ is the second moment of inertia for the rectangular cross section of the truss about the z-direction, J and J_{truss} are the polar moment of inertias of the beam and the truss, respectively; G is the shear modulus and $\beta = GJ_{truss} / EI_{y,beam}$. When the truss is much stiffer than the flexible beam (i.e. $\alpha \gg 1$) and $L \gg L_t$, equations 2.11 reduce to

$$K_{y,folded} \approx \frac{2Ehw^3}{L^3} \quad (2.12a)$$

$$K_{x,folded} \approx \frac{Ehw^3}{6LL_t^2} \quad (2.12b)$$

$$K_{z,folded} \approx \frac{24EI_{y,beam}}{L^3} = \frac{2Ewh^3}{L^3}. \quad (2.12c)$$

Comparing equation 2.12a with 2.10a, it is seen that lower stiffness of the capacitive sensor can be achieved with folded flexures than that with clamped-clamped beams. Another feature of the folded flexures is the enlarged linear moving range (up to approximately 10% of the beam length) due to the strongly reduced axial forces, which makes folded flexures very suitable for large deflection actuators. However, the disadvantages of folded flexures are the reduced stiffness in the undesired directions and occupying larger area. According to the designed geometries of the trusses ($w_t = 50 \mu\text{m}$, $h = 100 \mu\text{m}$, and $L_t = 70\text{-}80 \mu\text{m}$) and folded-flexure beams ($w = 5\text{-}10 \mu\text{m}$, $h = 100 \mu\text{m}$, and $L = 750\text{-}850 \mu\text{m}$), $K_{x,folded} / K_{y,folded} \geq 30$ was achieved. Note that a meander spring (or called U spring) could have lower stiffness than folded flexures in the y-direction, but the transverse stiffness is seriously degraded in a meander spring [Fedder, 1994], and therefore, it is not adopted in our design.

2.3.2 Triplate differential capacitive force sensor

Figure 2.9 shows the configuration of the differential triplate capacitive sensor [Sun et al., 2005] employed in the testing devices. As the heights of the capacitive plates are

much larger than the gaps among them, the electrostatic fringing field is negligible. The capacitance change ΔC of the movable electrodes due to a displacement x is given by

$$\Delta C = N(C_2 - C_1) = 2N\epsilon_0 Ax \left(\frac{1}{d_1^2 - x^2} - \frac{1}{d_2^2 - x^2} \right), \quad (2.13)$$

where N , ϵ_0 , A , d_1 and d_2 are the number of sensor unit, the permittivity of free space, the overlapping area of the sensing electrodes and the initial gaps between the plates, respectively. For differential capacitive sensors, opposite excitation with a capacitive feedback sensing scheme is often used because of the efficiency to mitigate the parasitic capacitance [Bao, 2005], where sensor output V_{out} is linearly dependent on ΔC and can be given by

$$V_{out} = aV_e\Delta C = 2aN\epsilon_0 AV_e x \left(\frac{1}{d_1^2 - x^2} - \frac{1}{d_2^2 - x^2} \right), \quad (2.14)$$

where V_e is the effective voltage of the excitation signal on the sensing electrodes, a is a constant that depends on the interface electronics.

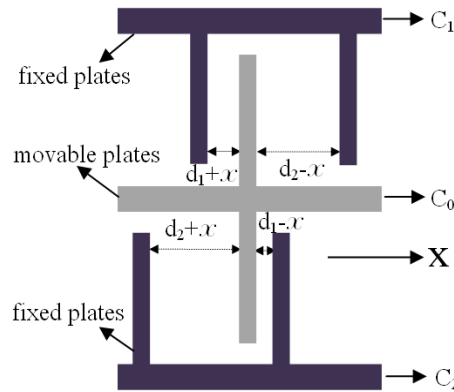


Figure 2.9: Schematic view of one unit of a triplate capacitive sensor (not to scale).

The excitation signal frequency (100 kHz in our application) is much higher than the resonance frequency of the capacitive sensor (see Section 4.1), so the electrostatic force F_E that stems from the excitation signal of the movable electrodes can be written as the average of the parasitic force and given by [Bao, 2005]

$$F_E = 2N\epsilon_0 AV_e^2 x \left[\frac{d_2}{(d_2^2 - x^2)^2} + \frac{d_1}{(d_1^2 - x^2)^2} \right]. \quad (2.15)$$

During tensile tests, the load applied to the specimen is considered as quasi-static, and therefore the relation between the equilibrium position of the movable plate and the external force F_t is

$$F_t = \{K_0 - 2N\epsilon_0AV_e^2[\frac{d_2}{(d_2^2 - x^2)^2} + \frac{d_1}{(d_1^2 - x^2)^2}]\}x . \quad (2.16)$$

Equation 2.16 shows the parasitic force has a stiffness softening effect, which introduces non-linearity in the suspension beams. When K_0 is not large enough and comparable with the nonlinear coefficient (i.e. $2N\epsilon_0AV_e^2[\frac{d_2}{(d_2^2 - x^2)^2} + \frac{d_1}{(d_1^2 - x^2)^2}]$), e.g. for nanomechanical testing applications, the effect of the parasitic force can not be neglected. This effect can change the sensor's stability, linearity and sensitivity and will be discussed in the following.

A. Stable working range

In equation 2.16, if $F_t = 0$, $x = 0$ is an equilibrium position of the movable plate. When the sensor stiffness becomes very small the parasitic force will possibly snap the capacitive plates together (pull-in). At a given excitation signal, the minimum stiffness K_{PI} is determined by the pull-in point at $F_t = 0$ from the following equations

$$\left\{ \begin{array}{l} F_t = -2N\epsilon_0AV_e^2[\frac{d_2x_{PI}}{(d_2^2 - x_{PI}^2)^2} + \frac{d_1x_{PI}}{(d_1^2 - x_{PI}^2)^2}] + x_{PI}K_{PI} = 0, \\ \frac{\partial F_t}{\partial x_{PI}} = 0 \end{array} \right. \quad (2.17a)$$

$$\quad (2.17b)$$

Then we can get

$$K_{PI} = 2N\epsilon_0AV_e^2 \frac{d_1^3 + d_2^3}{d_1^3 d_2^3} x_{PI} = 0 . \quad (2.18)$$

To find the relationship between the external force ($F_t \neq 0$) and the associated equilibrium position, a graphical method is used. Assuming $\delta = 2N\epsilon_0AV_e^2(K_0d_1^3)^{-1}$ which denotes the ratio between the parasitic force and the mechanical restoring force, $\varphi = 2aN\epsilon_0A(3C_Fd_1)^{-1}$ and $d_2/d_1 = 5$, the static equilibrium positions of the sensor obtained from equation 2.16 are plotted in figure 2.10 at $0 \leq x/d_1 \leq 1$. Curves at

$-1 \leq -V_{out} / \varphi V_e \leq 0$ plot the sensor output versus the external force by solving equations 2.14 and 2.16.

There is a stable branch (solid line) and an unstable branch (dashed line) in all the curves of figure 2.10. The maximum value of $F_t / (K_0 d_1)$ in each curve indicates the pull-in force, i.e. the maximum force can be measured by the capacitive sensor. For forces above the pull-in force, the sensor has no equilibrium position. The equilibrium position associated with $F_t / (K_0 d_1)_{max}$ is the pull-in displacement, i.e. the sensor's maximum stable displacement. Beyond that position, the restoring mechanical force of the spring cannot overcome the parasitic force, thus pull-in occurs. It is shown that decreasing the value of δ can increase the pull-in displacement, which can be realized by reducing N and A and increasing K_0 and d_1 . Based on this analysis, for a given sensor geometry (e.g. $N = 30$, $A = 5 \times 10^4 \mu\text{m}^2$, $d_1 = 5 \mu\text{m}$ and $d_2 = 25 \mu\text{m}$) and excitation signal (e.g. $V_e = 2.25 / \sqrt{2}$ V), the stable working range can be computed (to be $2.4 \mu\text{m} / 4.8 \mu\text{N}$ and $4.5 \mu\text{m} / 315 \mu\text{N}$) from the designed stiffness (e.g. 2 N/m and 70 N/m , respectively) for testing nanostructures of different stiffness.

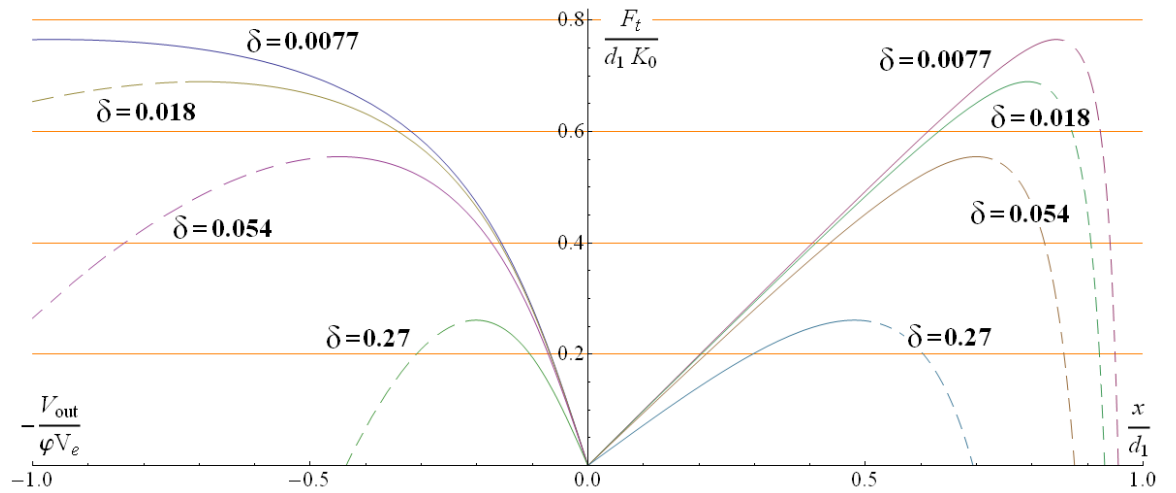


Figure 2.10: Graphical solutions for the displacement-external force and external force-output relationships.

B. Linearity analysis

Capacitive sensors can be used for displacement or force measurement. Using terminal linearity definition [Yamada et al., 1982], their non-linearity can be calculated from equations 2.14 and 2.16. For displacement measurement,

$$NL(\tilde{x})_D = \frac{\tilde{x}}{\tilde{x}_m} \left[\left(\frac{1}{1-\tilde{x}^2} - \frac{1}{\beta^2 - \tilde{x}^2} \right) \left(\frac{1}{1-\tilde{x}_m^2} - \frac{1}{\beta^2 - \tilde{x}_m^2} \right)^{-1} - 1 \right]. \quad (2.19)$$

For force measurement,

$$NL(\tilde{x})_F = \frac{\tilde{x}}{\tilde{x}_m} \left\{ \left(\frac{1}{1-\tilde{x}^2} - \frac{1}{\beta^2 - \tilde{x}^2} \right) \left(\frac{1}{1-\tilde{x}_m^2} - \frac{1}{\beta^2 - \tilde{x}_m^2} \right)^{-1} - \left[1 - \delta \left(\frac{\beta}{(\beta^2 - \tilde{x}^2)^2} + \frac{1}{(1-\tilde{x}^2)^2} \right) \right] \left[1 - \delta \left(\frac{\beta}{(\beta^2 - \tilde{x}_m^2)^2} + \frac{1}{(1-\tilde{x}_m^2)^2} \right) \right]^{-1} \right\}, \quad (2.20)$$

where $\tilde{x} = x/d_1$, $\beta = d_2/d_1$, and $\tilde{x}_m = x_m/d_1$ is the value under full range displacement.

Table 2.1: Calculated maximum non-linearity for (a) displacement and (b) force measurements.

		(a)			
		$\beta = 3$	$\beta = 4$	$\beta = 5$	
$\tilde{x}_m = 0.2$		1.73%	1.65%	1.62%	
$\tilde{x}_m = 0.3$		3.94%	3.78%	3.70%	
$\tilde{x}_m = 0.4$		7.13%	6.86%	6.74%	
$\tilde{x}_m = 0.5$		11.45%	11.06%	10.88%	
		(b)			
$(\beta = 4)$	$\delta = 0.0077$	$\delta = 0.018$	$\delta = 0.054$	$\delta = 0.27$	
$\tilde{x}_m = 0.2$		3.11%	3.14%	3.24%	4.11%
$\tilde{x}_m = 0.3$		5.09%	5.17%	5.47%	8.15%
$\tilde{x}_m = 0.4$		8.08%	8.26%	8.94%	15.36%
$\tilde{x}_m = 0.5$		12.23%	12.60%	13.99%	Pull-in

Comparing equation 2.19 with 2.20, $NL(\tilde{x})_F$ is higher than $NL(\tilde{x})_D$ under the same excitation signal V_e , working range \tilde{x}_m and sensor geometry (i.e. d_1 , d_2 , N and A). It is seen that $NL(\tilde{x})_F$ and $NL(\tilde{x})_D$ both decrease as full working range \tilde{x}_m increases and as initial gap ratio β decreases. Additionally, the maximum value of $NL(\tilde{x})_D$ under different \tilde{x}_m and β are obtained numerically from equation 2.19 and collected in table

2.1(a). With an assumption of $\beta = 4$, the maximum value of $NL(\tilde{x})_F$ under different \tilde{x}_m and δ are computed from [equation 2.20](#) and collected in [table 2.1\(b\)](#). At a given working range \tilde{x}_m and the maximum non-linearity within that range, data in [table 2.1](#) can be used to determine the value of β and δ , and therefore to optimize the sensor's geometry.

C. Sensitivity analysis

Sensor sensitivity is defined as the sensor output change per unit displacement (for displacement measurement) or per unit external force (for force measurement). From [equations 2.14](#) and [2.16](#), capacitive sensor output is not a linear function of the displacement or the external force, thus the sensitivity changes as the sensor moves. Therefore, when an average sensitivity is calculated or measured, the corresponding working range should be indicated. If $\tilde{x}^2 \ll 1$, i.e. at small displacement range, the displacement and force sensitivity determined from [equations 2.14](#) and [2.16](#) are nearly constant and expressed as

$$\frac{\partial V_{out}}{\partial x} = \frac{2aN\varepsilon_0AV_e}{d_2^2}(\beta^2 - 1) \quad (2.21)$$

$$\frac{\partial V_{out}}{\partial F_t} = 2aN\varepsilon_0AV_e d_2(\beta^2 - 1)[K_0 d_2^3 - 2N\varepsilon_0AV_e^2(\beta^3 + 1)]^{-1} . \quad (2.22)$$

Assuming d_2 is fixed, it is seen that increasing the value of β (i.e. decreasing d_1) and $2aN\varepsilon_0AV_e$ will both increase the sensor sensitivities. However, since the value of $\delta = 2N\varepsilon_0AV_e^2(K_0 d_1^3)^{-1}$ is increased at the same time, the sensor's stability and linearity is reduced as discussed before. Therefore, there should be a tradeoff between the stability, linearity and sensitivity. [Equation 2.22](#) also shows the smaller K_0 the higher the load resolution. In practice, the selection of K_0 is related to the strength of the tested specimen. For example in the developed tensile testing stage, a larger K_0 is desirable for stiffer specimen to avoid an excessively large displacement for an incremental tensile force until the specimen fracture. In addition to the sensor architecture, the interface electronics also play an important role to achieve high sensitivities. To improve the value of a in [equations 2.21](#) and [2.22](#), a highly sensitive interface electronics that is immune from parasitic capacitance is desirable [[Boser, 1997](#)].

2.4 Modeling of the whole system

2.4.1 Static analysis

The lumped force-displacement model of the system is shown in [figure 2.5\(a\)](#), where K_A , K_S , and K_0 are the stiffness of the comb drive actuator, the specimen, and the force sensors, respectively; U_A and U_B are the displacements of the actuator and the load sensor under actuation, respectively. At equilibrium, the governing equations of the lumped system are given as following:

$$U_A = \Delta U_s + U_B \quad (2.23a)$$

$$U_A = \frac{F_e - F_s}{K_A} \quad (2.23b)$$

$$K_{S0} = \left(\frac{1}{K_S} + \frac{1}{K_0} \right)^{-1} = \frac{K_S \cdot K_0}{K_S + K_0} \quad (2.23c)$$

$$F_s = F_B = \frac{K_{S0}}{K_A + K_{S0}} \cdot F_e \quad (2.23d)$$

$$F_B = K_0 \cdot U_B \quad (2.23e)$$

$$F_e = n\epsilon_0 \cdot \frac{h}{g} \cdot V^2, \quad (2.23f)$$

where ΔU_s is the elongation of specimen under the tensile force F_s , F_e is the electrostatic force generated in the actuator, F_B is the force applied on the force sensor, K_{S0} is the composition of K_S and K_0 , g , h and n , are the gap, the thickness and the number of the comb fingers, respectively, ϵ_0 and V are the permittivity of the air and the driving voltage, respectively. From [equations 2.23](#), the tensile force and the deflection of force sensor U_B can be expressed as following:

$$F_s = \frac{1}{(K_A / K_0) + (K_A / K_S) + 1} \cdot n\epsilon_0 \cdot \frac{h}{g} \cdot V^2, \quad (2.24a)$$

$$U_B = \frac{1}{(K_A / K_0) + (K_A / K_S) + 1} \cdot n\epsilon_0 \cdot \frac{h}{g} \cdot V^2 \frac{1}{K_0}. \quad (2.24b)$$

It can be seen that the smaller K_A , the more F_s . Folded flexures are therefore adopted as suspensions in comb drives since they have lower stiffness than straight fixed-fixed

beams given the same beam sizes. However, when K_A becomes very small, the device will be susceptible to the front sticking, which is discussed in the following.

During tensile testing, the specimen elongation and tensile force right before fracture is difficult to capture in SEM images owing to the stepwise increasing drive voltage, which leads to an underestimation of the specimen strength. This is more pronounced when the front sticking occurs in a comb-drive actuator, since a small increase of the drive voltage leads to a very large increase of the electrostatic force, which can cause a large error in the material strength measurement. The side pull-in has never been observed in our tests, since it happens at a higher voltage than the front pull-in, which is a typical case for comb drives with short fingers and small K_A . The front pull-in condition of a comb-drive actuator can be predicted from [Jaecklin et al., 1992]

$$K_{\Sigma}x_P = F_c + 2F_P \quad (2.25a)$$

$$K_{\Sigma} = \frac{\partial(F_c + 2F_P)}{\partial x_P}, \quad (2.25b)$$

where x_P is the pull-in displacement (i.e. the stable moving range) of the actuator, $F_c = \epsilon_0nhV_P^2/g$ is the electrostatic force of the actuator at pull-in voltage V_P without considering the fringing field, $F_P = V_P^2\epsilon_0nhw(L_0 - L_1 - x_P)^{-2}/2$ is the electrostatic force between the far ends of the movable fingers and the roots of the fixed set of fingers (which form capacitors with parallel plates) as shown in figure 2.11, and K_{Σ} is the system stiffness that is a composition of the actuator and sensor stiffness and is given by $K_{\Sigma} = K_A + K_0$ (here it is assumed that $K_0 \ll K_S$, i.e. the specimen deformation is negligible compared with the sensor displacement). Dividing equations 2.25b by 2.25a, we obtain

$$x_P = \frac{1 + wg(L_0 - L_1 - x_P)^{-2}}{2wg(L_0 - L_1 - x_P)^{-3}} \quad V_P = \sqrt{\frac{(K_A + K_0)(L_0 - L_1 - x_P)^3}{2\epsilon_0nhw}}. \quad (2.26)$$

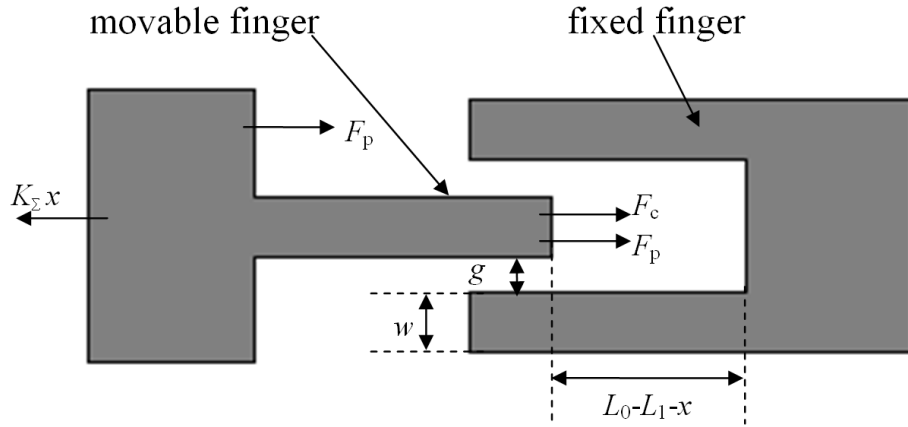


Figure 2.11: Schematic of one pair of comb fingers for front-sticking analysis.

Assuming $w=10\ \mu\text{m}$, $g=5\ \mu\text{m}$, $L_0=40\ \mu\text{m}$, and $L_1=15\ \mu\text{m}$, x_P is computed to be $15.0\ \mu\text{m}$, which agrees very well with the simulation result shown in figure 2.6(b) (where a sharp increase of F_c is observed at a overlapping length of about $30\ \mu\text{m}$). From equation 2.26, it can be seen that a small K_A will result in a small V_P . However, the maximum tensile force at the moment of front pull-in that can be deposited in the specimen (assuming $K_S \gg K_0$) would not change, since x_P (which is independent on K_A) is not changed. Taking account of the robustness of the suspended structures, the actuator stiffness in four different prototypes was selected close to the sensors' stiffness (See table 4.1). Therefore, about half of the total electrostatic force can be deposited in the specimen (assuming $K_S \gg K_0$).

From equation 2.24, F_s is dependent on the specimen stiffness K_S . Therefore, the optimization of the testing stage needs the prior-information of the tested sample. For this reason, four prototypes of the stages with different actuator and sensor stiffness and different number of comb fingers have been developed for testing nanostructures of different stiffness (labeled with device #1-#4, see Chapter 4).

In general, a small K_0 is required to achieve high force sensitivity. However, reduced K_0 leads to lower F_s as seen in equation 2.24a. Thus, a trade-off must be made between the sensor sensitivity and the applicable tensile force. One possible method to address this issue is to design a force sensor with tunable stiffness, which could be realized by engaging or disengaging several flexures that are arranged in parallel in the loading direction [Clemens, et al., 2006]. In practice, the selection of K_0 has to take into account

the specimen stiffness K_S , e.g. a larger K_0 is desirable for a stiffer specimen, because the displacement range (i.e. the measurable loading range) of a differential capacitive sensor is constrained by its geometry ($x < d_1$, $x < d_2$) and the device instability due to F_E . For a clamped-clamped beam force sensor, a larger K_0 is also necessary for a stiffer specimen to avoid excessively large displacements before specimen fractures. Assuming that the maximum sensor displacement and the maximum specimen deformation are $U_{B-\max}$ and $\Delta U_{S-\max}$, respectively, the front pull-in will not happen in the testing system as long as $U_{B-\max} + \Delta U_{S-\max} < x_P$ is maintained. Then the maximum drive voltage V_{\max} of the actuator is only governed by $U_{B-\max}$ (assuming $K_0 \ll K_S$), can be calculated, in analogy with equation 2.25a, from

$$K_{\Sigma} U_{B-\max} = \varepsilon_0 n h V_{\max}^2 / g + V_{\max}^2 \varepsilon_0 n h w \times (L_0 - L_1 - U_{B-\max})^{-2}, \quad (2.27)$$

and is given by

$$V_{\max} = \sqrt{\frac{U_{B-\max} (K_0 + K_A)}{\varepsilon_0 n h} \left[\frac{1}{g} + \frac{w}{(L_0 - L_1 - U_{B-\max})^2} \right]^{-1}}. \quad (2.28)$$

2.4.2 Dynamic analysis

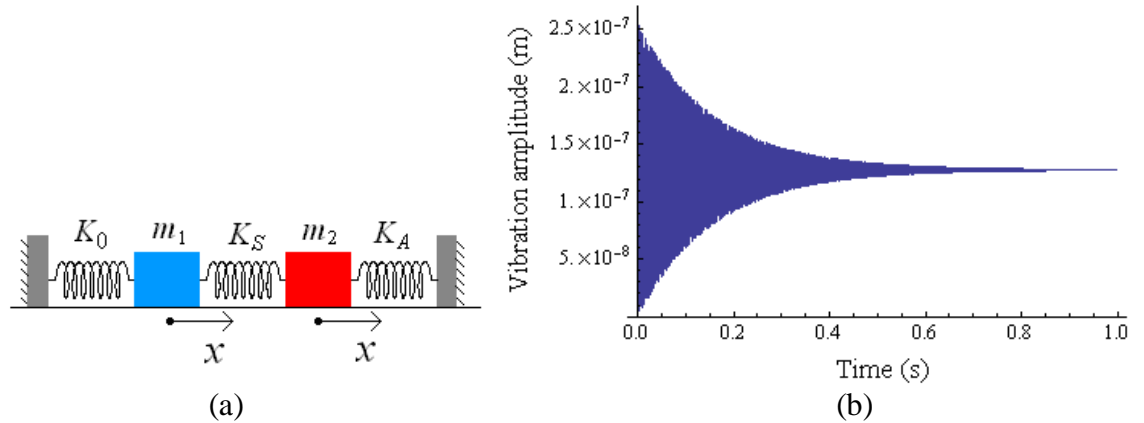


Figure 2.12: (a) A Lumped spring-mass model of the testing stages. (b) A history for the response of the testing system when there is a step increase of the drive voltage.

In quasi-static tensile testing, the stress and strain of the specimen should be measured at equilibrium under various loads. However, each increment of the drive voltage is an impact load on the testing system, which introduces vibrations due to the inertial effect of the actuator and sensor. To determine the necessary relaxation time between each

increment of the drive voltage, the system dynamics has to be studied. Assuming that K_S (for most of tested 1D nanostructures, $K_S \approx 10^2$ - 10^3 N/m) is infinite compared with K_A and K_0 (< 50 N/m, see [Chapter 4](#)), the governing equation of the spring-mass system as shown in [figure 2.12\(a\)](#) are determined by

$$(m_1 + m_2)x''(t) + cx'(t) + (K_0 + K_A)x(t) = n\epsilon_0 \frac{h}{g}(V + \Delta V)^2 - n\epsilon_0 \frac{h}{g}V^2, \quad (2.27)$$

where c is the damping coefficient, and ΔV is the step increase of the drive voltage V . A device (#1) where there was no gap between the actuator and the force sensor was excited into resonance in the vacuum chamber of a SEM, from which its first resonance frequency f and quality factor Q were measured experimentally. Assuming that c is independent on the vibration frequency, c can be given by $c \approx 2(m_1 + m_2)\pi f Q^{-1}$, where m_1 and m_2 are the respective mass of the movable structures of the sensor and actuator and can be calculated from their measured geometries. The estimated values of m_1 , m_2 , c , and the maximum of $[(V + \Delta V)^2 - V^2]$ for device #1 are listed in [table 2.2](#), where K_A , K_0 , n , h/g are the calibrated parameters. With the initial conditions of $x(0)=0$ and $x'(0)=0$, [equation 2.27](#) is solved numerically with Mathematica. [Figure 2.12\(b\)](#) shows that $x(t)$ can exceed 200 nm at the beginning phase of the vibration and nearly stabilize in 1 s. Based on this analysis, the time lag between each increase of the drive voltage is set to 20 s, and the SEM images (for measuring specimen elongation and/or sensor displacement) are always taken with a delay of 15-18 s after a voltage increase to ensure that the system is at equilibrium at the moment of imaging. Note that, to maintain a small tensile force increment and therefore a small overshooting during tests, a much smaller step increase should be used at high voltages than at low voltages since F_e is proportional to V^2 .

Table 2.2: Parameters used in the spring-mass model of device #1.

Parameter	Units	Value
m_1	Kg	4.77×10^{-7}
m_2	Kg	4.56×10^{-7}
K_0	N/m	33.23
K_A	N/m	35.47
c	N·s/m	1.17×10^{-5}
n	-	240
h/g	-	15
$[(V+\Delta V)^2 - V^2]_{\max}$	V^2	275

2.5 Summary

Two novel MEMS-based nanotensile stages are proposed. One consists of a comb-drive actuator and a capacitive force sensor. The other one is composed of a comb-drive actuator and a clamped-clamped beam force sensor. Folded flexures were adopted as the suspension for the comb drives and capacitive sensor, because their stiffness is half of clamped-clamped flexures given the same beam sizes. The influence of the parasitic force arising from the excitation voltage of the sensing electrodes of a capacitive sensor on the sensor's stability, linearity and sensitivity was studied analytically for the first time. From the analytical modeling of the whole system, an actuator of lower stiffness enables more tensile force deposited in the specimen and lower stiffness of a force sensor is required to achieve a high resolution for the force measurement. The selection of sensor stiffness also has to take into account the specimen stiffness, e.g., larger sensor stiffness is desirable for a stiffer specimen to avoid excessively large displacements before specimen fractures. Finally, we studied the dynamics of the whole stage, from which the necessary relaxation time between each increment of the drive voltage was determined to be about 1 s.

3.

Microfabrication and packaging

In this chapter, several layout design issues, detailed micro-fabrication process and the packaging for the designed nanotensile stages are presented. Emphasis is placed on the process challenges of DRIE, including notching effect and the enhanced under-etching (i.e. lateral etching) of the suspended beams induced by thermal effects. The micro-fabrication was performed in the clean room of Center of Micro-/nanotechnology (CMI) at EPFL and adhered to its contamination protocols.

3.1 Layout design issues

The layout is used for the fabrication of optical masks, which can be accomplished by AutoCAD, L-Edit and other graphic software. Several important issues related to the device performance are discussed in the following.

A. Crystal orientation of flexures

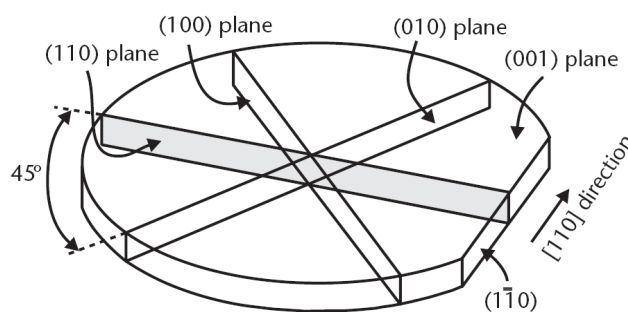


Figure 3.1: Illustration identifying various planes in a Si {100} wafer [Maluf, 2004].

The flexures of comb drives and force sensors should be designed along the same crystal orientation in the wafer, thus the MEMS devices of the same design will have (almost) the same stiffness independent of their locations on the wafer. Figure 3.1 shows the

arrangement of various planes in a Si {100} wafer [Maluf, 2004]. In our design, the longitudinal direction of all the suspensions are parallel to the primary flat of a (100) SOI p-type wafer, i.e. along the [110] direction. Therefore, during tensile testing, all the flexures in the actuators and sensors are bent in $[1\bar{1}0]$ direction. Young's modulus $E=170$ GPa of Si $\langle 110 \rangle$ is used in the analytical prediction of the flexures stiffness.

B. Supporting hinges for dice-free releasing of individual chips from wafer

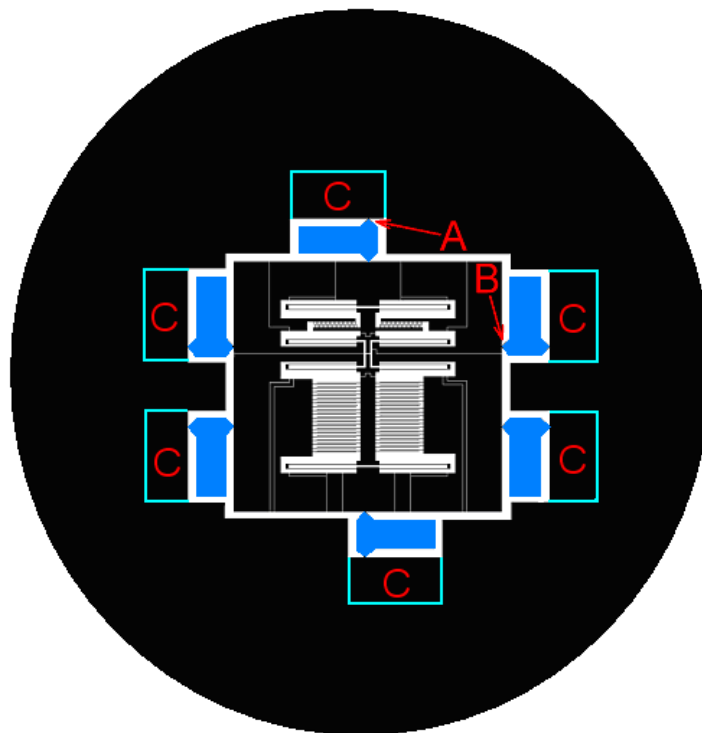


Figure 3.2: Schematic of supporting hinges for dice-free device releasing from a wafer.

Dicing is a general method to separate a wafer into individual chips by using a dicing saw. During the cutting, specially treated water is poured onto the wafer to remove the fine particles generated and also to cool the wafer. A dice-free method should be used to release individual devices from a wafer when the device is fragile and sensitive to dust and stiction problems. Several methods have been reported in the literature to realize dice-free device releasing. One way is to embed the chips in photoresist prior to dicing, thus the mechanical structures are not laid open during dicing [Overstolz et al., 2004]. In

general, this resist layer protects well the fragile structures during dicing but stripping the resist afterwards in acetone and isopropanol is very critical. Dicing debris deposited onto the resist layer during dicing have the tendency to settle down on the silicon surface when the resist is stripped in acetone. This must be avoided since these particles can potentially create short circuits or block moving parts in actuators. In addition, stripping of the resist layer and rinsing is extremely dangerous due to sticking and much effort has to be done to avoid this. Another way to release an individual SOI-based device is to design a rim surrounding the device that defines the footprint of the chip [Overstolz et al., 2004; Sun et al., 2005]. Such a rim is etched on the frontside as well as on the backside of a SOI wafer by DRIE. In this work, dedicated suspended structures which can be easily broken off by applying a small pressure (e.g. with sharp tweezers) were designed around each die, as shown in figure 3.2. The thickness of the connecting points A and B is the thickness of the device layer (100 μm) of the SOI wafer, where the backside substrate is removed during the backside DRIE. The rectangular pads C shown in figure 3.2 are electrically insulated from other parts of the wafer but mechanically connected through the buried SiO_2 layer. Therefore, all electrodes of the MEMS device are electrically insulated, which opens the possibility of probe-based electrical testing of individual devices on the wafer before releasing individual devices.

C. Adjacent sharp tips

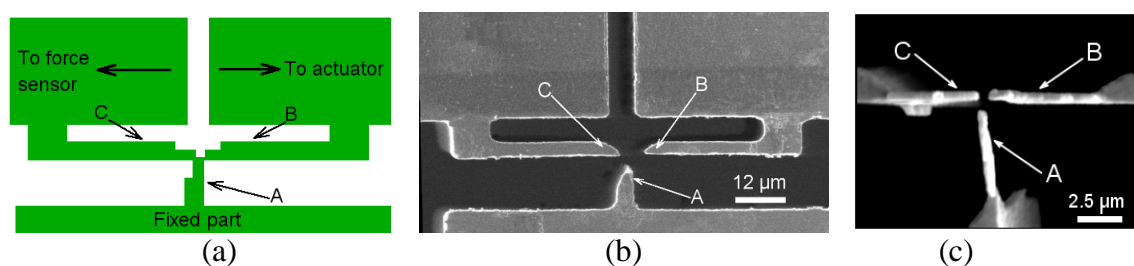


Figure 3.3: (a) Layout of the designed three-beam structure. (b) SEM image of the fabricated structure after clean-room process. (c) SEM image of slender beams fabricated by FIBID.

For the nanotensile stage composed of a comb-drive actuator and a clamped-clamped beam force sensor, a three-beam structure, as shown in figure 3.3, is designed near the

gap on the MEMS device. During tensile tests, the movement of the three-beam structure is recorded in a video file or a series of SEM images, from which the sensor displacement (i.e. the gap change between A and C) and the specimen elongation (i.e. the gap change between B and C) can be measured concurrently [Zhang et al., 2009b]. Since the sensor displacement and specimen elongation are obtained from images analysis, the measurement resolution directly depends on the image pixel size, which is governed by the imaging magnification. Therefore, the beams A, B and C should have very sharp (sub-micrometer) ends and very close to each other (with nanometer range). However, this requirement is constrained by the DRIE process in this work. To address this issue, two strategies were adopted: (1) Over-etching in DRIE was used to improve the lateral resolution. The three beams were initially connected with a tiny joint (2 μm wide) in the layout design as shown in figure 3.3(a), which were separated by the over-etching (larger than 2 μm) in the DRIE as shown in figure 3.3(b). (2) Copper-carbon composite beams were fabricated by FIBID to further reduce the initial gaps among them, as shown in figure 3.3(c). The modified gaps are of sub-micrometer, and therefore the sensor displacement and specimen elongation are increased significantly due to the allowable high magnification during imaging. In our tests, a displacement resolution of better than 10 nm (pixel size at a magnification of 29K) was safely achieved. It is worth noting that a stepwise increase of the DC drive voltage of the actuator could cause severe e-beam drift during testing, thus the sensor deflection cannot be solely treated as the monitored displacement of the beam C, but the displacements difference of the beams A and C.

D. Uniform openings to suppress the notching effect in DRIE

DRIE (also known as Bosch Process) is widely used to fabricate high-aspect-ratio structures in Si, which is based on alternating passivation (by nonvolatile fluorocarbons) and etching (by reactive ions such as F^+). Due to the combination effects of physical sputtering and chemical etching, the commonly observed effects such as RIE lag, notching (or footing) effect, and micro-loading are difficult to control and eliminate [Rangelow et al., 2003]. The etching rate of DRIE has a strong dependence on the trench width, which is called ARDE or RIE lag [Rangelow et al., 2003], as shown in figure 3.4. Wide openings (e.g. gap between suspensions) are usually over-etched when the narrow

openings (e.g. electrical insulation gap) are etched to the desired depth. Notching is caused by a surface charging effect on the oxide layer at the bottom or sidewall of the trench due to poor charge relaxation and a lack of neutralization by electrons during DRIE [Ishihara et al., 1999]. Notching effect could lead to rough and distorted surfaces as well as a non-uniform distribution of mass and stiffness, which could significantly change the design specifications. Furthermore, over-etched structures have poor strength and will have more chance of mechanical failure and poor reliability. A carefully designed layout is necessary to mitigate these effects.

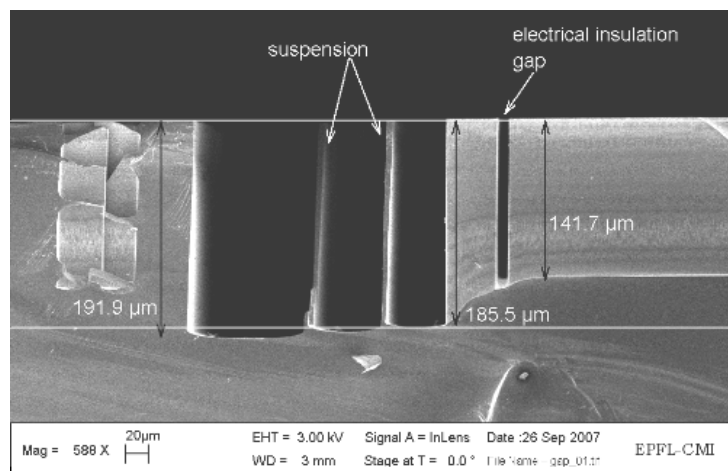


Figure 3.4: SEM image showing the ARDE effect (DRIE of a dummy Si wafer).

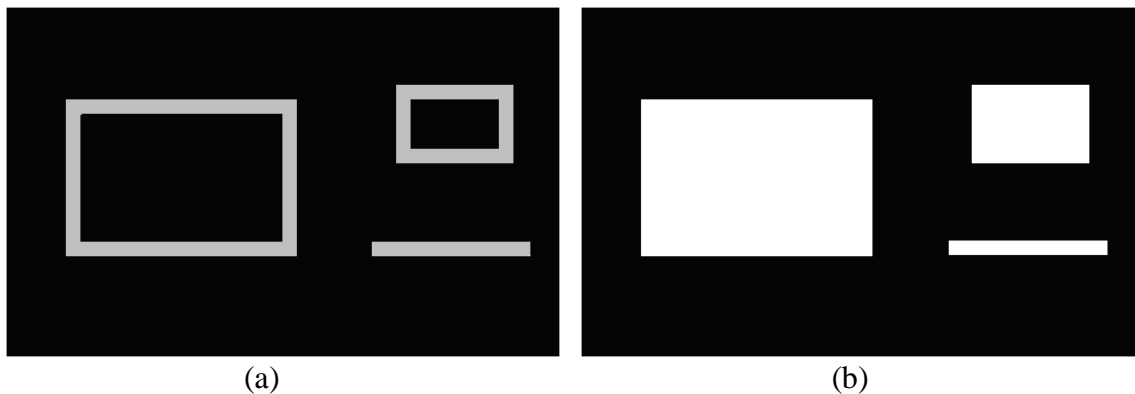


Figure 3.5: Schematics for a halo etch to compensate for differences in etch rate resulting from feature size in through wafer etching. (a) The shaded regions are for etching and (b) the blank regions are the final features.

Ideally, all the patterns should have uniform openings, so that they could be etched to the ending point at the same time. However, this condition is almost impossible to meet in many MEMS designs. In our fabricated prototypes, the smallest opening is 5 μm that is fixed as the minimum feature size of the process. The other large openings are kept as small as possible to suppress the ARDE effect. To further suppress these effects, the “Halo mask” concept proposed in [Khanna et al., 2001] might be used. As schematically shown in figure 3.5(a), only the perimeters of the patterns (i.e. the shaded regions) are etched. The width of this perimeter is fixed at one value for all the features. When the etch punches through (DRIE on both sides of a SOI wafer), the features become separated from the bulk of the wafer and can be mechanically removed, leaving an open area defined by the perimeter etch, i.e. the blank region shown in figure 3.5(b).

E. General issues

1) Under-etching compensation is generally needed for suspensions since their stiffness is proportional to w^3 (w : width of beam). An under-etching of 1 μm in a 8- μm -wide beam (designed value) will result in a decrease of stiffness by 33%.

2) The design should accommodate expected alignment error based on personal skill level and process (2 μm is a safe number).

3) Photoresist that is within 2-5 mm away from the wafer’s edge will be removed in the edge bead removal (EBR) process during photolithography, and also the edges of wafers are frequently touched by a wafer cassette or mechanical clamping during process. Hence, any masks or patterns should not be placed in this zone.

4) The DRIE over a wafer is not uniform and tends to etch the edges of the wafer faster than the center of the wafer in a radially symmetric pattern. Structures with larger features should be placed closer to the wafer edge than those with small features.

5) It is better to add global identifiers (to identify the processing side of a mask and a wafer), local identifiers (to identify a chip or a substructure from the devices), and testing structures (to check the lithography resolution and DRIE depth) on the mask. It’s important to make sure that all the marks are not removed during the process.

6) Mask writing with a laser beam is generally a high-cost process. There are a number of tricks to reduce exposure time for Heidelberg DWL66 mask maker (which is used in CMI at EPFL). Since the DWL scans much faster in the Y-direction than in the

X-direction, the structures should be designed in a way that the longest features (e.g. the long beams of suspensions) are in the Y-direction. Large areas of empty space should be avoided in the design as the system will take the same time to scan even if there is nothing to pattern. A write head that is appropriate for the resolution requirements should be used.

3.2 Microfabrication process



Figure 3.6: Schematic of the process flow (not to scale). (a) LPCVD SiO₂. (b) Topside lithography and RIE. (c) Backside lithography, RIE SiO₂ and DRIE. (d) Topside DRIE. (e) SiO₂ etching in HF vapor. (f) E-beam evaporation of Cr and Au on topside.

The devices were fabricated on a 4 inch (100) SOI wafer with a resistivity of 1-10 Ω·cm (boron doped), which consisted of a silicon support layer of 380 μm, 2 μm buried SiO₂ and 100 μm device layer. The main process flow is illustrated in [figure 3.6](#), where only two lithographic masks are required.

Before starting the micromachining process, optical masks were fabricated with DWL200. The graphical patterns in L-Edit were firstly exported into Caltech intermediate Format (CIF) (GDSII also works) and then transferred to .lic file, which was executable in DWL 2000. During the file transfer, the laser configuration was selected as a 10 mm lens with 4 beams mode (very high speed), which could achieve a writing resolution of 2.0 μm, and the estimated writing time for a 5 inch mask is 26 min. Note that the patterns on the optical mask are a mirroring with respect to the Y axis of the layout. The as-received blank mask was a 127 mm×127 mm quartz plate that was coated with a 100-nm-thick layer of low reflective Cr. On top of this Cr film, 530-nm-thick positive resist (AZ1518) was coated. After exposure by the laser beam, this

photoresist (PR) was developed and the exposed Cr is etched away in a wet bench (20 °C, chemical: $\text{HClO}_4 + \text{Ce}(\text{NH}_4)_2(\text{NO}_3)_6 + \text{H}_2\text{O}$, time: 110 s).

The as-received SOI wafer were firstly cleaned by a standard RCA cleaning before the deposition of a 1- μm -thick low temperature silicon oxide (LTO) layer by low pressure chemical vapor deposition (LPCVD) (400-450 °C, 6-9 nm/min). This SiO_2 layer can also be deposited by sputtering on both sides of the wafer, which is a faster process. Note that the laser marking is on the back side of a SOI wafer (i.e. on the handle layer).

A 3 μm -thick AZ92XX PR was coated on the topside of the wafer (Rite Track, 3450 rpm, 45 s, no EBR) after HMDS treatment, and was exposed with the first mask in MA150 (contact mode, exposure time: 15 s). Note that the Cr side on the mask was facing down during exposure. Then the PR was developed followed by a post bake (115 °C, 5 s). The exposed SiO_2 was etched by reactive ion etching (RIE) in AMS200 (selectivity of SiO_2 to PR is 1:1, 0.3 $\mu\text{m}/\text{min}$, 4 min). This process could be checked by measuring thickness of the remaining SiO_2 with Nanospec AFT-6100 spectro-reflectometer. The PR was stripped in O_2 plasma. The patterned SiO_2 on topside of the wafer served as hard mask for the subsequent DRIE.

A 5- μm -thick AZ9260 PR was spun onto the support layer of the wafer (EVG150, no EBR) after HMDS treatment. This PR was patterned by the second mask (exposure time: 21 s), which was aligned to the marks on topside of the wafer in MA150. The PR was developed in DV10. The exposed SiO_2 on the backside of the wafer was etched by RIE in AMS200 (4 min). Then the exposed Si was etched by DRIE (20 °C, 3-4.5 $\mu\text{m}/\text{min}$) until the buried SiO_2 layer. The “ending point” was determined by measuring the thickness of the backside cavity with an optical profiler (Veeco Wyko NT1100). Note that the large etching depth of the wafer (backside) cannot be measured by a profilometer (TENCOR–Alpha-Step 500) because the stylus cannot reach the bottom of the cavities.

With the patterned SiO_2 as a mask, the device layer was etched by DRIE in AMS200 until the buried SiO_2 to form comb fingers, capacitive plates, suspensions, gaps for bridging specimen, and the electrical insulation gaps. Note that the large openings (e.g. the suspension region) would be etched to the buried layer earlier than the small openings (e.g. the gaps between capacitive plates) due to the ARDE effect; some over-

etching time was needed. To avoid excessive long time of over-etching at the large opening while ensuring the small openings reaching the desired ending point, a Si dummy wafer that had the same pattern as the SOI wafer was etched by DRIE using the same recipe. The over-etching time for the SOI wafer was determined to be about 12 min. Furthermore, during the DRIE process, we have used a special recipe developed in Alcatel AMS 200 [ALCATEL web, www.alcatelmicromachining.com.] to avoid the electrical charging effect at the Si–SiO₂ interface.

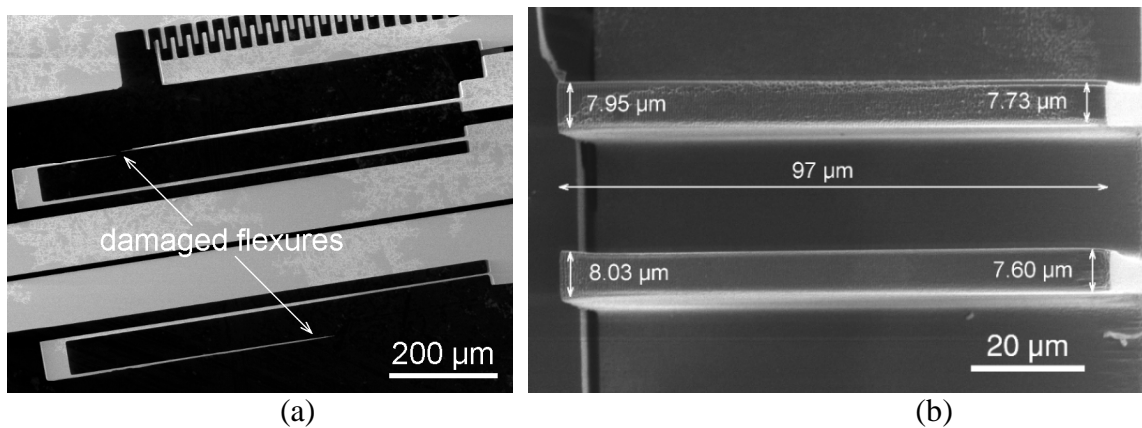


Figure 3.7: SEM images of (a) a silicon suspension damaged by thermal effects and (b) the finally fabricated comb fingers (sidewall).

At the last phase of the device layer DRIE, a helium leak was observed in the chamber of AMS200 since the exposed buried SiO₂ film could not withstand the helium gas (for cooling) at the backside of the wafer. Then a dummy Si wafer was temporarily bonded to the backside of the SOI wafer using heat conductive paste. This paste is afterwards removed using an acetone cleaning (scratch cleaning). By employing a silicon dummy wafer, the loading and the reactant concentration remain practically unaltered even if the buried SiO₂ is completely etched through [Sarajlic, 2006]. However, an enhanced lateral under-etching and ultimately a severe damage of the flexures had been observed, as shown in figure 3.7(a) in the 1st SOI wafer. Similar serious under-etching was previously reported in [Bertz et al., 2002; Sarajlic, 2006; Qu et al., 2007] and attributed to the thermal effect due to ions bombardment. This heating effect was not pronounced at the beginning stage of the DRIE, because heat could easily conduct away through the remaining silicon that prevented (local) excess temperature increase, as illustrated in

figure 3.8(a). However, when the microstructures are completely released, as shown in figure 3.8(b), the heat conducting path was decreased. This limited heat conduction dramatically increased the temperature of the suspensions causing the fluorocarbons passivation to fail and isotropic etching. Due to this heating effect (within a few minutes), many devices in the 1st SOI wafer were destroyed.

Several methods may be used to mitigate the heating effect. First, the over-etching time can be reduced by eliminating or suppressing the ARDE effect (e.g. by using a properly designed mask). Second, the etching process can be optimized by reducing the discharge power and by lowering the chuck temperature [Bertz et al., 2002]. Finally, temporarily connecting suspended structures to each other and/or to surrounding bulk material (e.g. by PR) to form additional thermal paths [Qu et al., 2007]. These conductive paths material must be easily removed after the etching is completed.

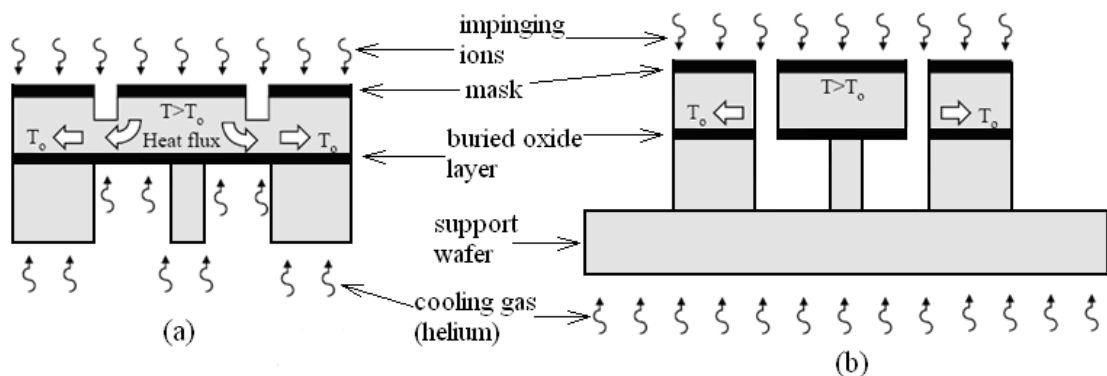


Figure 3.8: Schematic of the heat conduction in a SOI wafer during DRIE process (adapted from [Sarajlic, 2006]). (a) The SOI wafer could be well cooled by the backside helium gas when the device layer is not etched through. (b) The heat conduction path is significantly limited when the SOI wafer is etched through and placed onto a support wafer.

During the processing of the 2nd and 3rd SOI wafers, the wafers (SOI wafer bonded onto a Si support wafer) were taken out of the processing chamber of AMS200 every 1.5-2 min to avoid excess temperature increase in the suspended structures. Consequently, a yield of 80% was achieved. Figure 3.7(b) shows a SEM image of the fabricated comb fingers (the sidewall). Although the fingers (with a thickness of 100 μm) are thinned by up to 2.4 μm (the designed width is 10 μm), they have rather vertical

profiles with an average width difference of about 325 nm between the top and bottom sides, certifying that the notching effect has been efficiently mitigated.

It had been found that the adjacent parallel capacitive plates could stick to each other if wet etching was used to remove the SiO_2 (e.g. in HF or Silox solutions). Vapor-phase hydro-fluoric (HF) acid was finally used to remove the exposed SiO_2 layer. In the last step, the wafer topside was coated with Cr (10 nm) and Au (100 nm) films by E-beam evaporation. The gold layer on device surface served as contact for gold wire bonding, trace of the on-chip electrical measurements, and for reducing the sensor series resistance [Suster et al., 2006]. It is worth noting that the under-etching in the buried SiO_2 is larger than 600 nm during HF vapor etching, the insulation trench will not be covered by the deposited metal layer, and thus there is no short circuit.

3.3 Packaging

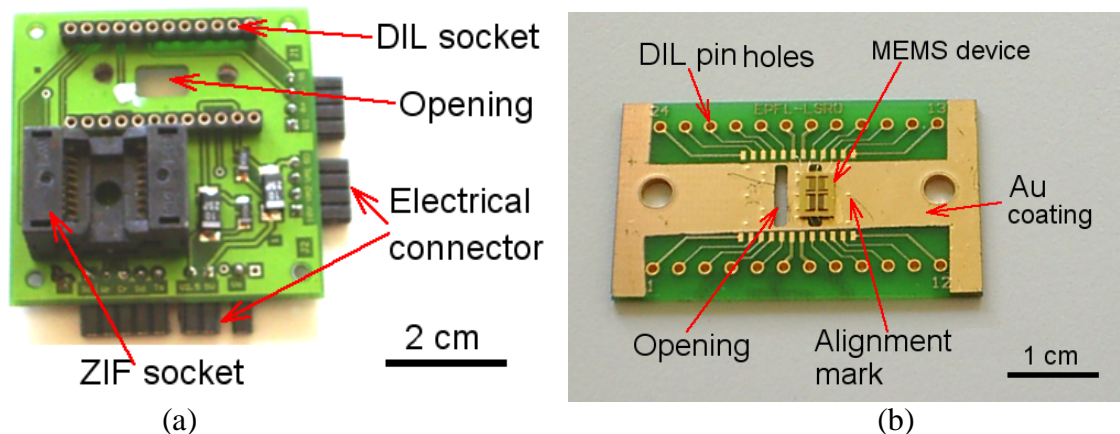


Figure 3.9: Packages for MEMS device. (a) The big PCB. (b) The small PCB.

Individual NWs have to be mounted on the MEMS device by *in-situ* nanomanipulation inside a SEM. Hence, the devices can not be packaged hermetically, which makes them extremely fragile. This drawback requires that the device should be easily changed after it is broken. Two printed circuit boards (PCB) are designed for the MEMS devices packaging, which are called big PCB and small PCB, as shown in figure 3.9(a) and (b) , respectively. A MEMS device is glued on the small PCB and wire bonded to the pads on it. The small PCB is designed in the form of dual-in-line (DIL) package, which can be easily changed once the housed device is broken. The big PCB is designed to mount the

small PCB with a plug-and-play socket with all electrical connections, and can be fixed onto a SEM stage. A Zero Insertion Force (ZIF) socket (16 pins, Digi-key, Thief River Falls, MN 56701, USA) was soldered on the big PCB, which can house the capacitive readout chip MS3110 (Irvine Sensors, Costa Mesa, CA, USA) inside a SEM chamber. During testing, the small and the big PCBs are mounted inside a SEM chamber. The electrical signals from the big PCB are connected to the outside through the electrical feed-through of the SEM. Figure 3.10 shows the schematic of the electrical connection of the setup, similar to that presented in [Zhu et al., 2005].

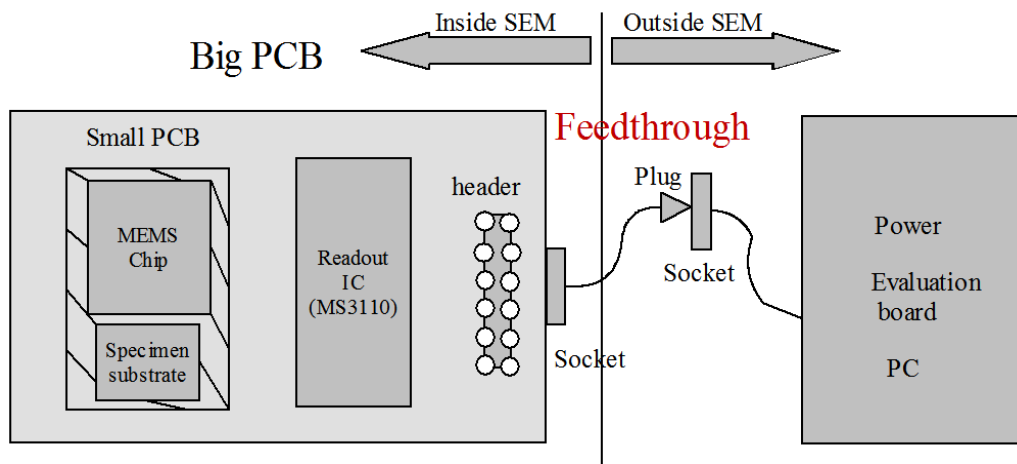


Figure 3.10: Schematic setup for *in-situ* SEM experiment.

For the MEMS device consisting of a comb-drive actuator and a capacitive sensor, capacitive sensing electronics has to be designed to convert the capacitance signal into analog voltage/current signal. We used a commercial capacitance readout chip MS3110, which can measure the differential capacitance signal with a typical resolution of $4 \text{ aF Hz}^{-1/2}$ ($1 \text{ aF} = 10^{-18} \text{ F}$). Since MS3110 is based on a sensing scheme of opposite excitation with a capacitive feedback, the large parasitic capacitance that is parallel connected to the capacitive sensor can be effectively mitigated [Bao, 2005]. With the ZIF socket, MS3110 could be placed inside SEM chamber. However, for *in-situ* TEM studies, MS3110 has to be placed outside of the chamber. In this case, short and shielded coaxial cables should be used to suppress the influence of the surrounding electromagnetic field and the parasitic capacitance from the conducting wires.

It should be noted that all the material used inside a SEM should be vacuum compatible. The custom-made PCB proved no problem even in the high resolution SEM (Cold field emission, Hitachi, S4800) with a very low pressure ($\sim 10^{-6}$ mbar). To avoid electrical charging on the small PCB during e-beam imaging, its surface is coated with 50 nm Au with Al foil as masks. A small opening beneath the movable shuttle of the comb drives and the force sensors was designed in the small PCB to allow the free movement of the MEMS device. This opening is also indispensable for the tensile testing in TEM, since the transmission electrons will be detected by a detector beneath the device.

To glue an MEMS device on the small PCB, extremely carefulness has to be taken to prevent destroying the devices. First, an individual device is released from a wafer. A sharp metal wire (diameter ~ 50 μm) was used to dip a very small drop of non-conductive adhesive (Epsilon 2103, Abattech, La Chaux-de-Fond, Switzerland) and transferred a small volume of this glue to the backside of the MEMS device. Sharp tweezers with plastic end effector was used to pick up the MEMS device and put it on the small PCB. Several metal points were designed on the small PCB for aligning the MEMS device. The small PCB was baked in an oven at 90 °C for about 2 h for the paste curling. Note that the MEMS device could be dragged up during the wire bonding if it was not glued stiffly on the PCB. The in-plane stiffness of the actuator and force sensor was calibrated using a resonance method (see [Chapter 4](#)) inside a SEM, followed by soldering the dual-in-line pins onto the small PCB.

3.4 Summary

Nanotensile stages were fabricated in a SOI wafer by an optimized DRIE based process. Several important issues in the layout design were presented, such as the crystal orientation of suspensions, supporting hinges for dice-free releasing of individual devices, adjacent tips for increasing measurement resolution, and uniform openings to suppress ARDE and notching effects. Special cares have to be taken in the DRIE process to suppress the notching and thermal effects that could damage the slender flexible beams. The fabricated MEMS devices were packaged in a dual-in-line form to enable easy exchange after it was broken on customer-made PCBs.

This page intentionally left blank

4.

Device characterization

In this chapter, characterization results of the developed nanotensile stages are presented. Since the devices are designed for *in-situ* tests, the calibration experiments were done inside a SEM under vacuum condition. The main characterization work consists of stiffness calibration of the actuator and force sensor, voltage-displacement characteristic of the actuator, capacitance-displacement characteristic of the capacitive sensor, and noise analysis and pull-in voltage prediction of the capacitive sensor.

4.1 Stiffness calibration

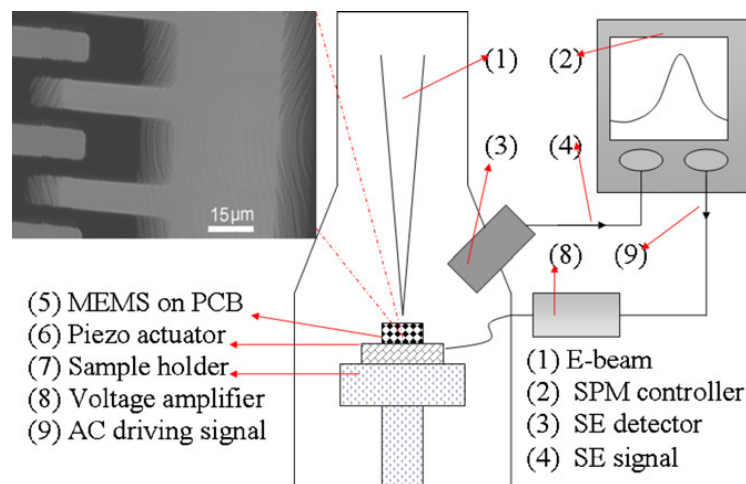


Figure 4.1: Schematic of experimental setup for in-plane stiffness calibration. Inset: SEM image of resonance vibration of comb fingers.

The force measurements for both types of force sensors (capacitive sensor and clamped-clamped beam) are based on Hooke's law. Thus, accurate calibration of the flexures' stiffness is crucial. A resonance method was used to calibrate the in-plane stiffness of the actuators and sensors. The vibration of a comb-drive actuator can be excited by applying an ac drive signal. However, the triplate capacitive sensor and clamped-clamped beams cannot be excited in this way. Shear mode piezoelectric ceramics (C82, Fuji Ceramics)

were used to mechanically excite vibrations in the testing system. The schematic experimental setup is shown in [figure 4.1](#). The fabricated devices were first glued on a custom-made PCB and wired bonded to the pads on the PCB. Then the PCB is fixed onto the piezo ceramics. The measurements were performed inside a SEM (Hitachi S-3600N). Before vibration, the electron beam was focused at the edge of a movable structure. The ac drive voltage applied to the ceramic bar was controlled by a NANONIS SPM controller (Nanonis GmbH, Switzerland). During sweeping the drive frequency, the secondary electron (SE) current was modulated by the in-plane movement of the MEMS device [[Gilles et al., 2008](#)] and can be detected by the SPM controller. The peak signal of the SE current corresponded to the resonance of the MEMS device. Note that all the electrodes of the actuator and capacitive sensor had to be connected to avoid electron charging during imaging, which could induce error for the stiffness measurement or even snap the parallel plates together. As the damping in the device is small, the measured first resonance frequency can be approximated by the natural frequency. The relationship between the first resonance frequency f_0 and stiffness K_0 can be expressed as

$$K_0 = (2\pi f_0)^2 M_{\text{eff}}, \quad (4.1)$$

where $M_{\text{eff}} = M_s + M_t/4 + 12M_b/35$ for folded flexures [[Tang, 1990](#)] and $M_{\text{eff}} = M_s + 13M_b/35$ for clamped-clamped beams (please refer to [Appendix A](#) for the derivation) from Rayleigh's energy method [[Weaver et al., 1990](#)], M_s , M_t and M_b are the total masses of the shuttle, the trusses, and the suspended beams, respectively (see [figure 2.8](#)), which are calculated from their geometries measured from SEM images. The vibration amplitude is kept low (≤ 3 % of the flexures' length) to avoid nonlinearity in the suspensions.

From the measured 1st resonance frequency, the representative values of sensors and actuators stiffness are calculated and listed in [table 4.1](#), which agree with the calculated stiffness based on the measured beam dimensions. Note that the devices' stiffness may vary a lot from wafer to wafer due to the different DRIE time, thus each of the devices has to be carefully calibrated before usage. Experience has shown that when a voltage amplifier is connected to comb drives, the comb drives may not be driven into resonance vibration when the drive frequency (i.e. the AC signal of the amplifier) is half of the

natural frequency of a comb drive. This is because that the large capacitance of comb drives could significantly influence the behavior of the amplifier, e.g. the slew rate and bandwidth [Falco Systems, http://www.falco-systems.com/high_voltage_amplifiers.html]. Therefore, special care has to be taken when using voltage amplifiers to determine the resonance frequency of comb drives.

Table 4.1: Calibrated sensor and actuator stiffness.

Device number	Measured resonance frequency (Hz)		Stiffness (N/m) calculated from equation 4.1		Stiffness (N/m) calculated from beam dimensions	
	Sensor	Actuator	Sensor	Actuator	Sensor	Actuator
#1	1329	1404	33.23	35.47	32.62	34.90
#2	859	1035	13.84	13.84	13.92	13.92
#3	4911	697	16.02	16.88	17.25	14.34
#4	4122	1262	18.26	20.61	15.20	20.88

Note: Devices #1 (with 240 pairs of comb fingers) and #2 (with 160 pairs of comb fingers) are composed of a comb drive actuator and a capacitive sensor. Devices #3 (with 240 pairs of comb fingers) and #4 (with 160 pairs of comb fingers) are composed of a comb drive actuator and a clamped-clamped beam force sensor.

4.2 Voltage-displacement characteristic of actuator

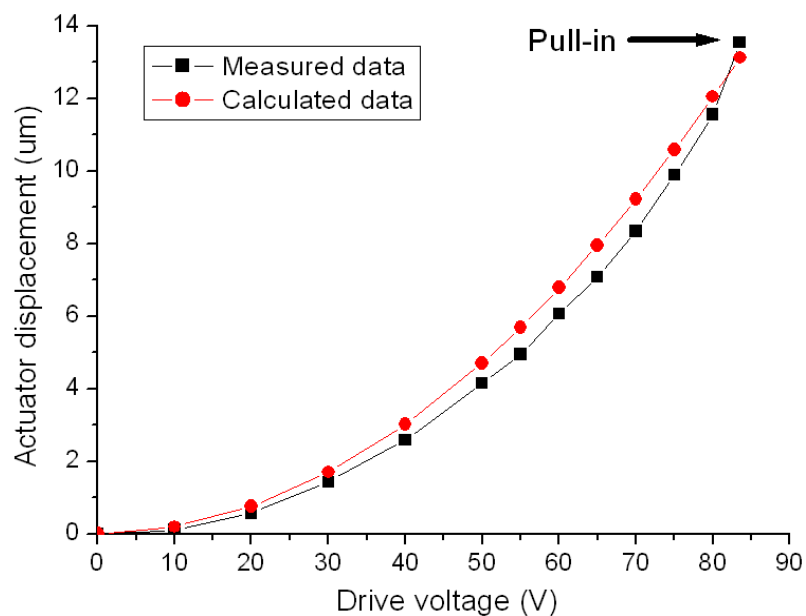
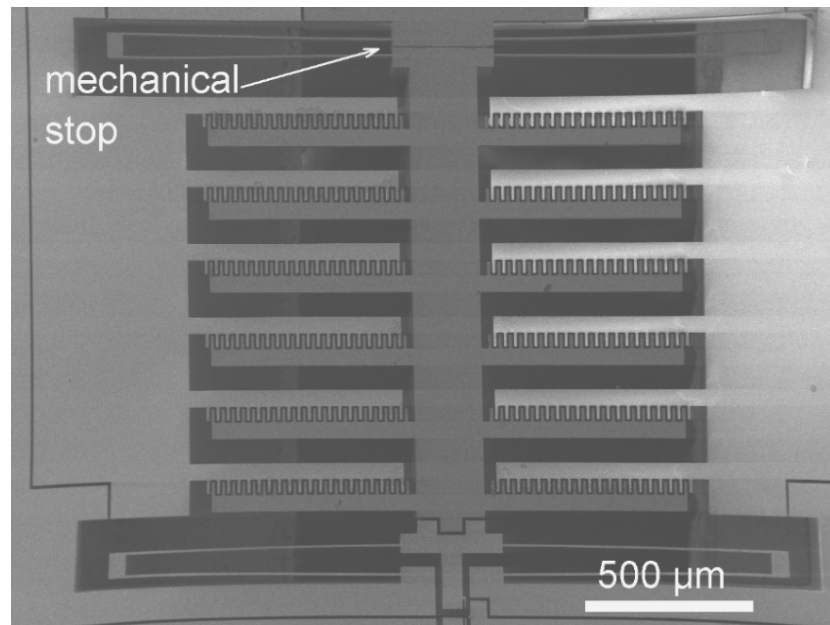


Figure 4.2: Drive voltage versus actuator displacement (device #3).

The geometry of the comb-drive actuator was optimized by FEA in [Section 2.2](#) to shrink their size while enable a voltage-controlled force output. To check the performance of the fabricated comb drives, actuator displacements under various drive voltages were measured from SEM images and plotted in [figure 4.2](#). The analytical results are also shown in [figure 4.2](#) for comparison, which are calculated from $x = n\epsilon_0 h V^2 (gK_A)^{-1}$ (it is derived from [equation 2.24b](#)) with the measured sizes of comb fingers ($g = 6.55 \mu\text{m}$, $h = 100 \mu\text{m}$) and calibrated flexure stiffness ($K_A = 16.88 \text{ N/m}$). It can be seen that the measured data agrees well with the analytical results in the voltage range of 0 to 70 V, which confirms the accuracy of the stiffness calibration. The small deviation could be attributed to the non-perfect vertical profile of the comb fingers. When the drive voltage is larger than 75 V, the measured displacement increases faster and the deviation between the measured and calculated results becomes smaller. This is because that the movable fingers are close to the fixed fingers at high drive voltages and thus the fringing electrical field plays an important role, which was neglected in the analytical calculation. The front pull-in, as shown in [figure 4.3](#), was observed at a drive voltage of 83.5 V.



[Figure 4.3](#): SEM image of a comb-drive actuator at front pull-in.

As analyzed in Section 2.4, the front pull-in conditions can be computed from equations 2.26. With the measured values of $g = 6.55 \mu\text{m}$, $L_0 = 40 \mu\text{m}$, $L_1 = 15 \mu\text{m}$, $K_A = 16.88 \text{ N/m}$ (assuming $h = 100 \mu\text{m}$), the pull-in voltage is computed to be 79.04 V (the corresponding pull-in displacement is 16.3 μm), which agrees well with the experimental value of 83.5 V (the measured pull-in displacement is about 13.5 μm). Note that the above experimental results and analysis are made only for the actuator. During nanotensile testing, a specimen resides on the device and the force sensor is connected to the actuator through the specimen. Thus, the front pull-in conditions will change. Assuming that the specimen (1D nanostructure) have an infinite stiffness and the sensor stiffness is $K_0 = 17 \text{ N/m}$, the front pull-in voltage is estimated to be about 118 V.

4.3 Displacement-capacitance characteristic of capacitive sensor

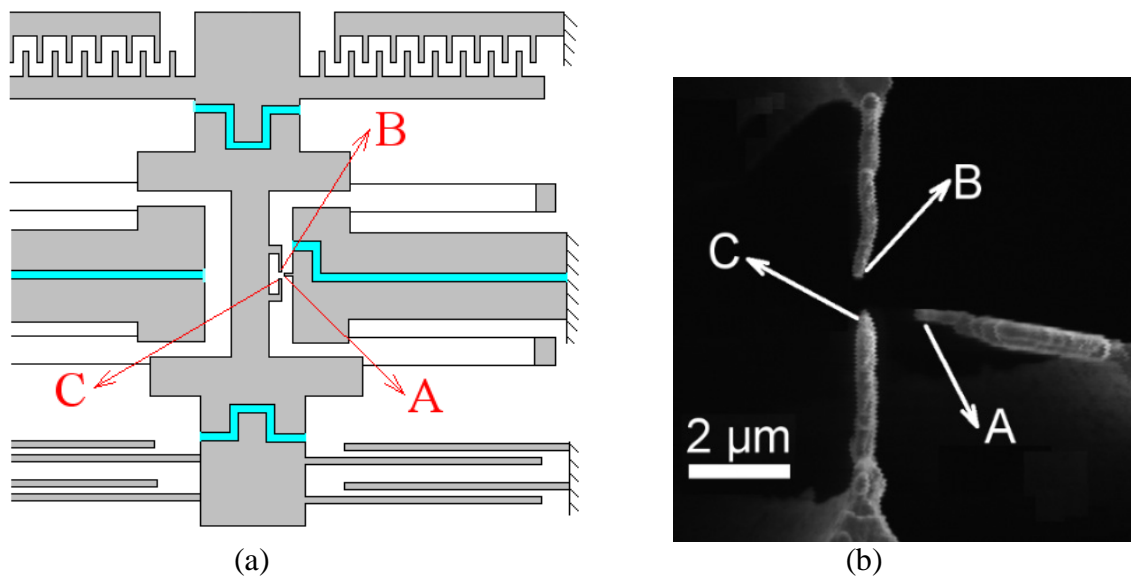


Figure 4.4: (a) Schematic of three-beam structure for high resolution displacement measurement. (b) SEM image of FIBID of copper-carbon beams.

The sensitivity of a capacitive sensor depends on its architecture and also the interface electronics. A Universal Capacitive Readout™ chip MS3110 (Irvine Sensors, Costa Mesa, CA, USA) was used to convert the differential capacitance change into voltage change. MS3110 is based on a sensing scheme of opposite excitation with a capacitive

feedback. The feedback capacitor (C_F) and the gain (GAIN) of MS3110 were selected so that it had a sensitivity of 0.934 mv/fF, which was calibrated by its internal capacitors.

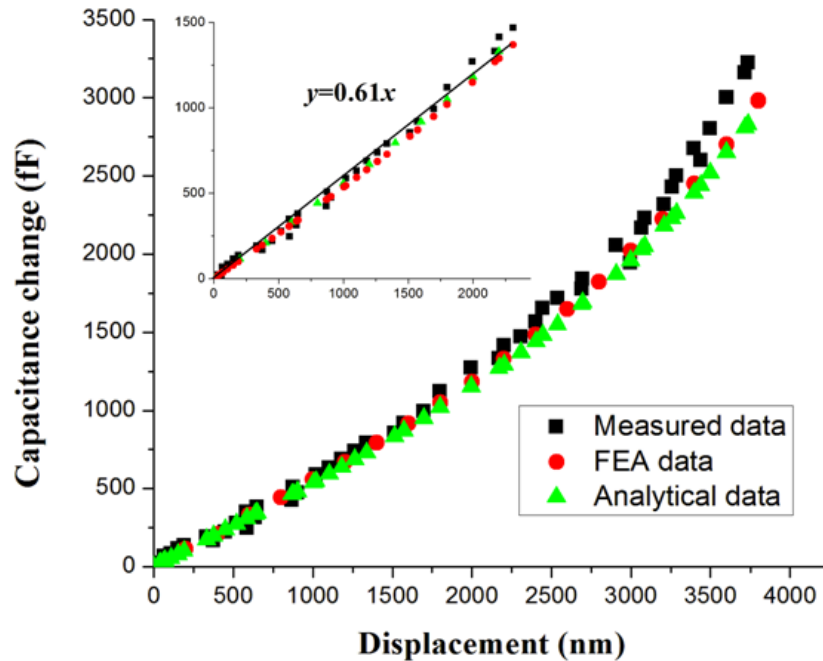


Figure 4.5: Measured capacitance change versus displacement. Inset: Linear fit of measured data from 0 to 2250 nm, i.e. the quasi-linear working range.

The small displacement in the capacitive sensor was introduced by small stepwise increases of the drive voltage of the actuator where a MEMS device without a gap between the actuator and the sensor was used. The sensor displacement was measured from a series of SEM images that were taken at high magnification. It was found that the stepwise increased DC driving voltage could induce drift of the e-beam (up to ~ 700 nm at drive voltage of 120 V). To accurately measure the sensor displacement, a special “three-beam” structure was fabricated by FIBID of copper as shown in the inset of figure 4.4(a) and (b). The beams A, B and C were mechanically connected to the fixed part of the device, the actuator and the force sensor, respectively. Beam A was not movable in the device frame, but will be shifted in the image frame due to the drift of the e-beam. The gap change between A and C corresponds to the sensor’s displacement. Since the initial gap between A and C can be controlled by FIBID with nanometer resolution, a displacement resolution better than 10 nm have been achieved and therefore the

accuracy of the capacitance calibration is improved significantly. The sensor displacement was recorded in a series of SEM images and the output voltage of MS3110 was recorded simultaneously through a 6 1/2-digit multimeter Keithley model 196. During the capacitance calibration, MS3110 was placed outside SEM chamber and connected to the MEMS device through the electrical feedthroughs of the SEM with shielded cables.

The measured capacitance change versus displacement is plotted in [figure 4.5](#). The sensitivity of the capacitive sensor within a working range of 2250 nm is determined to be 0.61 fF/nm, equivalent to 0.57 mV/nm according to the settings of the readout electronics used in the experiment. Note that the sensitivity value in the unit of mV/nm can be programmed on the MS3110 (by choosing different values of C_F and GAIN). The other sensitivity value (in the unit of fF/nm) is used in the following for performance comparison. The FEA result and the analytical values (according to [equation 2.13](#)) of the capacitance change versus displacement are also plotted in [figure 4.5](#). In the analytical prediction and the FEA, sensor geometry measured from SEM images was used as input. For the FEA, COMSOL Multiphysics was used to calculate the capacitance for a 3D model of one sensor unit. There are three types of boundary conditions in the electrostatic model: zero charge/symmetry boundary condition on the bounding box, fixed electrical potential V_f on the movable capacitive plates, and the ground boundary condition on the fixed capacitive plates. The 3D model was partitioned into tetrahedral elements with a predefined mesh size of “extra fine” and more than 211081 elements were generated (the number of elements is increased as the sensor moves in the model). The capacitance C_1 (or C_2) of the fixed capacitive plates was calculated with $C_1 = Q_1 / V_f$ ($C_2 = Q_2 / V_f$), where Q_1 (Q_2) was the surface charge on that sensing electrodes obtained from boundary integration of the surface charge density. The total capacitance change ΔC of the fabricated sensor was obtained by multiplying the value of $C_2 - C_1$ with the number of the sensor units. MATLAB was used to program changes in the model, i.e. the gap changes between the movable and the fixed sensing electrodes, by adding “for” loops and arrays around the code created by COMSOL, which allows for faster data capturing without constructing the models every time. In the FEA model, the fringing

field was taken into account in the capacitance calculation, which was neglected in the analytical modeling (see [Section 2.3.2](#)). The good agreement between the FEA and the analytical data shown in [figure 4.5](#) verifies that the designed sensor can be approximated as multiple parallel-plate capacitors without considering the fringing field. The measured data agrees very well with both the analytical and the FEA results within a displacement of 2250 nm. When the sensor displacement is larger than 2250 nm, the linearity decreases somewhat and the discrepancy increases. The deviation at large displacement is likely due to the vibrations of the movable plates. It was found that the sensor output becomes unstable when the displacement was larger than 4 μm because of large vibrations of the movable plates, which was observed from SEM images. The capacitive sensor shows a high linearity, with R^2 (coefficient of determination) value of 0.99 by least-squares linear regression of the measured data in the range of 0 to 2250 nm.

4.4 Noise analysis for capacitive sensor

The noise level determines the minimum detectable signal in the measurement (suppose the sensitivity is fixed), i.e. the resolution. Various noise sources in MEMS capacitive sensor system have been discussed in [[Gabrielson, 1993](#); [Spencer et al., 1988](#); [Wu et al., 2004](#); [Suster et al., 2006](#)]. Assuming that the upper limit of the bandwidth interested f_2 , is well below the sensor's mechanical resonance frequency f_0 , the total noise power in the MEMS sensor (exclude the interface electronics) for a bandwidth from f_1 to f_2 can be approximately described by

$$V_{noise}^2 = 4K_B T R_e (f_2 - f_1) + 2K_B T (f_2 - f_1) (\pi f_0 k_0 Q_m)^{-1} + \lambda \ln(f_2 / f_1), \quad (4.2)$$

where K_B is the Boltzmann constant, T the temperature in Kelvin, R_e the resistance seen by the sensor capacitance determined by the electrical network, Q_m the quality factor, λ the noise coefficient determined by the bias voltage and process parameters. The first term is the Johnson noise that is caused by the scattering of free electrons inside the structure [[Nyquist, 1928](#)], and the second terms is the Brownian noise that results from the thermal energy transferred from the surrounding mediums [[Gabrielson, 1993](#)]. In high vacuum environment (e.g. *in-situ* testing inside SEM/TEM), Brownian noise is minimized and can be neglected since it is small compared to Johnson noise. The third

term is flicker (or 1/f) noise that is believed to be frequency dependent [Hooge, 1969]; however the generation mechanism is complicated and still uncertain. Since the developed on-chip testing stages are intended for applications inside SEM/TEM, it is worth considering the possibilities of noise coming from the microscopes. First, the electrons in the primary beam have energy in the kilo electron volts range. The e-beam bombardment generates considerable heat, which can increase the Johnson and Brownian noises in the sensor. A good thermal conduction between the MEMS sensor and the SEM/TEM stage is necessary to minimize these noises. Second, the electrons from the primary beam enter the sample and interact with the atom lattices through scattering mechanisms. The emitted electrons (i.e. secondary and back scattered electrons) from the sample (metal and semiconductor) are generally less than the injected electrons [Thong, 1993], thus some surplus electrons remain in the sample. Assuming there is no internal electrical field (e.g. due to the presence of a P-N junction) within the sample, a current (called sample current or absorption current) that is in the range of picoampere can be measured by connecting it to the ground through a high sensitive current meter. On one hand, the surplus carriers will probably reduce the 1/f noise in the MEMS sensor, since the 1/f noise is found to be inversely proportional to the total number of the free carriers within a resistor [Hooge, 1969]. On the other hand, the surplus carriers can flow into the interface electronics and possibly cause signal fluctuation. Additionally, the absorption current can be significantly enhanced (by three orders of magnitude) for a semiconductor with an internal/external electrical field due to the electron beam induced current (EBIC) effect [Leamy, 1982]. In this case the electrical measurements are more susceptible to the e-beam. To avoid the EBIC effect, the primary beam should not be incident on the sensor region. Other solutions to minimize this effect include operating the SEM/TEM at a low acceleration voltage and coating the device surface with a metal layer of certain thickness to protect the semiconductor from the impinged electrons. The penetration depth of high energy electrons into various solid specimens can be estimated by Monte Carlo simulations [Ryuichi et al., 1992].

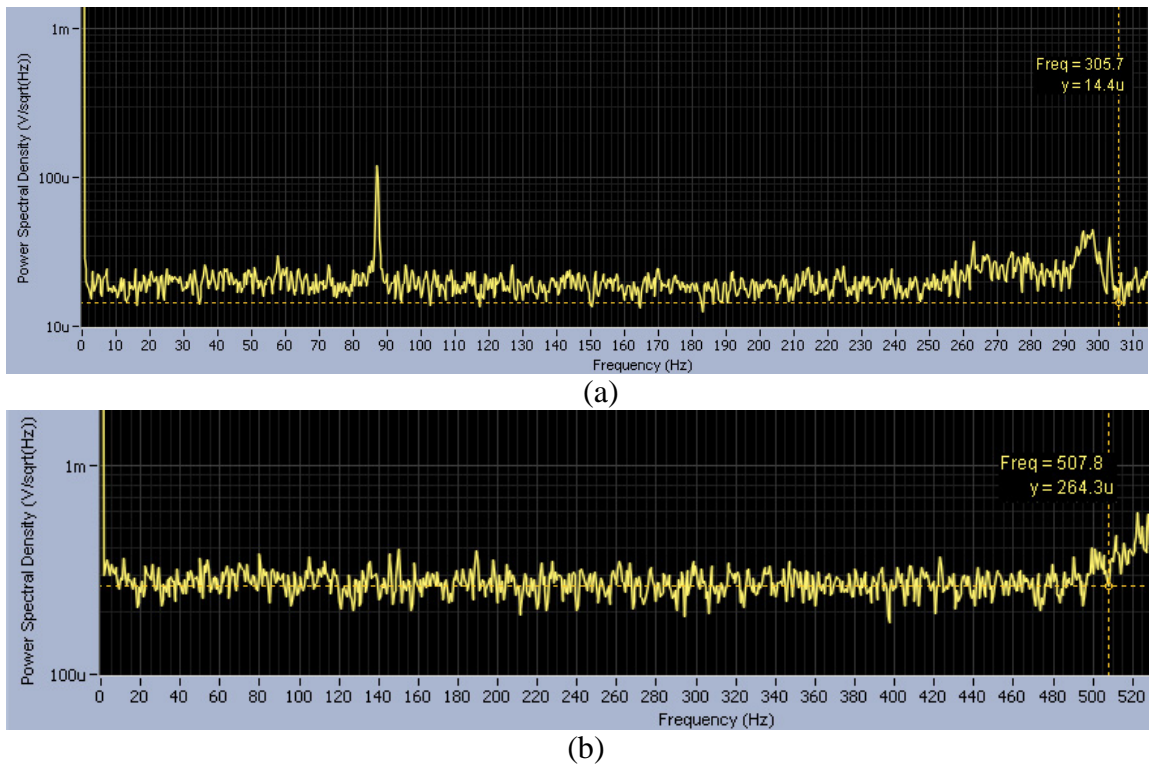


Figure 4.6: Measured noise spectrums of the capacitance measurement system. (a) All the connecting cables (inside and outside of SEM chamber) are shielded. (b) The connecting cables outside of SEM chamber are shielded, but the inside cables are not shielded. Note: the unit of the data shown in the vertical axis is V/\sqrt{Hz} .

The output voltage noise power spectral density of the complete measuring system was measured using a spectrum analyzer (Nanonis GmbH, Switzerland). A noise floor of $17 \mu V Hz^{-1/2}$ was measured except in the frequency range of 86 ± 2 and 280 ± 20 Hz, as shown in [figure 4.6\(a\)](#). Deterministic peak voltage noise power densities of about 140 and $50 \mu V Hz^{-1/2}$ are observed at 86 and 295 Hz, respectively. The reasons of these peak signals are not clear at this moment. The total noise voltage is estimated to be about 0.56 mV for a bandwidth between 0 and 300 Hz, which results in a displacement resolution of 1 nm according to the measured sensitivity of 0.57 mV/nm. The corresponding force resolution is computed to be 34 nN with the measured flexure stiffness of 33.23 N/m (device#1). The above experimental values of the sensitivity and the noise floor are measured when the e-beam is on (with 10 KV acceleration voltage) and impinged at the “three-beam structure” (which is electrically insulated from the sensor). To check the influence of the e-beam on the sensor operation, the e-beam was shifted to the movable

and fixed sensing electrodes of the capacitive sensor, respectively, and focused the e-beam there with different magnifications. In each case, the sensor output and the noise spectrum were recorded and compared. No measurable changes were found either at the sensor output or at the display output of the spectrum analyzer. It can be concluded that the e-beam of the SEM has negligible influence on the capacitance measurement in the experiments. A further reduced electronic noise floor is expected by placing the MS3110 on the same PCB as the MEMS sensor inside SEM to further minimize the parasitic capacitance and the electromagnetic interference. Note that the shielding of conducting wires has a significant influence to the measured noise spectrum. When the connecting cables inside the SEM chamber were not shielded, a large increase of the noise signal had been observed as shown in [figure 4.6\(b\)](#). The achieved performance of the capacitive sensor in this work is comparable to that presented in [[Espinosa et al., 2007](#)] (sensitivity: 0.05 fF/nm, load resolution: 12 nN and displacement resolution: 1 nm), which shows the promise of the developed devices for nanomechanical testing.

4.5 Pull-in voltage of capacitive sensor

At given sensor stiffness K_0 , the capacitive sensor's pull-in voltage V_{PI} can be determined from [equation 2.18](#) with the following formula

$$V_{PI} = \left(\frac{K_0}{2N\epsilon_0 A} \frac{d_1^3 d_2^3}{d_1^3 + d_2^3} \right)^{1/2}. \quad (4.3)$$

The sensor geometry was measured from SEM images. With the measured stiffness 33.23 N/m, the pull-in voltage is computed to be 19.87 V.

The fixed electrodes, C_1 and C_2 , were connected together and a DC voltage was applied between C_2 and the movable electrode C_0 (see [figure 2.9](#)). By increasing the bias voltage gently step by step, the pull-in voltage was determined when the movable plates suddenly collapsed into the fixed plates. The measured pull-in voltage is 16.68 V, which is somewhat lower than the calculated value. We think the measured smaller value is due to the dynamic pull-in that is introduced from the gradually increased bias voltage. [Equation 4.3](#) is deduced under quasi-static assumptions. It has been shown that the pull-in voltage under dynamic conditions can be lower than the quasi-static pull-in voltage [[Nielson et al., 2006](#)].

4.6 Summary

The device performances were completely characterized. The in-plane stiffness of the fabricated actuators and force sensors was calibrated inside a SEM chamber by a resonance method. The measured sensor stiffness ranges from 13 to 33 N/m. The measured voltage versus displacement of the comb drives agrees well with the analytical results when the drive voltage is smaller than 80 V. The front pull-in voltage and pull-in displacement of the actuator were measured to be 83.5 V and 13.5 μm , respectively. Capacitance versus displacement of the differential capacitive sensor was measured by using a commercial capacitive readout chip MS3110, which agrees very well with analytical and FEA results. Finally, a slightly lower pull-in voltage of the capacitive sensor than the analytical value was measured, which could be attributed to the dynamic pull-in effect.

5.

***In-situ* nanotensile and electrical measurements**

In-situ SEM nanomanipulation, well-known as low throughput and time-consuming, is a common technique to prepare samples for nanotensile testing. The main challenges in this task are discussed firstly, and a novel strategy of modifying device topography is proposed to facilitate pick-and-place nanomanipulation with higher efficiency. After a nanowire (NW) is placed on the MEMS device, its two ends need to be fixed onto the device by FEBID. This process (which is called nanowelding in the remainder of this thesis) has been found to introduce contaminants in the NW, which is quantitatively characterized using a HRSEM. The mechanical testing capability of the developed tensile stages are successfully demonstrated by testing three types of NWs inside a SEM, namely, Si <111>, Si <100>, and nanocrystalline Co NWs. However, the envisioned on-chip electromechanical measurements are not successfully conducted. The main reasons and difficulties in this work are discussed.

5.1 *In-situ* nanomanipulation

In tensile tests, an individual NW has to be aligned and fixed onto the MEMS device so that the tensile force is along its longitudinal direction. This requirement renders significant challenges for testing at the nanoscale due to the extremely small specimen size. Various techniques have been reported to align 1D nanostructures on a substrate, such as external field alignment [Smith et al., 2000; Huang et al., 2001; Fujiwara et al., 2001; Lu et al., 2005], direct growth of 1D nanostructures with controlled direction [He et al., 2006; Kiuchi et al., 2007], and pick-and-place operation [Williams et al., 2002; Fukuda et al., 2003; Zhu et al., 2005]. Compared with pick-and-place nanomanipulation, the former two methods are faster, simpler, and scalable to large production quantities. However, they are not as suitable for the developed tensile stages in this thesis due to the

following reasons: (1) the fabricated MEMS devices have many deep trenches serving as electrical insulation gaps, which can be easily short-circuited if conductive material is deposited inside these trenches. In addition, parallel capacitive plates can stick to each other in solvent due to the capillary force, which could not recover after drying. Therefore, electrophoresis alignment cannot be executed for our MEMS devices; (2) one could integrate the NWs synthesis into microfabrication of the testing stages as in [He et al., 2006] and [Han et al., 2006] or deposit an individual NW on the device [Kiuchi et al., 2007] directly, but then the devices can only be used once and the chemical composition and microstructure of these NWs are strictly limited.

Pick-and-place individual NWs with a nanomanipulator inside a SEM combined with nanowelding were used in [Zhu et al., 2005] and [Samuel et al., 2007] to mount single NWs onto a MEMS device, which is also adopted in this work. This technique is straightforward, but quite time-consuming and of low throughput that remains a main limitation in performing standard tensile tests on individual nanostructures. A specimen preparation technique that can achieve high efficiency and throughput is highly desirable.

5.1.1 Challenges of *in-situ* nanomanipulation

In-situ nanomanipulation relies on high magnification SEM images as a visual feedback system in order to interact with a nanoscale target using a probe, which has been extensively utilized to characterize the mechanical and electrical properties of novel nanostructures [Zhou et al., 2007]. The challenges of *in-situ* nanomanipulation arise from the specimen separation, imaging system of a SEM, moving freedom and resolution of a nanomanipulator, and the contacting force control during pick and release.

A. Specimen separation

NWs are normally synthesized in form of clusters, bundles or nets on the sample substrate, which need to be separated for easily picking up. Several methods can be used to separate NWs, such as casting a small drop of dispersed NWs solvent on the edge of a razor blade or TEM grid, or scratching the sample substrate with a razor blade or TEM grid. Special attention has to be paid in these operations to avoid introducing large defects in the NWs. To bridge an individual NW on the MEMS device, the specimen

length has to be larger than the gap in the MEMS device. In addition, a template substrate (where the NWs were temporarily residing) with a grid structure is helpful to reduce the contacting force between the NWs and the substrate [Li et al., 2007].

B. Imaging system of a SEM

A conventional SEM has a two-dimensional (2D) imaging system, i.e. the SEM image is a projection view of an object from the top. Therefore, a sample that looks parallel to a horizontal substrate from the SEM image might have a large tilted angle in the side view. In frequent cases, a NW picked by a manipulator tip is not parallel to the MEMS device. Hence, the two ends of the NW will not touch the device at the same time. After fixing one end of the NW onto the device by FEBID, this NW can possibly be released from the manipulator tip by retracting it. Then the other end of the NW is tilted with respect to the device surface. It is possible to push this end and make it contacting with the device with a manipulator tip, but a large bending stress in the sample will be introduced that could result in artificial defects or even failure (in particular for brittle NWs).

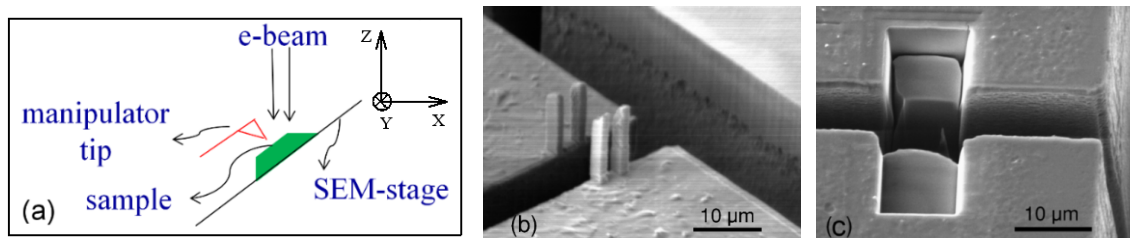


Figure 5.1: (a) Schematic of a tilted manipulation setup. (b) SEM image pillars fabricated by FEBID of copper-carbon composite. (c) SEM image of trenches fabricated by FIB milling.

SEM has a large depth of focus ranging from a few micrometers to several tens of micrometers, which is normally referred to as an advantage when compared with an optical microscopy since it allows imaging features of high topography differences. However, this tends to be a problem when we approach a manipulator tip toward a target (e.g. a MEMS device or an individual NW) in the Z-direction. The depth of focus depends on the working distance (WD), magnification, and aperture [Goldstein et al., 2007] of the SEM. A smaller depth of focus could be achieved when the SEM is working at a small WD, a large magnification, and with a small aperture.

To overcome the above two limitations, one could tilt the whole manipulation setup, as schematically shown in [figure 5.1\(a\)](#). In this case, the SEM stage (i.e. MEMS device) is not allowed to rotate with large angles with respect to the manipulator tip (to align the specimen). Another potential challenge here is the nonorthogonal movement of the manipulator tip with respect to the MEMS device, where the Z-direction position of the tip has to be compensated during its in-plane movement (in the X- and Y-directions) to avoid a crash into the device. With a dual beam SEM/FIB, one could obtain a side view of the setup with respect to the SEM image from the FIB image. However, the focused ion beam can easily introduce defects into the NWs, so this manipulation strategy is not considered here.

The modification of device topography is found to be quite helpful in that it is independent of the manipulation setup. This can be realized by pillars or trenches fabricated at the edge of the gap where the nanostructures will be bridged, as shown in [figure 5.1\(b\)](#) and [\(c\)](#). In the nanomanipulation strategies proposed in [[Williams et al., 2002](#)] and [[Zhu et al., 2005](#)], the NWs have to be soldered at the exact end of the manipulator tip otherwise they will not touch the device substrate on lowering the tip. However, this is not as critical with the help of trenches or pillars because the picked NWs can be released onto the sidewalls of the pillars and trenches. This function can be called a “release structure”. To make sure there is no height misalignment, both ends of the NWs (outside of the gauge length) have to be pushed toward the device substrate until they are in contact with the substrate. In addition, by approaching the NWs to the sidewall of the pillars or trenches, we are able to roughly estimate the distance between the tip and device substrate in Z-direction (this is difficult to be done alternatively due to the large depth of focus of a SEM). This function can be called as a “height reference”. When the NWs are placed inside the trenches or between the two sets of pillars, they have less chance to jump away (e.g. due to a slight crash) if they touch the device, which is a major cause for a failed manipulation. This function can be called as a “guard”. There is a caution that should be noted considering the low bending stiffness of these pillars. The bending of these pillars has to be excluded when measuring the specimen elongation.

C. Moving freedom and resolution of a nanomanipulator

For *in-situ* nanomanipulation, a large moving range (>2 cm) and a high resolution (sub-nanometer) are both required features of a manipulator. The large moving range is for transferring a single NW from the sample substrate to the MEMS device, and a very small step movement is for approaching the manipulator tip to the sample substrate or the MEMS device. A slip-stick piezo actuator equipped with a sharp tungsten tip (made by electrochemical etching) is used in this work. Note that the outer surface of the piezo actuator should be grounded to shield its electric field, otherwise the e-beam may be drifted or distorted. Compared with a conventional AFM tip, the tungsten tip allows for larger field of view, and is of low cost. The disadvantage of a tungsten tip is that it is susceptible to vibration during manipulation due to its low resonance frequency. To mitigate the vibration, the tungsten tip has to be kept short (<10 mm) and a thick support wire is desirable. Special care has to be taken to avoid crashing during manipulation, which can easily destroy the MEMS devices due to their high fragility.

A specimen has to be mounted on the MEMS device in such a way that the tensile force is along its longitudinal direction. This can be realized by rotating the MEMS device with respect to the manipulator tip before approaching the tip to the device. In our tests, a manipulator tip (attached with a NW) is typically kept about 5-6 mm over the MEMS device. This rotation freedom could be implemented by using the SEM stage.

D. Contacting force control

At the nanoscale, gravity force is negligible while other surface-based forces like electrostatic force, capillary force and van der Waals force play an important role. The most important issue in pick-and-place is how to achieve the control of the interaction forces [Fukuda et al., 2003] between the tool and sample, $F_{tool-samp}$, between the sample and sample substrate, $F_{samp-sub1}$, and between the sample and target substrate, $F_{samp-sub2}$.

The following conditions have to be met for a successful manipulation:

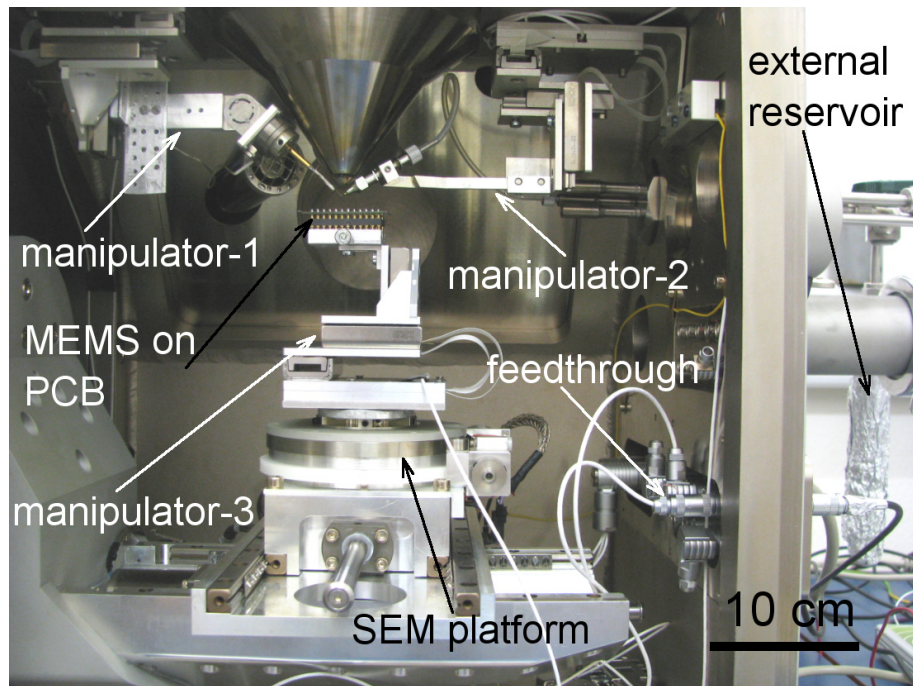
$$\text{Pick: } F_{tool-samp} > F_{samp-sub1},$$

$$\text{Place / release: } F_{tool-samp} < F_{samp-sub2}.$$

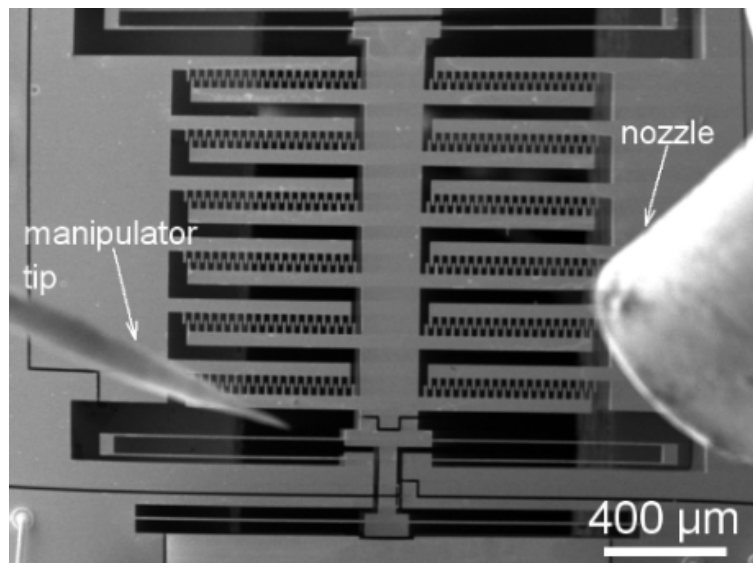
The commonly used tungsten tip in nanomanipulation is a passive end effector. The contacting force is difficult to be controlled by itself. For *in-situ* nanomanipulations, the above conditions could be met by the assistance of FEBID. For example, a weak nanosoldering is made between the manipulator tip and the sample while a stronger nanosoldering is made between the sample and the target substrate. The soldering materials can be hydrocarbon contaminates inside a SEM chamber or purposely injected precursor gas [Utke et al., 2008].

5.1.2 Experimental setup

The experimental setup for *in-situ* nanomanipulation is shown in figure 5.2(a) and (b), in which three sets of nanomanipulators are installed. An electrochemically etched tungsten tip was used to scratch the sample substrate gently and many single NWs were attached to the tip randomly. This tip (referred to as “sample-tip” to make a distinction with the “manipulator tip” in the follows) and the MEMS device were mounted close to each other on the manipulator-3. Another tungsten tip (manipulator tip) was bent to 30°-45° with respect to the horizontal plane and fixed on the manipulator-1. A homemade external gas injection system with a closing valve and organic-metallic precursor ((hfa)Cu-VTMS) was equipped on the SEM. The movement of the nozzle, connected to the external reservoir for introducing precursor gas, was controlled by the manipulator-2. The manipulator-2 and manipulator-3 were fixed on the sidewall of a SEM (Tescan Lyra, SEM/FIB) chamber, while the manipulator-1 was mounted on the SEM platform such that the MEMS device could rotate with respect to the manipulator tip by rotating the SEM platform. The coarse positioning was done with the manipulator-1 and manipulator-2, and the fine positioning was achieved by moving the manipulator-3. This is because that the manipulator tip is very susceptible to vibration during the step movement, which can easily result in a crash between the picked NW and the device substrate in the final approach.



(a)



(b)

Figure 5.2: (a) Experimental setup for *in-situ* nanomanipulation. (b) SEM image of the MEMS device, manipulator tip, and the nozzle for precursor gas injection.

5.1.3 Manipulation procedure

The main procedure of mounting an NW onto the MEMS device is: (1) an individual Co NW was chosen according to the length ($>10 \mu\text{m}$) from the sample-tip and picked up by

the manipulator tip. The joint between the manipulator tip and NW was made by FEBID of carbonaceous material for 1-2 min (figure 5.3a); (2) the MEMS device was positioned in the view of the SEM image (figure 5.3b). The NW was aligned with respect to the MEMS device by rotating the SEM platform; (3) the manipulator tip was approached toward the trench-1 (formed by deep reactive ion etching in Si) on the device, an obvious contrast change would be observed if the NW was lower than the device surface (i.e. the NW is inside the trench-1); (4) the NW was released onto the bottom or sidewall of the trench-2 (FIB milled) by another 2 min of FEBID of carbonaceous material between the one end of NW and the device. Push the manipulator tip against two ends of the NW by moving the manipulator-3 to make sure the NW is in contact with the device (figure 5.3c); (5) position the nozzle of the gas injection system close to the substrate and fixed the two ends of the NW onto the device by FEBID with the presence of precursor (figure 5.3d). Through these procedures, individual Co NWs (diameter ~300 nm) were mounted onto the MEMS device with a yield of around 80%.

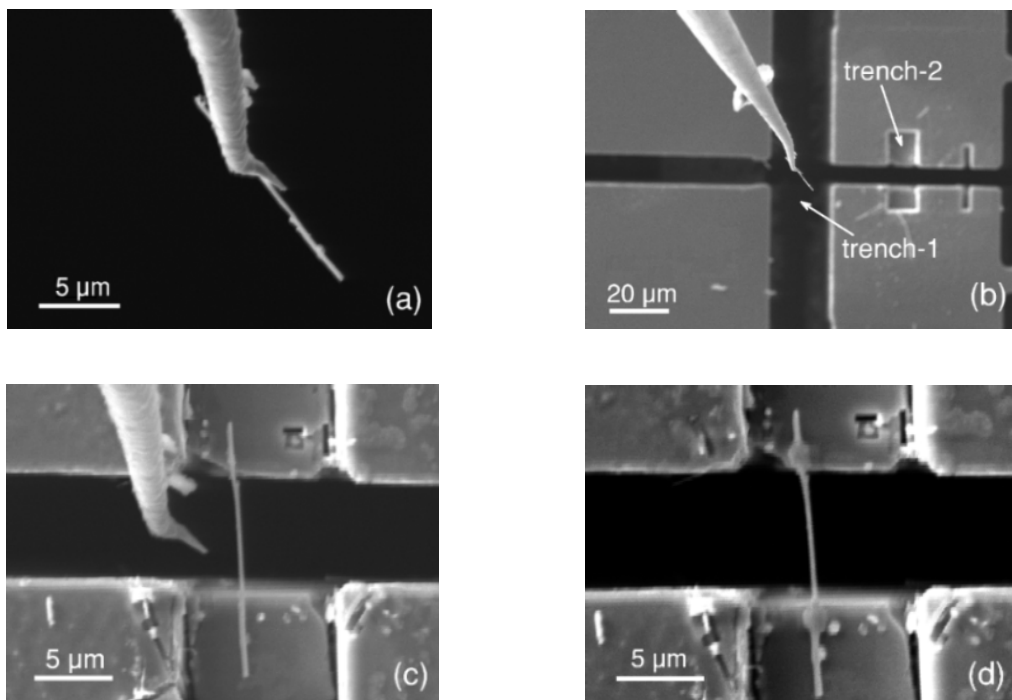


Figure 5.3: Nanomanipulation procedures to mount a single NW onto the MEMS device: (a) pick up one NW; (b) align the NW before approaching the tip to the device; (c) release the picked NW inside the trench; (d) fixing the NW onto the device by FEBID.

5.2 Nanowelding

5.2.1 Focused electron beam induced deposition

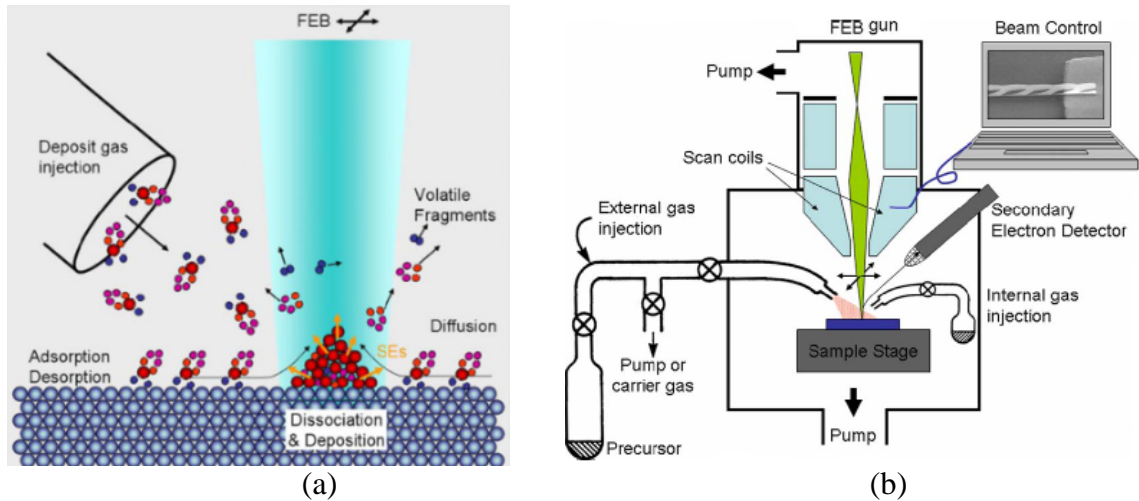


Figure 5.4: (a) Schematic of FEBID principle: molecules adsorb, desorb, and diffuse at the surface and are dissociated under electron impact. (b) Nanowelding fabrication system [Utke et al., 2008].

FEBID is used to fix the aligned NWs onto the MEMS devices. Figure 5.4(a) and (b) schematically show the principle and experimental system for the nanowelding process. When the primary e-beam impinges on a substrate, back scattered electrons (BSE) and secondary electrons (SE) are generated due to the elastic and inelastic interactions mechanisms, respectively. A chemical reaction happens between the electrons and the surface adsorbed molecules, and the nonvolatile dissociation products form the deposit grows coaxially into the beam, while volatile fragments are pumped away. It is still an open debate to which electrons the dissociation can be attributed for gas-assisted FEB processing [Utke et al., 2008]. For nanotensile testing, large volumes of FEBID has to be fabricated to increase the stiffness (to avoid large elastic deformation) of the soldered portions. Therefore, FEBID with high rate is highly desirable to reduce the deposition time, which could be achieved from the following methods:

(1) maximum the flux of precursor molecules at the FEBID location. For example, using a precursor gas of high vapor pressure and optimizing the nozzle position of the gas injection system.

- (2) operating the SEM at a large beam flux (i.e. high probe current).
- (3) decreasing the substrate temperature to enhance the absorption rate of the precursor molecules.
- (4) scanning the e-beam towards the precursor flux.

5.2.2 Mechanical characterization of FEBID

In tensile testing, the two clamping portions of a NW need to be strong enough to sustain a high tensile load (up to $\sim 200 \mu\text{N}$) and adhere well to the substrate without slippage. To maintain this condition, the mechanical properties of FEBID have to be known.

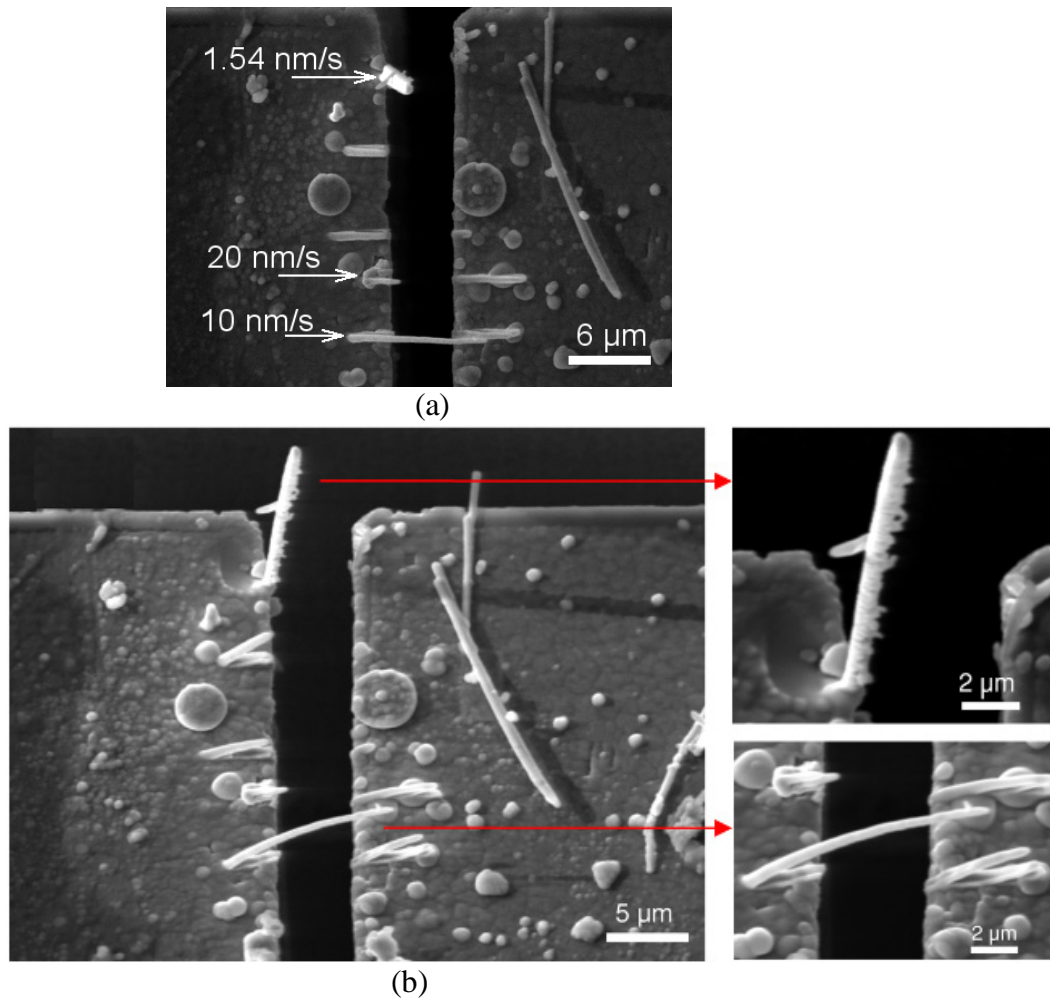
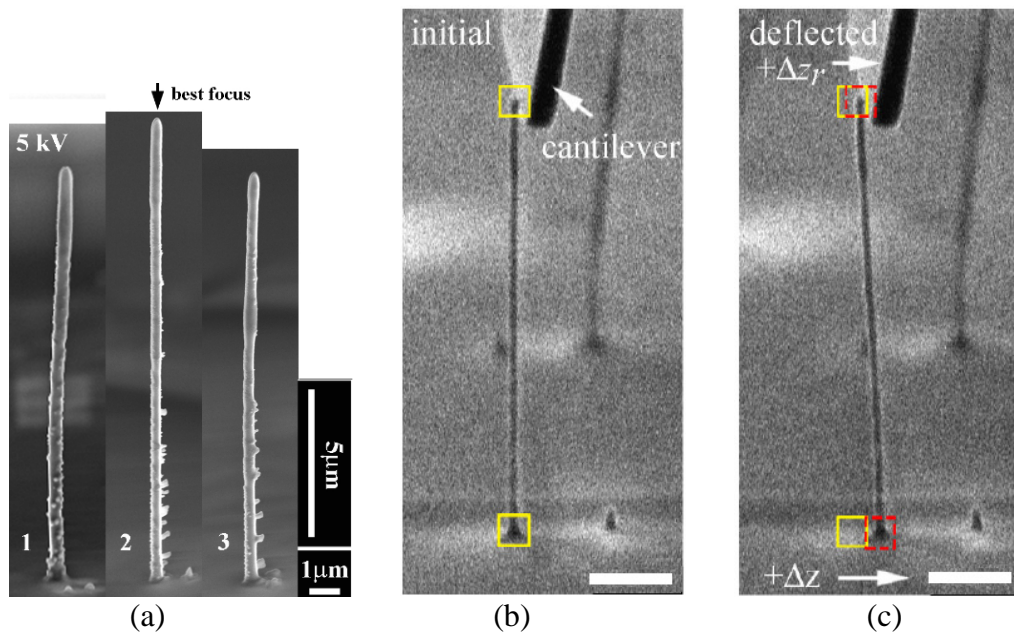


Figure 5.5: (a) Front-view of FEBID structures on a MEMS device. (b) Side-view (tilt 25°) of the FEBID structures, insets are close-up views of these deposited structures.

Tensile properties of the deposited material could be directly measured by the developed MEMS device if an individual NW bridging a gap in the device could be fabricated by FEBID. For this purpose, Co carbonyl (solid) was filled into a stainless steel syringe reservoir inside a dry nitrogen glove box. This reservoir was fixed onto a Smaract nanomanipulator and the precursor vapor is directed to the MEMS device by pointing the nozzle (0.9 mm diameter) to the device inside a SEM chamber (Hitachi, VP3600). The depositions were performed at a probe current of about 95 pA measured in a Faraday cup by a Keithley 6485 pico-amperemeter. E-beam lithography software (XENOS, Nano-Lithography System) controlled movement of the primary e-beam of the SEM. In XENOS, an individual line was written as a single scan with an incremental step size of 1 pixel (which is 1 nm according to the settings in XENOS). Three line patterns were deposited where the scan speeds of the primary e-beam were set to 1.54 nm/s, 10 nm/s, and 20 nm/s, and the corresponding dwell time (the time spent by the e-beam at every pixel) were 650 ms, 100 ms and 50 ms, respectively. SEM images of these three deposited structures are shown in [figure 5.5\(a\)](#). It can be seen that the lower the scan speed the larger the diameter of the deposited NWs. However, only the NW deposited at the speed of 10 nm/s successfully bridges the gap. As seen in [figure 5.5\(b\)](#), all the three structures were not grown horizontally, but were tilted. This finding suggests that the NWs grow in the vertical direction as well as in the horizontal direction. A higher scanning speed yields a structure of smaller tilted angles. However, a very high speed will make the NWs too thin to bridge the gap. Therefore, the fabrication of NWs by FEBID growing horizontally requires further optimization of the process parameters, such as the dwell time, precursor gas flux, and e-beam spot size. Since this work tended to be quite time-consuming, we didn't continue this experiment any more and no tensile measurements on the FEBID material was obtained.

Mechanical characterization of FEBID was performed by Friedli et al [[2009](#)] in the same group of EMPA under similar conditions. Pillars with aspect ratio >30 were deposited from the precursor $\text{Cu}(\text{C}_5\text{HF}_6\text{O}_2)_2$ on a Si substrate in a SEM as shown in [figure 5.6\(a\)](#). The probe current during deposition was 100 PA at an acceleration voltage of 5 KV, and the backpressure in the SEM chamber was 3×10^{-5} mbar. The deposition was executed for 30 min in continuous spot mode for each of the NW, which resulted in

NWs of about 15 μm long and 250 nm in diameter (average value). A micro-fabricated cantilever (stiffness is calibrated to be 0.019 N/m) was used to bend the deposited NW at its free end as shown in [figure 5.6\(b\)](#) and [\(c\)](#), from which the bending force and the NW deflection were measured. Thus the NW stiffness was measured. However, Young's modulus of the FEBID is difficult to determine accurately since the diameter of the grown NW is not uniform. To address this issue, resonance test on the same NW was performed, from which the resonance frequency was measured. FEA based on ANSYS was performed to extract the effective Young's modulus of the NW according to the measured values of stiffness and resonance frequency. The measured Young's modulus is between 10 and 30 GPa depending on the dose of the impinging electrons with an average value of about 20 GPa.



[Figure 5.6](#): SEM images of (a) three NWs deposited by 30 min (for each NW) FEBID, (b) a microfabricated cantilever contacting the NW and (c) the NW was bent by the cantilever. The scale bars in (b) and (c) are 3 μm [[Friedli et al., 2009](#)].

5.2.3 NW contamination during nanowelding by FEBID

[Figure 5.7\(a\)](#) shows a fragment of a Co NW after tensile tests, where a core-shell structure can be clearly observed. The core shows more ductility than the shell as suggested in [figure 5.7\(c\)](#). To measure the chemical composition of the shell, a

nanomanipulator tip was used to scratch the NW surface. A small piece of the shell material was slitted from the NW as shown in the [figure 5.7\(b\)](#). Energy dispersive X-ray emission (EDX) analysis was performed and the results for the shell and core were shown in [figure 5.8\(a\)](#) and [\(b\)](#), respectively. It is found that the shell has a very similar chemical composition as that of the welding material (Cu: C: O =17%: 53%: 29%, atomic ratio), which confirms that the shell is formed by FEBID. The EDX result shown in [figure 5.8\(b\)](#) shows that the core is rich of Co and is believed to be Co NW.

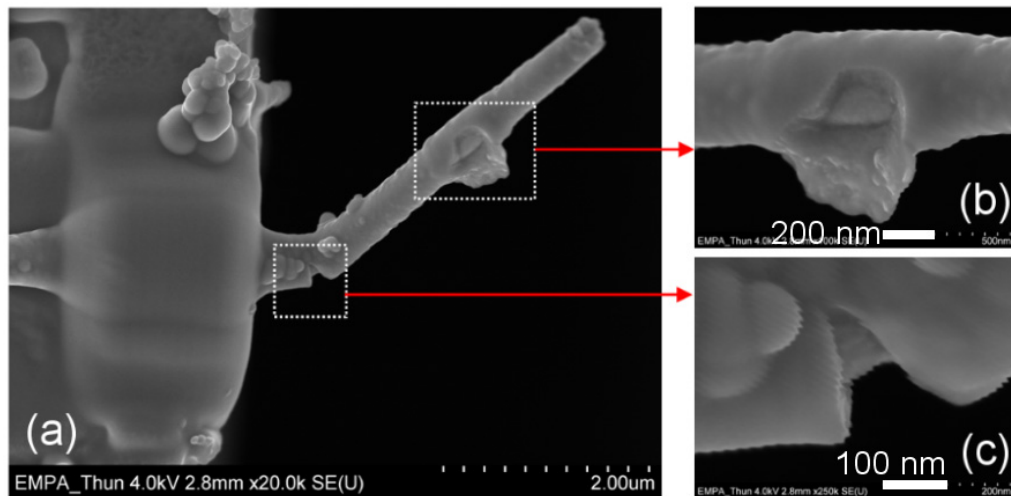


Figure 5.7: (a) HRSEM image of a fragment of a tested Co NW. (b) and (c) are close-up views of the NW showing a core-shell structure.

The contamination from FEBID is deleterious, which could result in a large error in the experimental results of a nanotensile test if not carefully treated. To quantitatively measure the thickness of the contamination deposited on the bridged NW during nanowelding, the diameter of a dummy bridged NW was measured with a HRSEM before and after the FEBID, as shown in [figure 5.9\(a\)](#) and [\(b\)](#), respectively. Several discernible features in the NW were chosen as the measuring points. The measured diameter differences before and after FEBID at these locations are plotted in [figure 5.9\(c\)](#). The FEBID conditions (e.g. the nozzle position, and the deposited area and time) were set to the same as those used in the nanotensile experiments.

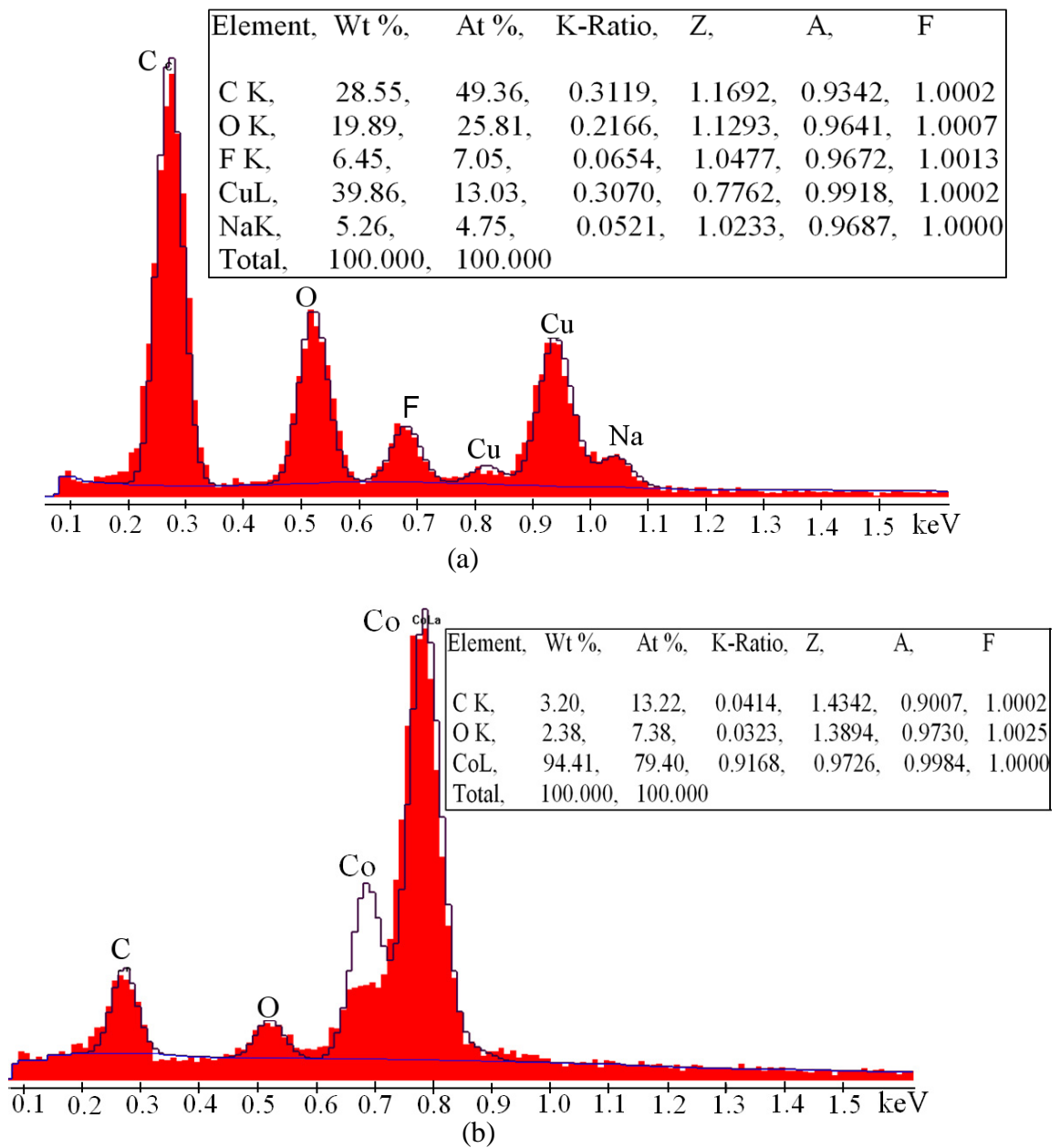


Figure 5.8: EDX spectrums of (a) the shell and (b) the core of the NW shown in figure 5.7.

It is found that regions as far as 2 μm away from the welding portions of the bridged NW is contaminated and becomes a little thicker. The NW was deposited with about 65 and 10 nm-thick contaminant thin films at the locations of 400 nm and 1.9 μm away from the welding area, respectively. Note that only one end of the freestanding NW was welded by FEBID here. The FEBID at the other end of a NW is expected to introduce

the same level of contaminations in the other end of the NW. The probable reasons of the FEBID besides the welding portions are the Gaussian-profile of the primary e-beam and the SE and BSE ejected from the sidewall of the FEBID as schematically shown in [figure 5.9\(d\)](#). As the nanowelding grows in the Z-direction, the SE and BSE generated from the FEBID would hit the adsorbed precursor molecule in the NW and cause extended deposition.

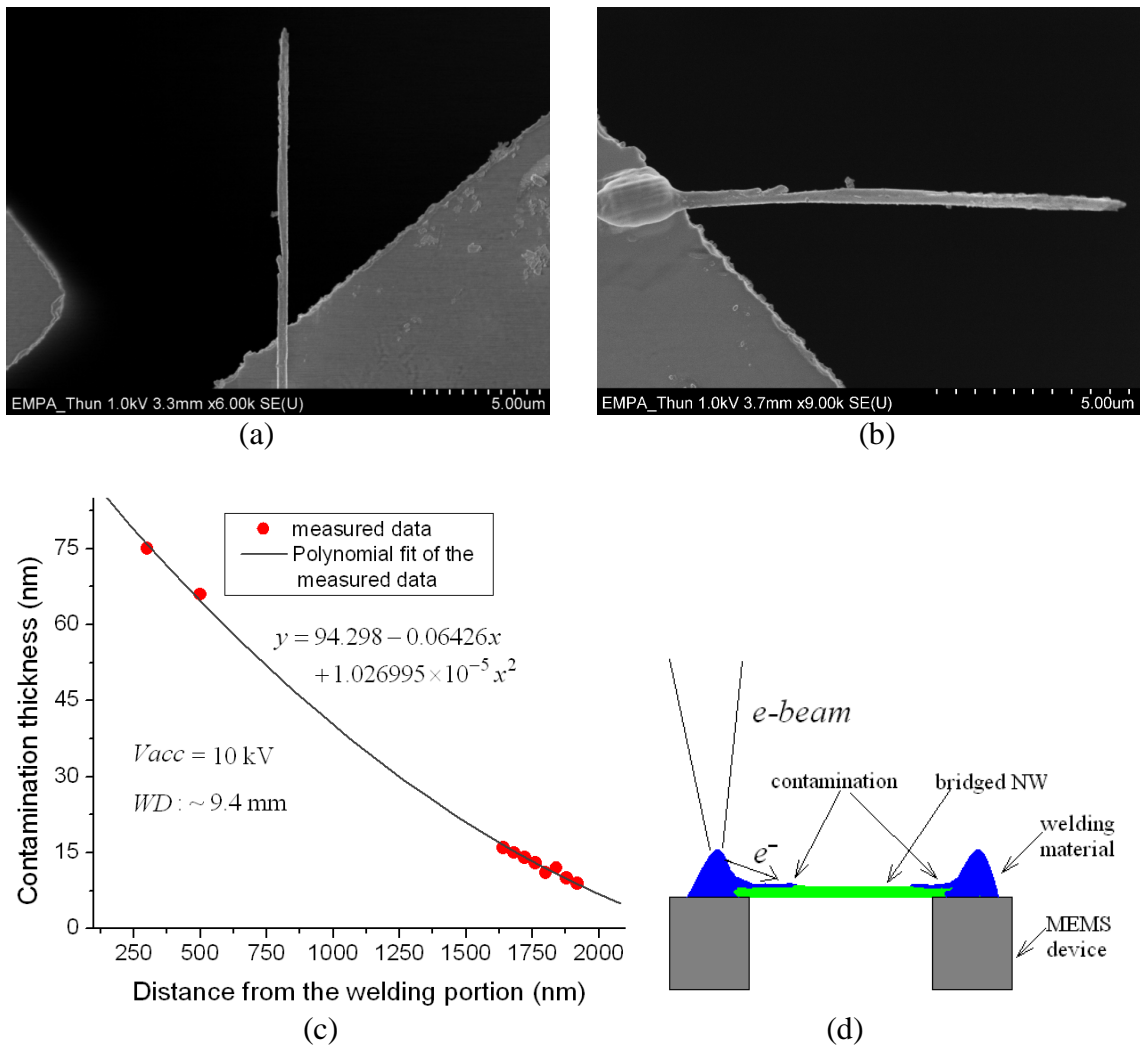


Figure 5.9: (a) and (b) are HRSEM images of a dummy Co NW attached on the MEMS device before and after performing FEBID, respectively. (c) The measured thickness of FEBID in the NW away from the welding portion. (d) Schematic of deposition in the NW by electrons emitted from the welding material.

5.3 Nanotensile measurements

Using the nanomanipulation setup and operation strategy described in [Section 5.1.3](#), nanotensile measurements on Si <111> NWs, Si <100> NWs, and Co NWs were performed inside a SEM. The SiNWs were synthesized by Dr. Silke Christiansen's group in the Institute of Photonic Technology (IPHT) at Jena, Germany, and the Co NWs were synthesized by Miss Barbara Cousin *et al.* at EMPA, Thun.

5.3.1 Si <111> nanowires

A. Nanowire synthesis

Si <111> NWs were prepared by the VLS method [[Stelzner et al., 2008](#)] using chemical vapor deposition (CVD) from silane (SiH_4) on a Si (111) substrate with B-doping (5-10 Ωcm). For that purpose the substrate was etched in diluted HF to remove the native oxide; subsequently, a 1-nm-thick Au film was sputtered on the substrate before the sample was transferred into the CVD chamber. The Si substrates were annealed at 650 °C at a high vacuum (1×10^{-7} mbar) for 10 min. The temperature was then reduced to 500 °C and a mixture of 5 sccm He and 4 sccm SiH_4 was introduced for the NW growth for 40 min at a pressure of 0.5 mbar. The NWs were *in-situ* doped during the growth process by adding 0.04 sccm 2% PH_3 in He to the process gases. As observed from SEM studies, the as-grown SiNWs with diameters between 20 and 200 nm have a typical length of 20 μm , and are straight with smooth surfaces.

B. Testing results and discussion

An individual SiNW was mounted on the MEMS device by nanomanipulation performed inside a SEM. The sample substrate was mounted close to the MEMS device inside the SEM chamber. An individual NW was picked up directly from the substrate with a sharp tungsten tip and transferred to the MEMS device. To eliminate the FEBID contamination induced error in the measurement of the NW diameter, the NW diameter was measured when it was placed onto the MEMS device and before performing the nano-welding via FEBID, as shown in [figure 5.10\(a\)](#). The inset in [figure 5.10\(b\)](#) shows a SEM image of the bridged SiNW on the MEMS device after the FEBID of copper-carbon composite. In our work, 30-40 min deposition was made at each end of the

nanowire with a pattern size of $1.6 \mu\text{m} \times 1.2 \mu\text{m}$, and the height of the deposits is measured to be about $1.2 \mu\text{m}$.

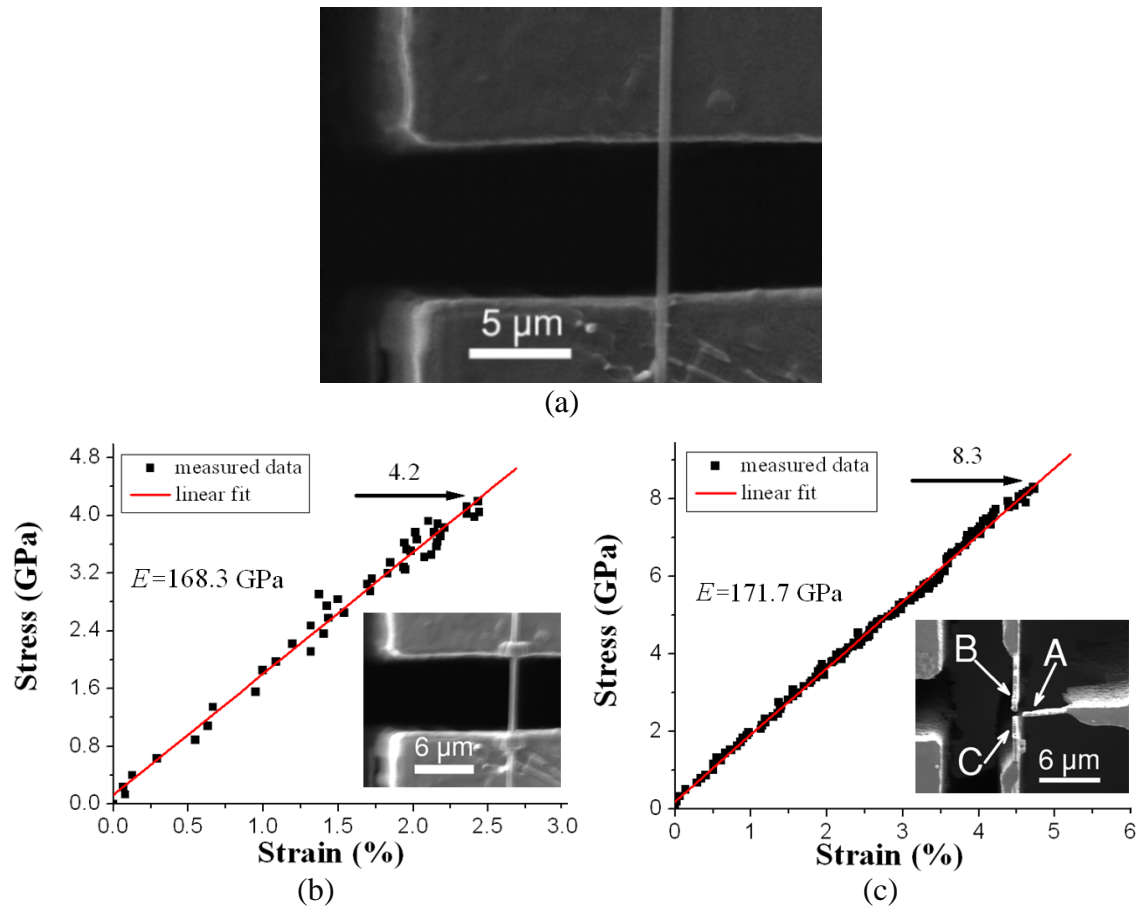


Figure 5.10: (a) SEM image of a SiNW bridging a gap in the MEMS device. Engineering stress-strain curves of SiNWs memasured with (b) device #1 and (c) device #3. Insets of (b) and (c) are SEM images of a NW welded to the device and the three-beam structure for measuring the tensile force and specimen elongation.

Two quasi-static tensile tests on the as-synthesized SiNWs were performed by using devices #1 and #3, respectively. During the testing with device #1, the specimen was observed continuously and a series of SEM images were recorded for the whole gauge length. The corresponding tensile load, i.e. the capacitive sensor output, was recorded through a digital multimeter. The two edges of the gap were used as the tracking marks in the subsequent image analysis to extract the specimen elongation. The engineering stress-strain curve of the test with device #1 was shown in [figure 5.10\(b\)](#). The measured modulus value is 168.3 GPa , which is the slope of the fitted line obtained from least-

squares linear regression of the experimental data. The NW (203.6 nm) was not fractured under a maximum tensile stress of 4.2 GPa.

During the testing with device #3, a three-beam structure as shown in the inset of [figure 5.10\(c\)](#) was observed continuously, from which the tensile force and specimen elongation could be extracted concurrently from SEM images. [Figure 5.10\(c\)](#) shows the engineering stress-strain curve obtained with device #3. Since the NW was not directly imaged during this testing, a very small amount of FEBID of carbonaceous material on the NW is expected. Therefore, the test can last longer and a smaller strain rate can be used. The second SiNW (198.4 nm in diameter) shows a Young's modulus of 171.7 GPa and is not fractured under a maximum strength of 8.3 GPa. The average Young's modulus of the two measurements is (170.0 ± 2.4) GPa. This value is consistent with the previous results reported in [[Gordon et al., 2009](#)] for Si $\langle 111 \rangle$ NWs grown by VLS technique. Our experimental results indicate that the as-synthesized SiNWs have a tensile strength of more than 8.1 GPa. This finding agrees with our earlier bending experiments on Si $\langle 111 \rangle$ NWs [[Hoffmann et al., 2006](#)] (reported tensile strength: 7-18 GPa) and the strength value of top-down fabricated Si nanostructures (10-20 GPa) reported in [[Namazu et al., 2000](#)], confirming again that the material strength increases as its size scales down [[Courtney, 2000](#)]. The measured E is 10% lower than that of bulk Si in the $\langle 111 \rangle$ direction (189 GPa), which could be attributed to the experimental error and/or the intrinsic material properties. The most relevant source of the experimental error is the measurement of the NW strain, which would be overestimated if the two soldering portions of the NWs are not rigid enough and result in an underestimation of E . However, this kind of experimental error is difficult to be quantitatively characterized inside a SEM. In [[Agrawal et al., 2008](#)], selective area diffraction (SAD) patterns taken under various loads during an *in-situ* TEM tensile test have been employed to measure the local atomic strain in a specimen, which is a promising way to overcome this issue and actually an advantage of *in-situ* TEM testing. In addition, the measurement of the NW diameter could be another probable source of the experimental error, since a 2% overestimation of the diameter (e.g. due to the finite diameter of the electron beam and the excitation volume of secondary electrons) will result in a 4% underestimation of E . The structural defects, e.g. twins and grain boundaries possibly formed during the VLS

process [Akhtar et al., 2008], could also lower E . However, further detailed microstructure analyses of these SiNWs by TEM are required to corroborate this speculation.

5.3.2 Si <100> nanowires

A. Nanowire synthesis

SiNWs, with the longitudinal direction along <100> obtained by an aqueous electroless chemical etching of single crystalline silicon wafers, were prepared and tested. Boron doped 4 inch Si (100) silicon wafers were used in the materials synthesis. The wet electroless deposition of silver (Ag) and wet chemical etching of Ag/Si surface mainly consists of two steps [Chen et al., 2008]. In the first step, silver nanoparticles were deposited on silicon surfaces simply by electroless deposition that occurs during immersing silicon surfaces in aqueous solution of 0.02 M silver nitrate (AgNO_3) and 5 M HF acid with 1:1 volume ratio (solution I) for 30 s. In the second step, silicon wafers, now covered with silver nanoparticles, were immersed into the etching solution of mixed 5 M HF and 30% H_2O_2 with 10:1 volume ratio (solution II) in a teflon vessel for 1 h at room temperature. During this step 1D Si nanostructures form. Finally, the material obtained after the etching procedure was rinsed several times in de-ionized water and blown dry. The wafers were then washed in concentrated (65%wt) nitric acid (HNO_3) for 15min to remove the residual Ag nanoparticles from the nanostructures surfaces. TEM analysis confirmed that these wet chemically etched SiNWs are single-crystalline as was the starting wafer and their long axis is along the axis of the surface normal [Peng et al., 2002]. However, the shapes of these 1D Si nanostructures are diverse, and ribbons, triangles and cylindrical wires could be found, as shown in figure 5.11(a). The actual shape adopted is mainly dependent on their diameters [Peng et al., 2002]. The HRSEM images indicate that most of the 1D Si nanostructures show a uniform shape along the wire axis and the NWs that have circular cross sections are generally the smallest in diameter (< 100 nm, see left inset of figure 5.11a).

B. Testing results and discussion

For easy manipulation inside an SEM (Dual beam SEM/FIB Tescan, with tungsten filament), two tests were performed (with device #3) on specimens that are 200-300 nm

thick. Specimens that are below 100 nm thickness are too small to be manipulated. The two specimens didn't have circular cross sections, which are very difficult to estimate their cross sectional areas due to the resolution limit and the two-dimensional imaging system of the SEM. Although the tensile load can be measured during testing, the stress can not be estimated accurately. Therefore, we report the load-displacement curves for this case, as shown in [figure 5.11\(b\)](#) and [\(c\)](#). By performing a linear fit (least-square) of the measured data, the stiffness of the samples is determined to be $K_S = 1643$ N/m and $K_S = 637$ N/m, respectively. The sample in [figure 5.11\(b\)](#) was not fractured under a tensile load of about 150 μ N, and the corresponding strain is about 1.2%. The specimen response seen in [figure 5.11\(c\)](#) is linear elastic until the catastrophic failure at a load of 168 μ N, and the corresponding strain is 3.9%. Note that this curve has an intercept in the vertical axis (i.e. the stress is not zero when there is no strain), which is due to the pre-deformation of the sensor's flexure. This pre-deformation is likely to be caused by a preload on the NWs generated during placing the NWs onto the device or by the FEBID induced surface stress at the two ends of the NW.

Since the longitudinal direction of these nanostructures is $\langle 100 \rangle$, we assumed that they have a Young's moduli of 130 GPa that is the same as that of the bulk Si $\langle 100 \rangle$. With $E=130$ GPa, the effective cross sectional areas of these 1D nanostructures can be determined from $S_{\text{eff}}=K_S l_0/E$, where l_0 is the initial gauge length of the specimen. The calculated effective cross sectional areas are $S_{\text{eff}}=350^2\pi/4$ nm² and $S_{\text{eff}}=200^2\pi/4$ nm², respectively, which correspond to 350 and 200 nm in diameter if assumed that they have circular cross sections. With this method, the fracture strength of the Si [100] nanostructures is determined to be 5.4 GPa from the curve shown in [figure 5.11\(c\)](#). This result is close to the tensile strength of single crystal Si $\langle 100 \rangle$ specimen of micrometer size reported in [[Ando et al., 2001](#)] (5.2 GPa). Note that the surface defects (see the left inset of [figure 5.11a](#)), introduced during the wet chemical etching of Si $\langle 100 \rangle$ nanostructures, can lead to stress concentration and initiate failure and reduce the tensile strength significantly.

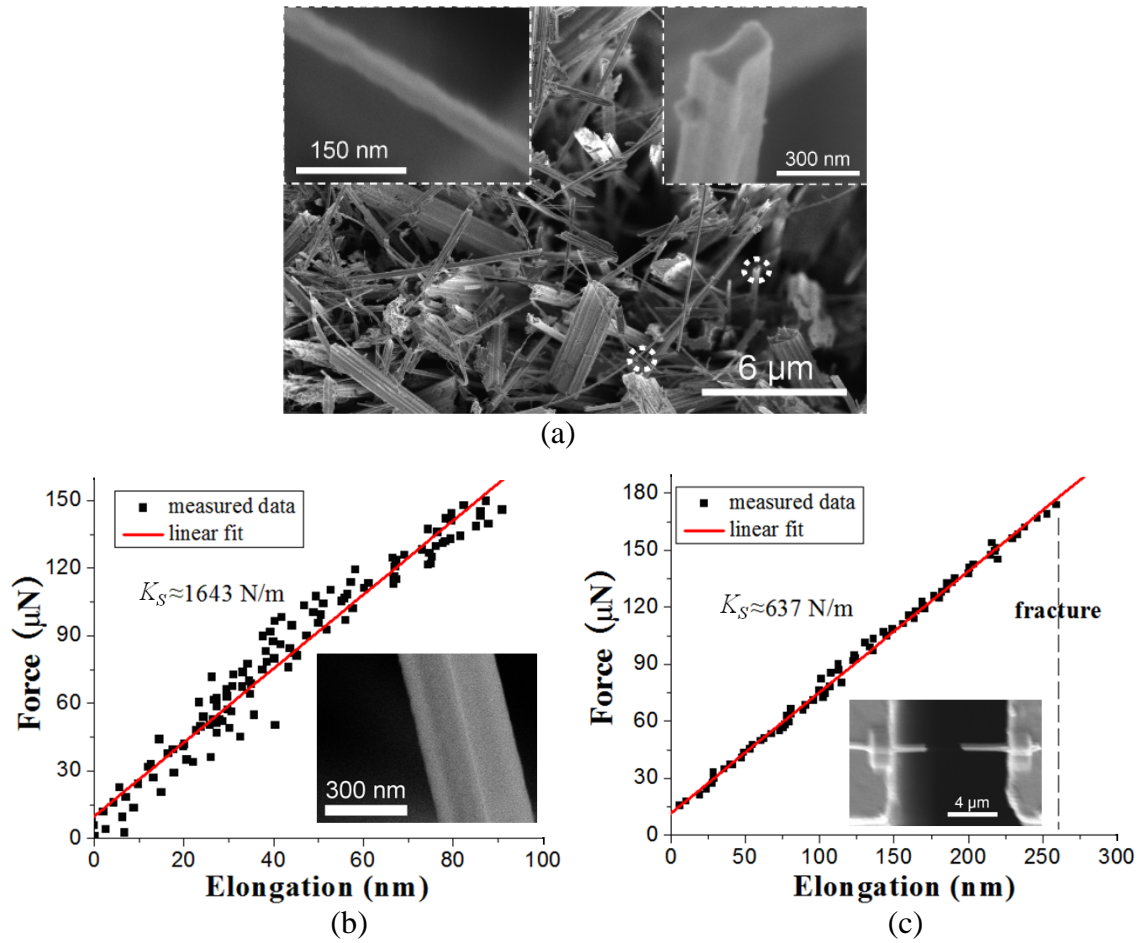


Figure 5.11: (a) HRSEM images of the wet chemically etched 1D Si nanostructures. Left inset shows the rough surface of a SiNW with diameter of about 45 nm, and right inset shows the cross section of a nano ribbon. (b) and (c) are the load-displacement curves of the two tests on these 1D Si nanostructures. Inset of (b) is a HRSEM image of the tested specimen, and inset of (c) is an SEM image of the fractured specimen.

5.3.3 Co nanowires

A. Nanowire synthesis

Co NWs were synthesized using EDP in porous polycarbonate membranes at room temperature [Philippe et al., 2007]. A 200-nm-thick gold layer evaporated onto one side of the membrane served as the back electrode. A Pt circular grid and a saturated-calomel electrode (SCE) were used as the counter and reference electrode, respectively. The deposition was carried out in a DC mode with overpotential of -1 V. The electrolytic solution was composed of CoSO_4 (1M), H_3BO_3 (0.7M) and NaCl (0.11M) with a pH

value of 3.5. Extraction of NWs from the template was performed by gold layer and then polycarbonate membrane chemical dissolution. Figure 5.12(a) shows a SEM image of the extracted Co NWs. The NWs density is so high that most of them are intervened with other NWs, which need to be separated for easily picking up. The HRSEM image, as shown in the inset of figure 5.12(a), shows the rough surface of the NWs that is commonly observed in electroplated thin film or NWs. As seen in figure 5.12(b), the as-synthesized Co NWs are nanocrystalline and exhibit variations of grain sizes (10-150 nm) and crystal orientations analyzed by means of TEM and selected area electron diffraction (SAED) techniques [Philippe et al., 2009].

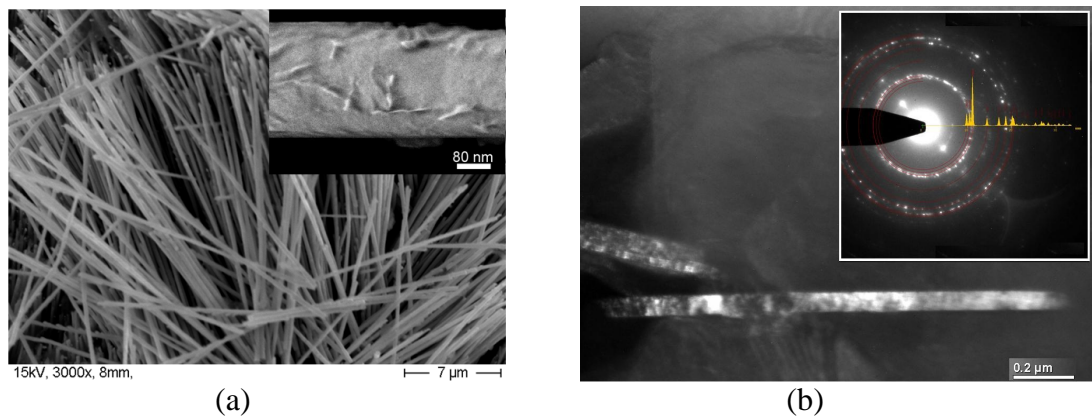


Figure 5.12: (a) SEM image of extracted Co NWs from template. Inset is a HRSEM image of a single Co NW showing the rough surface. (b) TEM image of a Co NW. Inset is a SAED pattern, which reveals that this Co NW exhibits variations of crystal orientations (polycrystalline).

B. Testing results and discussion

Quasi-static tensile tests on as-synthesized Co NWs were performed for eight samples. During testing, the three-beam structure was imaged at high magnification (~25K) and consecutive images (1024×576 pixels) were taken automatically by the SEM. The specimen elongation and the sensor deformation in each frame were measured with an accuracy of subpixel with a program based on a cross correction algorithm [Hoffmann et al., 2007]. After experiments, the fragments were carefully bent a little upward by a manipulator tip from the fixed part for imaging the fractured cross section in a HRSEM.

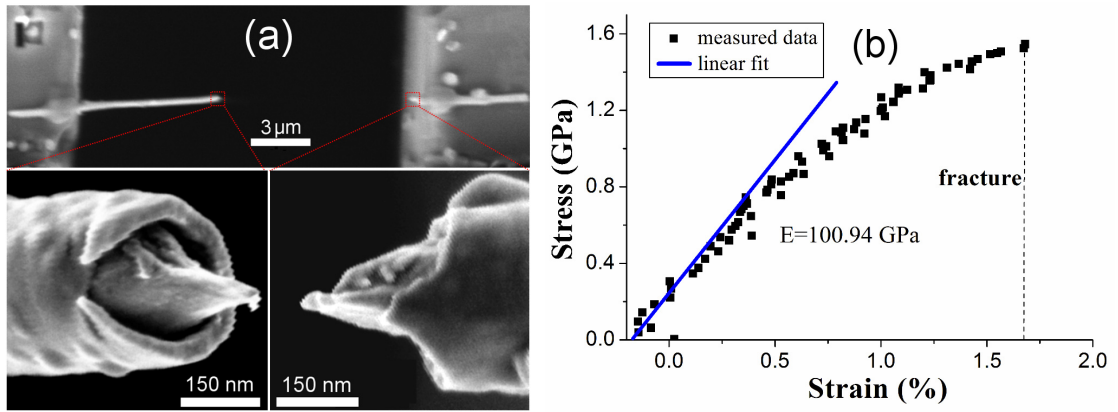


Figure 5.13: (a) SEM images of a fractured NW and its cross sections. (b) Typical stress-strain curve of the tested Co NWs.

Table 5.1: Tensile testing results of Co NWs.

NW diameter (nm)	Original length (μm)	Fracture strain (%)	Tensile strength (GPa)	Young's modulus (GPa)
285	8.75	1.89	1.41	74.97
289	7.75	3.57	2.00	54.59
289	7.07	2.05	1.58	76.32
342	7.45	1.70	1.57	100.94
315	7.54	NA	NA	79.48
340	7.55	2.14	2.04	79.88
278	7.82	1.82	1.30	79.48
368	8.74	1.90	1.08	56.55
Average ^a		2.2±0.6	1.6±0.4	75.3±14.6

^a The average is expressed in the form of “the mean ± the standard deviation”.

A core-shell structure is observed as shown in [figure 5.13\(a\)](#), where the core shows higher ductility than the shell. EDX analysis on the shell (which was slitted from the NW by a manipulator tip confirms that it is formed by FEBID, since it has a very similar chemical composition as that of the welding material. All the NW diameters were measured after they were aligned on the MEMS device and before performing FEBID. [Figure 5.13\(b\)](#) is a representative engineering stress-strain curve of the tested Co NWs, where a failure strain of about 1.7% is measured. Note that this curve has an intercept in the vertical axis, which is due to a pre-deformation of the sensor's flexure. This pre-deformation is likely to be caused by a preload on the NWs generated during placing the NWs onto the device or by the FEBID induced surface stress at two ends of the NW.

The modulus value shown in [figure 5.13\(b\)](#) is the slope of the fitting line obtained from least-squares linear regression of the measured data in the range of 0-0.8 GPa, which is assumed to be the elastic deformation range (i.e. the yield strength is assumed to be 0.8 GPa) of the tested Co NW.

Eight NWs were tested and the overall tensile results are summarized in [table 5.1](#). The measured higher tensile strength (1.6 ± 0.4) GPa and lower fracture strain (2.2 ± 0.6) % than those of bulk polycrystalline Co (0.9 GPa and 6%-19%) reported in [[Karimpoor et al., 2006](#)] can be attributed to the small grain size of the Co NWs, since a similar trend in the increase of material strength and decrease of the ductility are commonly observed for many other nanocrystalline metals compared with their coarse-grained counterparts [[Meyers et al., 2006](#)]. The measured strength value is comparable to that of bulk nanocrystalline Co (1.9 GPa) [[Karimpoor et al., 2006](#)], but it is significantly lower than the theoretical strength of monocrystalline Co [[Soboyejo et al., 2007](#)] (which is about 1/10 of the Young's modulus). The measured apparent Young's modulus (75.3 ± 14.6) GPa is well below the value for bulk nanocrystalline Co (209 GPa) [[Karimpoor et al., 2006](#)].

In the experiments, specimen elongation is measured from the distance increase between the beams B and C (see the inset of [figure 5.10c](#)). Hence, any slippage between the FEBID material and the device (due to poor adhesion) will be mistaken as the specimen elongation, which yields an underestimation of E . Co NWs were fixed onto the device by FEBID of a carbon-copper composite. No failure or dislocation at the fixed portions was observed in all of our measurements, i.e. the slippage can be excluded. A 1500 nm by 1000 nm pattern was deposited for about 30 min at each end of the NW, which yielded a thickness of 1.1-1.3 μm of the carbon-copper deposition. According to our previous mechanical characterization, this welding material has an elastic modulus of about 20 GPa [[Friedli et al., 2009](#)]. The stiffnesses of the clamping portions were estimated to be an order of magnitude higher than those of the tested Co NWs, thus the elastic deformation of the soldering parts can be neglected compared to the NWs elongations. In addition, in all of our measurements, the in-plane misalignment angle is $<5^\circ$ which causes the underestimation of E less than 3% [[Li et al., 2005](#)]. Simulations have shown that the surface roughness does not have an appreciable effect on the elastic

modulus of metal NWs [McDowell et al., 2008]. The probable reasons for the reduction in the Young's modulus are structural defects (e.g. pores) present in the NWs [Kovacik, 1999; Sakai et al., 1998; Liu et al., 2006; Varghese et al., 2008] and surface effects (e.g. surface oxide and surface contamination) [Jing et al., 2006]. The similar trend of a reduction in E was previously reported for NWs of other compositions, such as WO_3 [Liu et al., 2006], Co_3O_4 and CoO [Varghese et al., 2008], and ZnO [Ni et al., 2006; Song et al., 2005]. However, to corroborate these arguments, further detailed studies on the NWs microstructure and/or density are necessary. Since the tested samples are of similar size, no obvious size dependence of the strength or Young's modulus can be observed, neither on the NWs diameter, length nor volume.

There are inevitable uncertainties which exist in the measurement of the specimen size, the sensor stiffness, and the displacements of the beam A, B and C (see the inset of figure 5.10(c)). Assuming the Co NWs have a homogeneous cross section of diameter D , Young's modulus E based on continuum mechanics can be given by

$$E = \frac{4}{\pi} \frac{K_0(x_C - x_A)}{D^2} \frac{l_0}{x_B - x_C}, \quad (5.1)$$

where l_0 is the initial length of the NW. The terms $x_C - x_A$ and $x_B - x_C$ denote the sensor deformation and the specimen elongation, where x_A , x_B and x_C are the monitored displacements of the beams A, B and C, respectively. The propagated percentage uncertainty [Taylor 1997] into the Young's modulus can be estimated by

$$\frac{\Delta E}{E} = \sqrt{\left(\frac{\Delta K_0}{K_0}\right)^2 + 4\left(\frac{\Delta D}{D}\right)^2 + \left(\frac{\Delta l_0}{l_0}\right)^2 + \left[\frac{(x_B - x_A)\Delta x_C}{(x_C - x_A)(x_B - x_C)}\right]^2 + \left(\frac{\Delta x_A}{x_C - x_A}\right)^2 + \left(\frac{\Delta x_B}{x_B - x_C}\right)^2}, \quad (5.2)$$

where ΔD , Δl_0 , Δx_A , Δx_B and Δx_C are the measurement uncertainty of NWs diameter, NWs initial length and displacement of the beam A, B and C, respectively.

$\frac{\Delta K_0}{K_0} = \sqrt{\left(\frac{\Delta h}{h}\right)^2 + \left(\frac{\Delta L_s}{L_s}\right)^2 + \left(\frac{\Delta W_s}{W_s}\right)^2 + \left(\frac{\Delta L_b}{L_b}\right)^2 + \left(\frac{\Delta W_b}{W_b}\right)^2}$ is the propagated percentage uncertainty of the sensor stiffness due to the measurement uncertainty in the beam size, i.e. Δh , ΔL_s , ΔW , ΔL_b and ΔW_b (assuming the measurement uncertainty of the resonance frequency

is neglectable). It is seen that a precise measurement of the NWs diameter is crucial for an accurate calculation of the Young's modulus. The statistical error can be reduced by taking the mean value of several measurements in a HRSEM. However, the systematic error due to the finite diameter of the e-beam and the excitation volume of secondary electrons will overestimate D and consequently underestimate E (see [equation 5.1](#)). Since x_A , x_B and x_C are measured from SEM images with a program [[Hoffmann et al., 2007](#)], Δx_A , Δx_B and Δx_C can be treated as fixed values that are subpixel size (typically a few nanometers). When the tensile load is very small, NWs have little elongation (i.e. $x_B \approx x_C$), the measurement uncertainty of E can be quite large. This can explain the relatively large data scattering in the low strain range as shown in [figure 5.13\(b\)](#). From the medium to high strain range, the measurement uncertainty of E is dominated by the measurement uncertainties in k_s , D and l_0 , which is estimated to be about 18% with a moderate assumption of $\Delta h/h = \Delta L_s/L_s = \Delta W_s/W_s = \Delta L_b/L_b = 3\%$, $\Delta l_0/l_0 = 5\%$, $\Delta W_b/W_b = 3\%$, and $\Delta D/D = 8\%$. The value of $\Delta D/D$ is assumed to be a little large by taking into account the SEM imaging, surface roughness and possible carbonaceous depositions during nanomanipulation. The propagated uncertainty in E from [equation 5.2](#) could explain the spread of the measured E listed in [table 5.1](#).

5.4 *In-situ* electrical measurement

Apart from mechanical testing, on-chip electrical circuit is designed to measure the electrical properties of specimen under various loads. However, due to the difficulties of making ohmic contacts between SiNWs and metal electrodes inside a SEM, the giant piezoresistance of SiNWs reported in [[He, et al., 2007](#)] could not be measured with our MEMS device. The main difficulties in *in-situ* electrical measurements are discussed and the possible solutions are proposed in the follows.

A. Carbonaceous contamination and inherent oxide layer at the sidewall of SiNWs

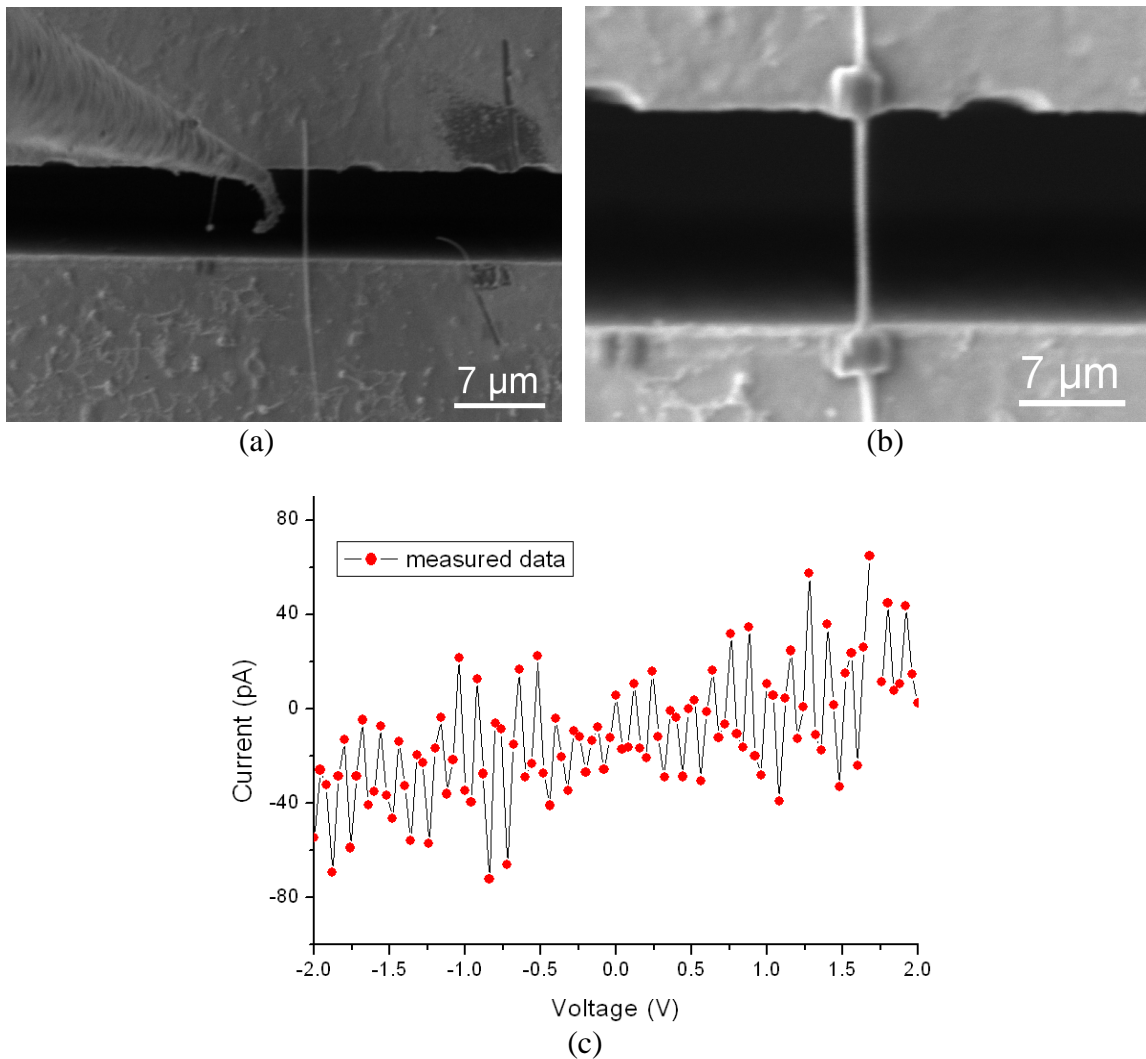


Figure 5.14: (a) SEM image of SiNW bridging on the metal electrodes. (b) SEM image of the SiNW welded on the electrodes by FEBID. (c) I-V curve of the SiNW shown in (a).

During *in-situ* nanomanipulation, SiNWs are exposed to the primary e-beam, which could deposit carbonaceous material in the NWs due to the residue hydrocarbons in the SEM chamber. These deposited materials are of unknown electrical resistivity since they are composed of amorphous carbon and oxide, and the deposited thickness depends on the vacuum quality of SEM chamber. In addition, TEM study has found that there is a native oxide layer of up to several nm at the sidewall of SiNWs [Stratakis et al., 2008]

grown by the conventional VLS technique. These carbonaceous contamination and oxide shell layer could act as an electrical insulator, which prevent the formation of ohmic contacts. This is verified by a current-voltage (I-V) measurement of a SiNW that is aligned on the metal electrodes of the MEMS device but was not fixed as shown in [figure 5.14\(a\)](#). The measured very high resistance ($\sim 10^9 \Omega$, see [figure 5.14c](#)) indicates that the SiNW is electrically insulated from the electrodes. After this SiNW was soldered onto the device by FEBID with the precursor gas of (hfa)Cu-VTMS, as shown in [figure 5.14\(b\)](#). The measured resistance is still in the order of $10^9 \Omega$ and there is no significant change.

A high vacuum quality of the SEM chamber is desired to mitigate the carbonaceous contaminations during *in-situ* nanomanipulation, and the primary e-beam should not focus on the specimen for long time. These carbonaceous contaminations and native oxide layer could be removed before making the nanowelding by focused ion beam with careful operation.

B. The out of beam sight effects in FEBID

As discussed in [Section 5.2.3](#), some regions of a bridged NW will be contaminated during the nanowelding process by FEBID. The welding material with high conductivity are desired to facilitate electrical measurement, however the deposited material on the NW out of the welding portions could act as a current leak. Therefore, the accuracy of the electrical measurement could be significantly decreased by these contaminations.

To diminish the out of beam sight deposition during nanowelding, the height of the deposited material at the soldering portions should be kept low. However, a firm fixation of the specimen on the device has to be ensured at the same time. Alternative techniques to fix an individual NW onto the tensile stage, which can provide mechanical fixation and good electrical contact (low resistance ohmic contact), are highly desirable for this purpose.

C. High resistivity of FEBID

For electrical measurement, large contact resistances should be generally avoided. When using organometallic precursors, a low metal content carbonaceous matrix embedding and separating numerous nanosized metal clusters is formed. The high carbon content in

the deposits results from both the oil vapors in the SEM pumping system and to a higher extent from the carbon rich precursor ligands. The electrical resistivity deposited by FEBID with organometallic precursor is generally 2-4 orders of magnitude higher than those of the bulk metal [Utke et al., 2002]. Inorganic carbon free volatile metal precursor could be used to fabricate the nanoweldings with high metal content. For example, an electrical resistivity of $22 \mu\Omega\text{cm}$ at 295 K (ten times the bulk Au value) has been obtained in FEBID with inorganic PF_3AuCl precursor [Utke et al., 2000].

A common strategy to eliminate the contact problem is to use four-point measurement scheme, which is usually executed on a planar insulating substrate, where the dispersed NWs on the substrate can be contacted at different locations along their longitudinal direction by e-beam lithography technique. Integration of a four-point measurement into the nanotensile stage is challenging due to the complicated fabrication process and the fact that only relatively long NWs can be tested. Another way to conduct two-point electrical measurement that could possibly avoid the problem of large contact resistance is impedance measurement based on an impedance spectroscopy [Barsoukov et al., 2005], which has been widely used in biophysics to study the electrical phenomena in living things [de Lorenzo et al., 1997]. In this case, the two contacts of the NWs have to be made by dielectrics (which are easier than deposition of pure metal by FEBID), and thus the contact portions could be modeled as a parallel circuit of a resistance and a capacitance. It should note that the large parasitic capacitance associated with electrostatic MEMS devices should be taken into account when interpreting the impedance results.

The resistance change of the Si suspensions caused by the stretching during tensile testing was measured with a device where there was no gap between the actuator and the force sensor. The resistance between connections V1 and V2 was measured to be $(122.515 \pm 0.020) \Omega$ (see figure 2.4b) when there was no voltage applied to the actuator (i.e. the Si suspensions were not stressed). Under a drive voltage of 100 V, the actuator moved about $4.5 \mu\text{m}$, the resistance between connections V1 and V2 changed to $(122.540 \pm 0.030) \Omega$. It can be seen that the resistance change of the suspensions is less than $50 \text{ m}\Omega$, which suggests that in the piezoresistance measurement of SiNWs, the 2-point connections could be used.

The above issues, hindering the on-chip electrical measurements, are possibly to be addressed by using FIBID to fabricate the electrical contacts between the nanowire and the electrode since: (1) the ion beam could remove the carbonaceous contamination and the inherent oxide layer at the sidewall of SiNWs before performing FIBID; (2) the electrical resistivity of FIBID is generally much lower than that of FEBID. FIBID also has an advantage of high deposition rate that necessitates much shorter time (< 10 min) than FEBID. However, the out of beam sight effects during FIBID might be unavoidable. In practice, FIBID should be carried out while the SEM platform is tilted with a large angle (52° in our case) so that the sample surface is normal to the ion beam. This requirement renders significant challenges for the nanomanipulation as discussed in [section 5.1.1](#). Furthermore, a major limitation of the current design has been found, which is the high susceptibility to vibrations (it will be discussed in detail in [Chapter 6](#)). This limitation does not allow us to tilt the SEM platform after a nanowire is placed on the device. Therefore, critical improvements in the mechanical design of the testing system (especially the dynamic stability) are required to enable the on-chip electrical measurements. Electrical measurements of SiNWs were performed separately in this thesis by a probe-based electron beam induced current (EBIC) method, which is presented in [Appendix B](#).

5.5 Summary

A novel strategy of modifying device topography, e.g. in the form of trenches and pillars, was proposed to facilitate *in-situ* SEM pick-and-place nanomanipulation, which could achieve a high yield of about 80% and reduce the difficulties in specimen preparation for tensile testing at the nanoscale. It was found that certain regions (as far as 2 μm away from the welding part) of a bridged NW was contaminated and became a little thicker due to the nanowelding process. These FEBID contaminants are thought to have negligible contributions to the mechanical loading of the tested Si and Co NWs ($D \sim 300$ nm), but they can possibly introduce errors in the NW diameter measurement. Therefore, all the NWs diameters have to be measured after they were aligned on the MEMS device and before performing FEBID. Phosphors-doped Si <111> NWs grown by VLS mechanism show an average Young's modulus of (170.0±2.4) GPa and a tensile

strength larger than 8.3 GPa. Si <100> NWs produced by electroless chemical etching were also tested, and a tensile strength of 5.4 GPa were determined from the measured load-displacement curves. The apparent Young's modulus, tensile strength and fracture strain of Co NWs were measured to be (75.3 ± 14.6) GPa, (1.6 ± 0.4) GPa and (2.2 ± 0.6) %, respectively. These unusual results of Co NWs compared to their bulk counterparts suggest that a great caution has to be paid when integrating them into NEMS as mechanical functional components. The main difficulties in performing *in-situ* electrical testing with the developed MEMS devices were discussed. The developed MEMS device and experimental techniques is expected to contribute to the experimental studies in nanomechanics.

This page intentionally left blank

6.

Conclusion and outlook

6.1 Conclusion

This thesis presents the design, fabrication, characterization and application of a novel nanotensile stage for *in-situ* electron microscopy mechanical testing of 1D nanostructures, like nanowires and nanotubes.

Two types of electrostatically actuated nanotensile stages were designed. The first one consisted of a comb-drive actuator and a differential capacitive force sensor, and the second one combined a comb-drive actuator with a clamped-clamped beam force sensor. Two functions were designed in both types of designs, namely, mechanical tensile testing and electrical testing. In tests, individual 1D nanostructures were mounted on the devices via SEM based nanomanipulation and FEBID. The specimen elongation was measured from SEM images with a program based on a cross correlation algorithm. The corresponding tensile force was measured either electronically (with the capacitive sensor) or by measuring beam deflection from SEM images (with the clamped-clamped beam force sensor). For electrical testing, the device surface was coated with thin metal films, and the electrical insulations among different electrodes were realized by deep trenches fabricated in the device layer of a SOI wafer.

To enable high force output at relative low drive voltages while keeping device footprints small, three strategies were adopted in the comb drives employed in the tensile stages: (1) high-aspect-ratio structures (finger height/gap=20) were designed in comb drives, which took benefit of DRIE in a SOI wafer; (2) suspensions stiffness of comb drives were kept low according to the developed modeling of the system; (3) geometries of comb drives were optimized by FEA, which reduces sizes of individual comb fingers and thus enables integrating more comb-finger pairs given the same device footprint. The influence of the parasitic force arising from the excitation voltage of the sensing

electrodes of a capacitive sensor on the sensor's stability, linearity and sensitivity was studied analytically.

The MEMS devices were fabricated in a SOI wafer by an optimized DRIE based process. The notching effect and the serious under-etching induced by thermal effects during DRIE were mitigated in our process. The fabricated comb drives (with 240 pairs of comb fingers) could output tensile force of about 210 μN at a drive voltage of 120 V, and the developed force sensors could achieve a resolution of better than 50 nN. The in-plane stiffness of sensors and actuators were calibrated by a resonance method and agreed well with the analytical values calculated from the measured suspension dimensions.

A novel strategy of modifying device topography, e.g. in the form of trenches and pillars, was proposed to facilitate *in-situ* SEM pick-and-place nanomanipulation, which could achieve a high yield of about 80% and reduced the difficulties in specimen preparation for tensile testing at the nanoscale. In the tensile stage consisting of a comb drive and a clamped-clamped beam force sensor, a "three-beam structure" was fabricated by FIBID, from which the specimen elongation and the tensile force could be measured concurrently from SEM images at high magnification (typically 20K-100K). This improved the displacement measurement resolution significantly and added much convenience for the data processing.

The mechanical testing capabilities of the developed tensile stages were demonstrated by tensile tests on individual nanocrystalline Co NWs, Si $\langle 111 \rangle$ NWs, and Si $\langle 100 \rangle$ NWs. The measured apparent Young's modulus, tensile strength and fracture strain of the electrochemically deposited Co NWs were (75.3 ± 14.6) GPa, (1.6 ± 0.4) GPa and (2.2 ± 0.6) %, respectively. The phosphorous-doped Si $\langle 111 \rangle$ NWs, grown bottom up by the VLS technique, showed an average Young's modulus of (170.0 ± 2.4) GPa and a tensile strength larger than 8.3 GPa. The measured tensile strength of Si $\langle 111 \rangle$ NWs is much larger than that of bulk Si $\langle 111 \rangle$, which confirms that the strength of materials increases as their sizes scale down. The top down electroless chemically etched Si NWs with their long axis along the $\langle 100 \rangle$ direction of the starting silicon wafer show a tensile strength of about 5.4 GPa.

6.2 Outlook

Although the developed nanotensile stages proved capable of studying mechanical properties of 1D nanostructures inside a SEM, several important design and operation issues have to be addressed to further improve the system performance. These fall under the scope of future work and are outlined in follows.

6.2.1 Clamping mechanism

One major limitation of the current design is the high susceptibility to vibrations due to the low resonance frequencies of the employed actuators and sensors. For this reason, once a NW is mounted on the MEMS device, the device should not be dismantled from the SEM platform. It has been found that only moving the SEM platform (e.g. tilting) could result in specimen failure. The developed testing stages could not be used for *in-situ* TEM study since the specimen preparation has to be done inside a SEM and the MEMS device require mounting again on a TEM holder. One possible solution of this issue is to reduce the masses of the shuttles in the actuator and sensor, and thus, to increase the resonance frequencies of them. This might be realized by reducing the handle layer thickness during micro-fabrication with another mask for the handle layer lithography, as schematically shown in [figure 6.1\(a\)](#) and [\(b\)](#). If there is no electrical insulation gaps in the device layer in these shuttles (i.e. omitting the on-chip electrical circuit, see [figure 2.4b](#)), the handle layer of the shuttles can be completely removed.

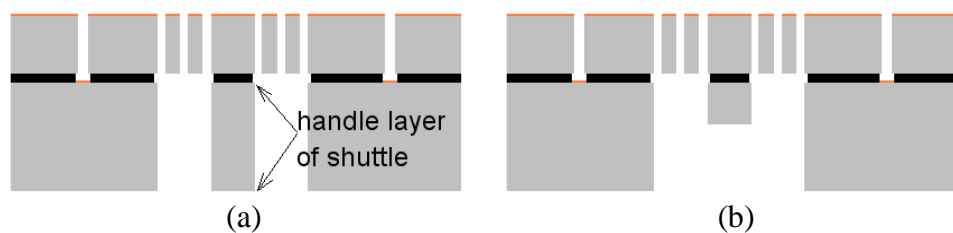


Figure 6.1: Schematics of (a) not etching the handle layer of the shuttles and (b) partially etching.

A controllable clamping mechanism is highly desirable to address the above issue of specimen failure during device handling. For example, the actuator and force sensor could be clamped during the device handling, and be released during testing. In addition,

a clamping mechanism for gripping individual NWs in the MEMS device, replacing the commonly used FEBID/FIBID, will be an interesting work in the future.

6.2.2 Alternative specimen alignments methods

To further prompt tensile testing at the nanoscale, a major development in the specimen preparation procedure is necessary, i.e. specimen alignment and firm fixation onto the testing device. The *in-situ* nanomanipulation technique is tedious, which usually takes two to three hours to mount a single NW on the MEMS device for an experienced operator. A faster specimen alignment method would be helpful to increase the testing throughput. The carbonaceous material deposited in the specimen during *in-situ* nanomanipulation might also be avoided. Electrophoresis alignment could be used for this purpose. However, the architecture of tensile stages has to be adapted to the aqueous environment, and whether the aligned NW will survive from the device handling is still a matter of concern.

6.2.3 Integration of a piezo-actuator into silicon based MEMS

Piezo-actuator has high energy density and could output large force, which is very attractive for application in a nanotensile stage. However, the force sensing of nano-Newton level is difficult to achieve with piezoelectric material based sensors (owing to the challenges of precise structuring of piezoelectric materials), and especially difficult for static measurements that is the case of quasi-static tensile testing. Integrating a piezo-actuator with a Si-based micro force sensor on a Si wafer will be a very interesting subject. The main challenges here might include micro-fabrication of piezoelectric materials, displacement amplification mechanism for the piezo-actuator, and maintaining a nearly pure in-plane force/displacement output from the actuator.

6.2.4 Micro force sensor with tunable stiffness

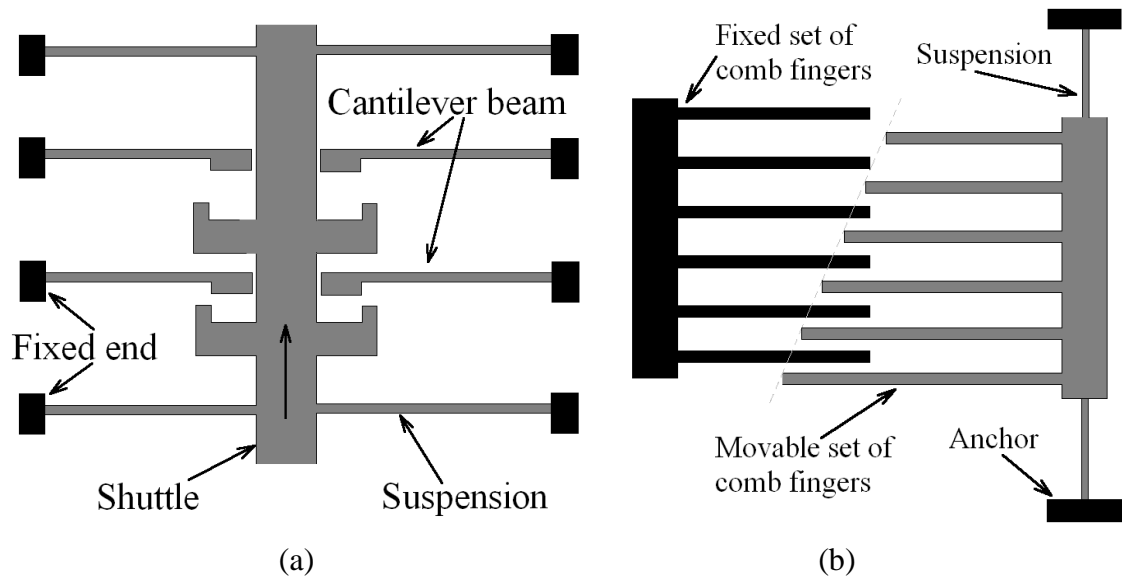


Figure 6.2 Schematics of methods for stiffness switching: (a) mechanical way [Clemens, et al., 2006] and (b) electrical way [Lee et al., 1998].

As discussed in Chapter 2, force sensors with different stiffness have to be designed for testing specimens of different stiffness. Four types of tensile stages were developed in this thesis to meet this requirement. A force sensor with tunable stiffness is promising to address this issue and enables testing many different samples with one device. The tunable stiffness of micro sensors could be achieved in a mechanical way, e.g. by engaging or disengaging several flexures [Clemens, et al., 2006] that are arranged in parallel in the loading direction, as shown in figure 6.2(a). This could also be achieved in an electrical way, e.g. by using a comb-drive actuator with triangular comb fingers as reported in [Lee et al., 1998], as shown in figure 6.2(b). The key requirement here is that the linearity of the force sensor should be ensured during the stiffness tuning.

This page intentionally left blank

Appendix A

Effective mass of a double clamped beam

This appendix shows derivation of the effective mass of a double clamped beam for the resonance analysis (see [Section 4.1](#)). [Figure A.1](#) is a schematic of a guided-end cantilever, i.e. the half of a double clamped beam.

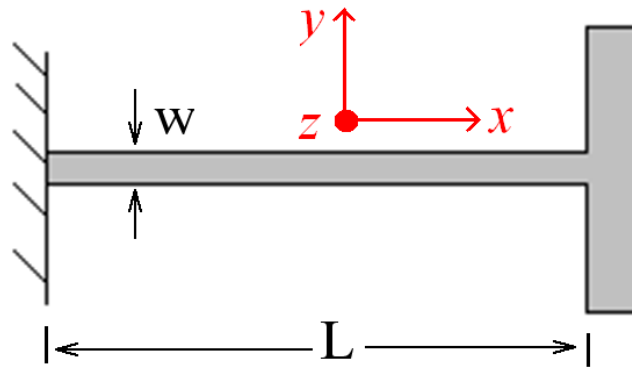


[Figure A.1](#): Schematic of a guided-end cantilever (not to scale).

Assuming that $(KE)_{\max}$ and $(PE)_{\max}$ are the maximum kinetic energy and the maximum potential energy during a vibration cycle, respectively, according to Rayleigh's energy method [[Weaver et al., 1990](#)],

$$(KE)_{\max} = (PE)_{\max} . \tag{A.1}$$

Since

$$v_s = \omega Y_0 , \tag{A.2}$$

We can get

$$\begin{aligned}
(KE)_{\max} &= \frac{1}{2} v_s^2 M_s + \frac{1}{2} \int v_b^2 dM_b = \frac{1}{2} (\omega Y_0)^2 M_s + \frac{1}{2} \int [\omega Y(x)]^2 dM_b \\
&= \frac{1}{2} (\omega Y_0)^2 M_s + \frac{1}{2} \frac{M_b}{L} \int_0^L [\omega Y(x)]^2 dx, \tag{A.3}
\end{aligned}$$

where v_s , v_b and M_s , M_b are the maximum velocity and mass of the shuttle and the beam, respectively. Y_0 is the maximum deflection of the cantilever end, and ω is the angular velocity of the cantilever.

The velocity profile of the guided-end cantilever beam is proportional to the mode shape at the maximum displacement. The mode shape is taken as the static displacement curve under a static load, which can be expressed as [Young et al., 2001]

$$Y(x) = \frac{FL}{12EI} x^2 \left(3 - 2 \frac{x}{L}\right) \quad (0 \leq x \leq L). \tag{A.4}$$

One of the boundary conditions is $Y(L) = Y_0 = \frac{FL^3}{12EI}$, we can get

$$EI = \frac{FL^3}{12Y_0} \tag{A.5}$$

$$Y(x) = Y_0 \left(\frac{x}{L}\right)^2 \left(3 - 2 \frac{x}{L}\right). \tag{A.6}$$

Therefore, equation A.3 can be expressed as

$$(KE)_{\max} = \frac{1}{2} \omega^2 Y_0^2 M_s + \frac{1}{2} \omega^2 Y_0^2 \frac{M_b}{L} \int_0^L \left(\frac{x}{L}\right)^4 \left(3 - 2 \frac{x}{L}\right)^2 dx = \frac{1}{2} \omega^2 Y_0^2 M_s + \frac{13}{70} \omega^2 Y_0^2 M_b. \tag{A.7}$$

In addition

$$(PE)_{\max} = \int_0^{Y_0} k y dy = \frac{1}{2} k Y_0^2, \tag{A.8}$$

Combing equations A.1, A.7 and A.8, we obtain

$$k = \omega^2 \left(M_s + \frac{13}{35} M_b\right). \tag{A.9}$$

Therefore,

$$M_{\text{eff}} = M_s + 13M_b / 35. \tag{A.10}$$

Appendix B

Verification of doping in SiNWs by electron beam induced current imaging

This appendix presents the experimental investigation of doping in SiNWs by electron beam induced current (EBIC) imaging. When a SiNW and the grown silicon substrate are of different doping (doping concentration or type), a built-in electrical field could be formed at the SiNW-substrate interface that is possibly detected by the EBIC imaging. This work was carried out in close collaboration with Dr Silke Christiansen's group (Dr. Thomas Stelzner and Björn Eisenhauer) at Institute of Photonic Technology (IPHT), Jena, Germany. The measurement results validate the successful doping of SiNWs, either by a chemical vapor deposition (CVD) or a pulsed laser deposition (PLD) during the VLS growth of SiNWs, which are crucial for developing SiNWs based solar cells and transistors.

B.1 Principle of EBIC imaging

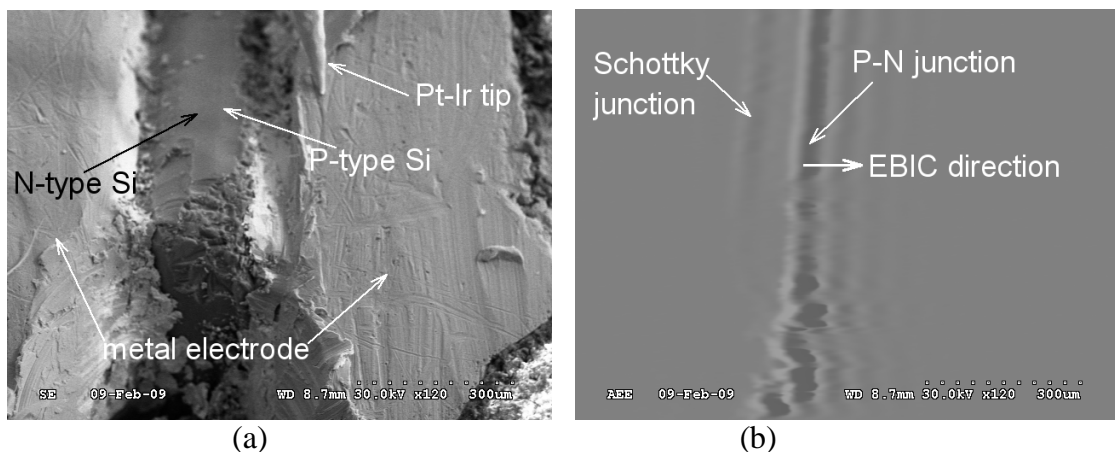


Figure B.1: (a) SE image of a P-N diode (the package was stripped), and (b) corresponding EBIC image of the diode.

EBIC imaging technique has been studied since about 50 years ago and is now widely used in the semiconductor industry and in material research community to locate p-n junctions and characterize various failure modes in different material systems [Leamy, 1982]. When an electron beam is incident on a semiconductor specimen, electron-hole pairs are created within the specimen by excitation of crystal electrons across the band-gap. Assuming that the specimen is not externally biased and has no internal electrical field, these excited carriers diffuse randomly and recombine eventually. No net current can be measured if the two terminals of the specimen are connected through an ammeter. However, in the presence of an (external or internal) electrical field, these carriers depart from purely random motions and constitute a current that may be measured in an external circuit. Since a SEM is a convenient source of e-beam, most EBIC techniques are performed using a SEM. To create an EBIC image, an e-beam is swept across the sample and the output current of the device is measured and displayed in the form of a synchronal video signal. The different gray levels at each pixel in the EBIC image indicate the magnitude and flowing direction of the induced current there, as shown in figure B.1(b). Superimposing the EBIC image with the SE image (see figure B.1a) permits location of the built-in electric field within the specimen.

B.2 Doping of SiNWs

Silicon nanowires (NWs) have attracted a great deal of interest in recent years due to their promising applications in nanoelectronics, biological sensing, and nano electromechanical system (NEMS) [Lu et al., 2006B]. Controllable doping in Si NWs is crucial for realizing Si NWs based solar cells and transistors, which has thus motivated considerable research efforts on this topic [Peng et al., 2005; Sivakov et al., 2009; Stelzner et al., 2008; Fukata et al., 2008; Cui et al., 2000]. Doping can be realized during the gas phase deposition process by adding dopants to the gas mixture in use for the NW growth. By changing the dopant source during the VLS process, various junctions have been successfully fabricated within a single SiNW, such as p-n and p-i-n SiNWs along the axial [Kempa et al., 2008] and coaxial [Tian et al., 2007] directions. High doping levels are required for fast response in small electronic devices, but the conventional CVD technique is reported to be limited in the realization of high doping levels as a

result of the VLS growth process making use of a gold droplet to catalyze SiNWs growth at growth temperatures, where unwanted gas phase decomposition of the dopant containing gas can take place [Zhang et al., 2010]. These catalyst droplets are liquid during growth at the eutectic gold silicon composition and show in addition a low solubility of dopants. The use of physical vapour deposition (PVD) for NWs growth could solve parts of the doping issue as there is no decomposition reaction. The synthesis processes of two types of doped SiNWs are presented in the following.

B.2.1 SiNWs doped by CVD during the VLS growth

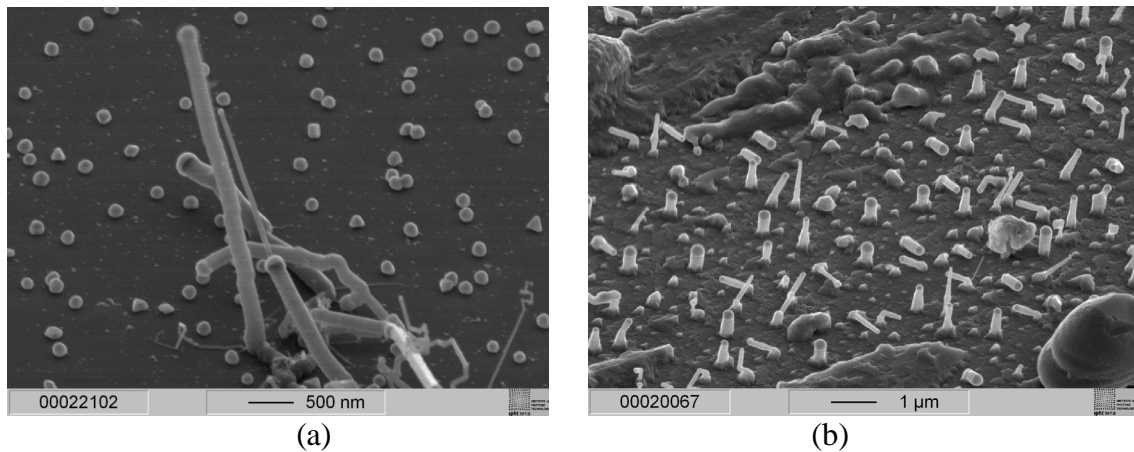


Figure B.2: HRSEM images of (a) SiNWs (TS383) doped by CVD during the VLS growth and (b) SiNWs (LW240) doped by PLD during the VLS growth. Note that the rough substrate surface in (b) renders challenges for contacting individual SiNWs in EBIC experiments.

Diameter controlled SiNWs were produced using gold colloids of 150 nm diameter (British Biocell International) [Stelzner et al., 2010]. The Au nanoparticles were immobilized on Si (111) substrates silylated using (3-aminopropyl) triethoxysilane (APTES). The thin silane film terminated with positively charged amino groups electrostatically attracted the negatively charged gold colloids in aqueous solution. The AuNPs immobilized on the substrate could then act as seeds for the VLS NW growth in a CVD reactor. The samples were inserted into a CVD reactor and annealed under a high vacuum at ~ 300 °C for 30 min to remove contamination followed by an annealing at ~ 580 °C for 10 min to improve the contact of the nanoparticles with the underlying

substrate. The temperature was then reduced to ~ 510 °C, and SiNWs were grown at a pressure of 2 mbar using the following gas flow rates:

TS383: 10 sccm Ar and 5 sccm silane for 5 min followed by 20 sccm Ar, 4 sccm silane, and 0.1 sccm diborane (100 ppm in He) for 20 min. The substrate is phosphorous doped Si (111) die (0.1-0.6 Ωcm). [Figure B.2\(a\)](#) shows a HRSEM image of these SiNWs.

TS387: 10 sccm Ar and 5 sccm silane for 5 min followed by 20 sccm Ar, 4 sccm silane, and 0.1 sccm phosphine (100 ppm in He) for 10 min. The grown substrate is boron doped Si (111) die (0.1-0.2 Ωcm).

B.2.2 SiNWs doped by PLD during the VLS growth

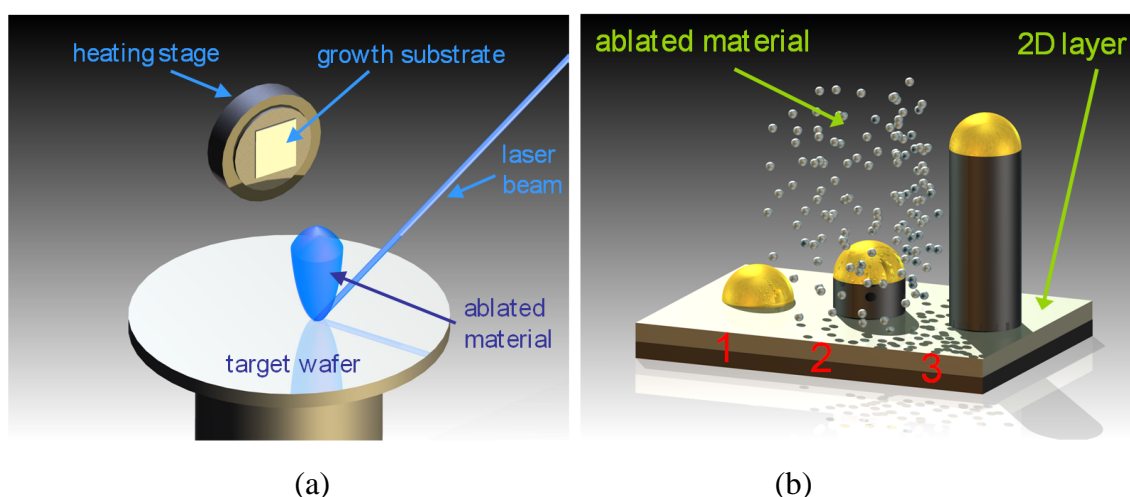


Figure B.3: Schematics of (a) the growth setup inside the vacuum chamber and (b) growth process at substrate: step 1: formation of droplets, step 2: incorporation of growth material, and step 3: supersaturation of eutectic droplet and growth of nanowires.

PLD was used to grow highly doped SiNWs for the reason that the stoichiometry of the target material equals the stoichiometry of the ablated target material and thus the doping level of the growth species can easily be controlled by the choice of the ablated target [[Zhang et al., 2010](#)].

The growth of SiNWs by PLD was performed under high vacuum conditions (10^{-6} mbar) in a Leybold L560s high vacuum chamber. The growth setup inside this chamber is schematically shown in [figure B.3\(a\)](#) and (b). A pulsed KrF Excimer Laser (λ

Physik LPX 300CC) operated at a wavelength of 248 nm was used to ablate the target material that was mounted on a rotational stage. The irradiating fluence at the target was about 2 J/cm^2 , the pulse width was $\sim 20 \text{ ns}$. This resulted in a laser power of $\sim 100 \text{ mW/cm}^2$ during the pulses at the target. Ablation resulted in presence of the atoms in the gas phase for a short time. The ablated material formed a plasma plume and propagated towards the growth substrate, which was mounted on a heating stage perpendicular to the plume of ablated material to minimize the amount of droplets of molten material impinging on the substrate in accordance to an approach presented by Holzapfel et al. [1992]. At this site, material precipitated both on the surface of the substrate and on the eutectic droplets. Material was incorporated directly into the droplets as well as via a sidewall diffusion process [Dubrovskii et al., 2006]. The growth follows a VLS routine in means of supersaturation of the droplets as well as relaxation of the supersaturation at the interface between the liquid droplet and the solid crystal below.

Slices of highly doped Si (111) wafers were used as a growth substrate. The growth was catalyzed by gold droplets formed by sputtering a thin gold film ($\sim 2 \text{ nm}$ thickness) onto the substrate and annealing at high temperatures for 1 h. The growth experiments were carried out directly after the annealing step. The used substrate temperature for the samples used in this work was $800 \text{ }^\circ\text{C}$, the total number of laser pulses was ~ 250000 . The background pressure in the growth chamber was $4 \times 10^{-6} \text{ mbar}$ for the samples discussed here.

For both of the samples LW240 and LW269, a boron doped Si (111) wafer with a specific resistivity of $5\text{-}10 \text{ } \Omega\text{cm}$ (which equals a dopant concentration of $(1.5\text{-}3) \times 10^{15} \text{ cm}^{-3}$) was used as the growth substrate. The ablation targets were a boron doped Si (111) wafer with a specific resistivity of $0.001\text{-}0.009 \text{ } \Omega\text{cm}$ (which equals a dopant concentration of $(1\text{-}6) \times 10^{19} \text{ cm}^{-3}$) for LW240 and a phosphorous doped Si (111) wafer with a specific resistivity less than $0.005 \text{ } \Omega\text{cm}$ (which equals a dopant concentration of $< 1.2 \times 10^{19} \text{ cm}^{-3}$) for LW269. A HRSEM image of LW240 is shown in figure B.2(b).

B.3 Experimental results and discussion

B.3.1 Experimental setup

To measure EBIC signal, the two terminals of a specimen have to be connected through a low-impedance current amplifier. Since these SiNWs were grown on a Si substrate, the bottom contact could be easily formed by connecting a shielded metal wire to the Si substrate directly with silver paste. The top of an individual SiNW was contacted by an electrochemically etched PtIr tip [Hoffmann et al., 2009]. This PtIr tip was equipped on a three-axis piezoelectric nanomanipulator (Smaract, Oldenburg, Germany), and the sample substrate was fixed onto a x, y, z piezo stage (Physik Instrumente (PI), Karlsruhe, Germany) with a $50\ \mu\text{m}$ range and sub-nanometer resolution in such a way that the SiNWs had a titled angle of about 50° with respect to the primary e-beam. The coarse positioning of the PtIr tip toward SiNWs was done with the nanomanipulator, and the fine positioning was achieved by moving the PI stage. The Smaract nanomanipulator can move in three directions of a Cartesian coordinate system independently, which is more convenient to use than a Kleindiek manipulator moving in a spherical coordinate system.

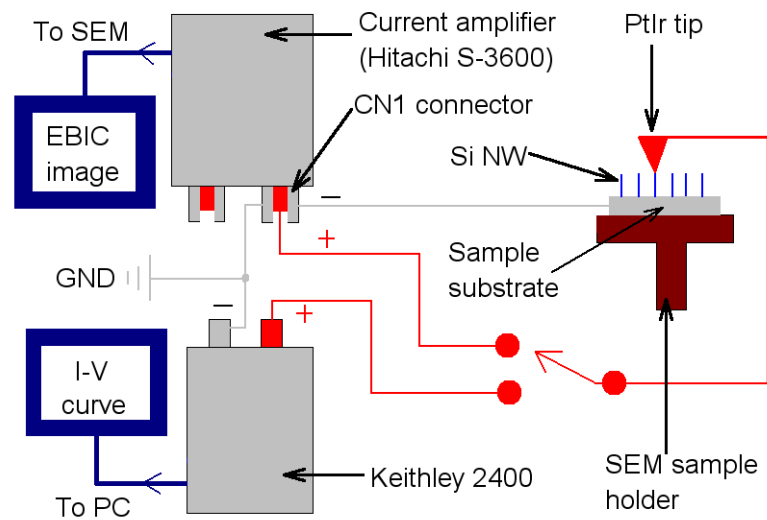


Figure B.4: Schematic of the electrical connections for EBIC and I-V measurement.

A Keithley 2400 SMU is used to perform the sweeping current-voltage (I-V) measurements when the PtIr tip is in contact with the top of SiNWs. The positive terminal of Keithley 2400 is connected to the PtIr tip, while the negative terminal is

connected to the sample substrate. The electrical connections for EBIC and I-V measurements are schematically shown in [figure B.4](#). Before testing, the gold droplets were removed by first dissolving the SiO₂ layer and then the gold particles, which was verified by HRSEM images. This step is to eliminate the possible hopping conductivity across gold agglomerates [[Bauer et al., 2007](#)] on the sidewall of the NWs.

B.3.2 Results and discussion

All of the synthesized samples have junctions at the SiNWs and the substrate interface, namely, TS383: *P-type NW on N-type substrate*; TS387: *N-type NW on P-type substrate*; LW240: *heavily doped P-type NW on lowly doped P-type substrate*; LW269: *heavily doped N-type NW on lowly doped P-type substrate*. In the follows, the EBIC images are always shown next to their SE images for locating the junctions. The corresponding I-V curves are also shown (if applicable) for the contact analysis. Note that the primary e-beam is blanked during I-V measurements to eliminate its influence to the electrical measurements.

A. TS383 and TS387

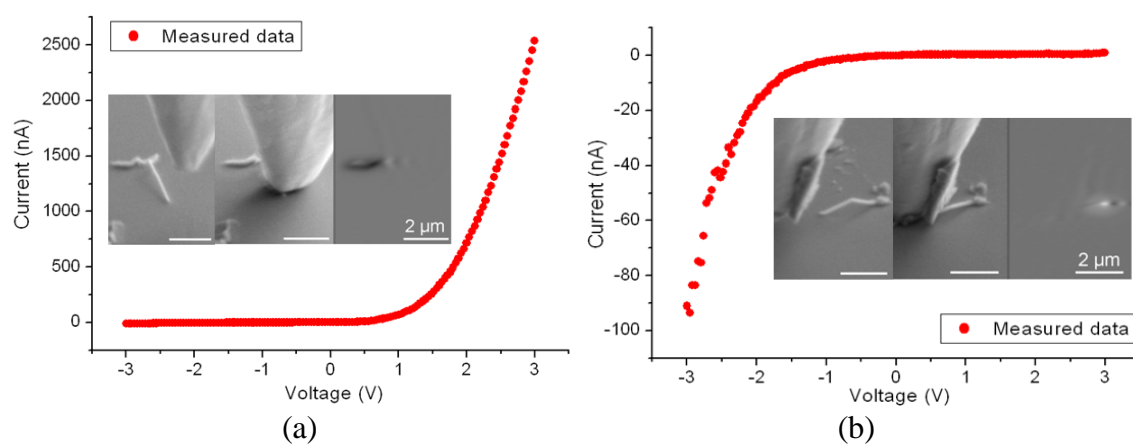


Figure B.5: SE and EBIC images and I-V characteristics measured on (a) TS383: boron doped SiNW grown on a N-type substrate and (b) TS387: PH₃ doped SiNW grown on a P-type substrate.

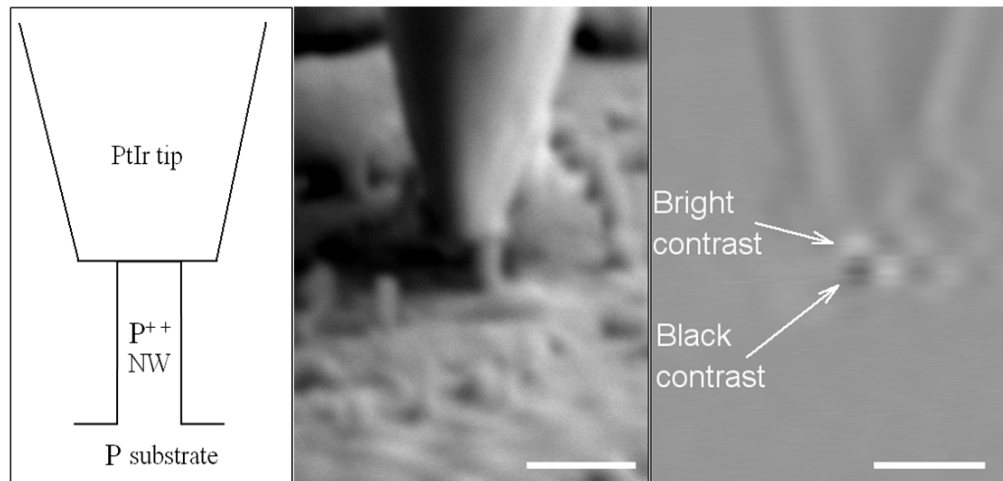
[Figure B.5\(a\)](#) shows the EBIC results on TS383 (*P-type NW on N-type substrate*). The dark spot seen in the right inset of [figure B.5\(a\)](#) indicates an EBIC flowing from the substrate to TS383 SiNW, and the junction is located at the NW-substrate interface. The

I-V curve shown in [figure B.5\(a\)](#) is rectifying with the forward direction from the PtIr tip to the NW. [Figure B.5\(b\)](#) shows the EBIC results on TS387 (*N-type NW on P-type substrate*). The bright spot seen in the right inset of [figure B.5\(b\)](#) indicates an EBIC flowing from TS383 SiNW to the substrate, and the junction is located at the NW-substrate interface. [Figure B.5\(b\)](#) shows the rectifying *I-V* curve with the reverse direction from the PtIr tip to the SiNW.

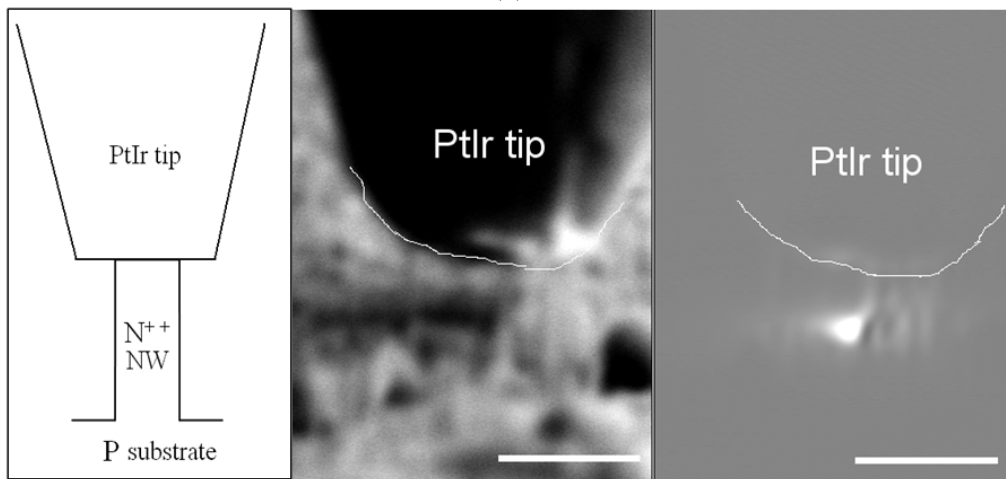
It can be seen that the threshold voltages in these curves are about 1.5 V, which is about 2 times of a normal P-N diode (~0.7 V). The most probable reason for this increase is a large series resistance connected to the P-N junction, which shares part of the applied voltage. This series resistance is likely to be caused by the high resistances of SiNWs and/or the contact resistances between the metal tips and the SiNWs. It should be noted that the EBIC signal can only be seen when certain amount of compressive force is applied to the contacting point of the SiNWs. We think the reason is that the compressive force removes the oxide layer and contamination layers on the SiNWs and the metal tips. Another possible reason is that the compressive force introduces phase transformation in SiNWs [[Jeong et al., 2003](#)]. When the compressive force becomes large, a Schottky junction at the metal tip and Si substrate interface could often be observed. Since a freestanding SiNW of large aspect ratio (length to diameter) is easily broken when compressed, short SiNWs are chosen in experiments.

B. LW240 and LW269

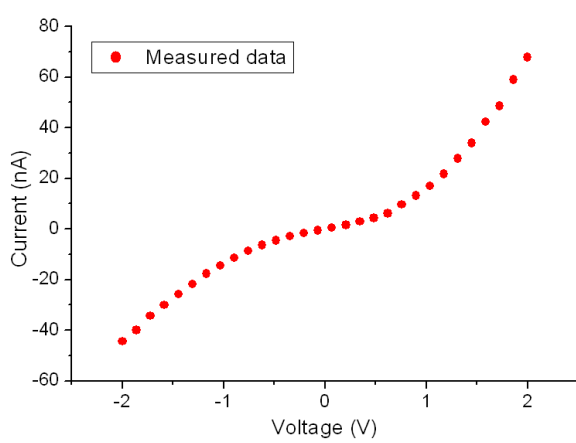
[Figure B.6\(a\)](#) and [\(b\)](#) shows the EBIC results on LW240 (*heavily doped P-type NW on lowly doped P-type substrate*). The dark spot seen in [figure B.6\(a\)](#) indicates an EBIC flowing from the substrate to LW240 SiNW, and the junction is located at the NW-substrate interface. A bright spot seen at the top of the dark spot in [figure B.6\(c\)](#) indicates an EBIC flowing from the PtIr tip to LW240 SiNW, and the junction is located at the NW-tip interface. The dark spot is caused by the built-in electric field of the P⁺⁺-P junction. The bright spot is caused by the Schottky junction at the tip-NW interface. [Figure B.6\(b\)](#) shows the measured *I-V* curve of the sample shown in [figure 4\(a\)](#), which could be explained from the two back-to-back connected diodes as discussed in [[Gao et al., 2009](#)].



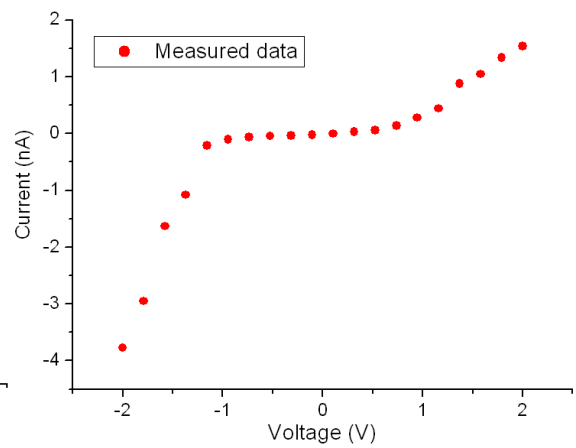
(a)



(b)



(c)



(d)

Figure B.6: EBIC testing results on LW240 and LW269. (a) SE and EBIC images of LW240. (b) SE and EBIC images of LW269. (c) I-V characteristic of LW240. (d) I-V characteristic of LW269. Scale bars: 1 μm .

Figure B.6(b) and (d) shows the EBIC results on LW269 (*heavily doped N-type NW on lowly doped P-type substrate*). The bright spot seen in figure B.6(b) indicates an EBIC flowing from the LW269 SiNW to the substrate, and the junction is located at the NW-substrate interface as expected. The I-V curve shown in figure B.6(d) is nearly rectifying with the reverse direction from the PtIr tip to the NW.

B.4 Conclusions

SiNWs were doped by CVD and PLD techniques during the VLS process, where junctions located at the SiNW and Si substrate interface were purposely implemented. By detecting the existences of these junctions with EBIC technique and two-point I-V measurements, the doping methodologies were successfully verified. This is the first time that PLD was experimentally demonstrated for doping SiNWs. This work is crucial for developing SiNWs based solar cells, transistors, and other advanced functional devices.

Bibliography

[Agrawal et al., 2008] Agrawal R, Peng B, Gdoutos E E and Espinosa H D 2008 Elasticity size effects in ZnO nanowires-A combined experimental-computational approach *Nano Lett.* **8** 3668–3674.

[Akhtar et al., 2008] Akhtar S, Usami K, Tsuchiya Y, Mizuta H and Oda S 2008 Size-dependent structural characterization of silicon nanowires *Jpn. J. Appl. Phys.* **47** 5053–5056.

[Allen, 2005] Allen J. J. 2005 *Micro Electro Mechanical System Design* (Boca Raton, FL: Taylor and Francis) pp. 429.

[Ando et al., 2001] Ando T, Shikida M and Sato K 2001 Tensile-mode fatigue of silicon film as structural materials for MEMS *Sensors and Actuators A.* **93** 70–75.

[Bao, 2005] Bao M 2005 *Analysis and Design Principles of MEMS Devices* (Amsterdam: Elsevier) pp. 213–245.

[Barsoukov et al., 2005] Barsoukov E and Macdonald J R 2005 *Impedance Spectroscopy: Theory, Experiment, and Applications* (Hoboken, New Jersey: John Wiley & Sons).

[Bauer et al., 2007] Bauer J, Fleischer F, Breitenstein O, Schubert L, Werner P, Gösele U and Zacharias M 2007 Electrical properties of nominally undoped silicon nanowires grown by molecular-beam epitaxy *Appl. Phys. Lett.* **90** 012105.

[Bell et al., 2005] Bell D J, Lu T J and Spearing S M 2005 MEMS actuators and sensors: observations on their performance and selection for purpose *J. Micromech. Microeng.* **15** S153–S164.

[Bertz et al., 2002] Bertz A, Kuchler M, Knofler Rand Gessner Th 2002 A novel high aspect ratio technology for MEMS fabrication using standard silicon wafers *Sensors and Actuators A* **97-98** 691–701.

[Boer et al., 2000] de Boer M J, Tjerkstra R W, Berenschot J W, Jansen H V, Burger G J, Gardeniers J G E, Elwenspoek M and van den Berg A 2000 Micromachining of buried micro channels in silicon *J. Microelectromech. Syst.* **9** 94–103.

[Boser, 1997] Boser B E 1997 Electronics for micromachined inertial Sensors *Proc. Transducers 1997* pp. 1169–1172.

- [[Brosnihan et al., 1997](#)] Brosnihan T J, Bustillo J M, Pisano A P and Howe R T 1997 Embedded interconnect and electrical isolation for high-aspect-ratio, SOI inertial instruments *Proc. Transducers 1997* pp. 637–640.
- [[Chen et al., 2008](#)] Chen C, Wu C, Chou C and Yen T 2008 Morphological control of single-crystalline silicon nanowire arrays near room temperature *Adv. Mater.* **20** 3811–3815.
- [[Clemens, et al., 2006](#)] Clemens M-F, Gouda S D, Kim S and Kim S-G 2006 A nanoscanning platform for bio-engineering: an in-plane probe with switchable stiffness *Nanotechnology* **7** S69–S76.
- [[Courtney, 2000](#)] Courtney T H 2000 *Mechanical Behavior of Materials* (Boston: McGraw–Hill).
- [[Cui et al., 2000](#)] Cui Y, Duan X, Hu J and Lieber C M 2000 Doping and electrical transport in silicon nanowires *J. Phys. Chem. B* **104** 5213–5216.
- [[Despont et al., 1993](#)] Despont M, Racine G A, Renaud P and de Rooij N F 1993 New design of micromachined capacitive force sensor *J. Micromech. Microeng.* **3** 239–242.
- [[de Lorenzo et al., 1997](#)] De Lorenzo A, Andreoli A, Matthie J and Withers P 1997 Predicting body cell mass with bioimpedance by using theoretical methods: A technological review *Journal of Applied Physiology* **82** 1542–1558.
- [[Diao et al., 2004](#)] Gall K, Diao J and Dunn M L 2004 The strength of gold nanowires *Nano Lett.* **4** 2431–2436.
- [[Ding et al., 2006](#)] Ding W, Calabri L, Chen X, Kohlhaas K M and Ruoff R S 2006 Mechanics of crystalline boron nanowires *Composites Science and Technology* **66** 1112–1124.
- [[Driehuisen et al., 1997](#)] van Driehuisen B P, Maluf N I, Opris I E and Kovacs G T A 1997 Force-balanced accelerometer with mG resolution, fabricated using silicon fusion bonding and deep reactive ion etching *Proc. Transducers 1997* pp. 1229–1230.
- [[Dubrovskii et al., 2006](#)] Dubrovskii V G, Sibirev N V, Cirilin G E, Harmand J C and Ustinov V M 2006 Theoretical analysis of the vapor-liquid-solid mechanism of nanowire growth during molecular beam epitaxy *Phys. Rev. E* **73** 021603.
- [[Duc et al., 2006](#)] Duc T C, Creemer J F and Sarro P M 2006 Lateral nano-Newton force-sensing piezoresistive cantilever for microparticle handling *J. Micromech. Microeng.* **16** S102–106.
- [[Elata et al., 2007](#)] Elata D and Leus V 2005 How slender can comb-drive fingers be? *J. Micromech. Microeng.* **15** 1055–1059.

- [Espinosa et al., 2007] Espinosa H D, Zhu Y and Moldovan N 2007 Design and operation of a MEMS-based material testing system for nanomechanical characterization. *J. Microelectromech. Syst.* **16** 1219–1231.
- [Fedder, 1994] Fedder G K 1994 Simulation of Microelectromechanical Systems *Ph.D. dissertation, University of California, Berkeley.*
- [Frisch-Fay, 1962] Frisch-Fay R 1962 *Flexible Bars* (London, U.K.: Butterworth) pp. 83–90.
- [Friedli et al., 2009] Friedli V, Utke I, Mølhave K and Michler J 2009 Dose and energy dependence of mechanical properties of focused electron beam induced pillar deposits from $\text{Cu}(\text{C}_5\text{HF}_6\text{O}_2)_2$ *Nanotechnology* **20** 385304.
- [Fujiwara et al., 2001] Fujiwara M, Oki E, Hamada M, Tanimoto Y, Mukouda I and Shimomura Y 2001 Magnetic orientation and magnetic properties of a single carbon nanotube *J Phys Chem A* **105** 4383–4386.
- [Fukuda et al., 2003] Fukuda T, Arai F and Dong L 2003 Assembly of nanodevices with carbon nanotubes through nanorobotic manipulations *Proc. IEEE* **91** 1803–1818.
- [Fukata et al., 2008] Fukata N, Matsushita S, Okada N, Chen J, Sekiguchi T, Uchida N and Murakami K 2008 Impurity doping in silicon nanowires synthesized by laser ablation *Appl Phys A.* **93** 589–592.
- [Gabrielson 1993] Gabrielson T B 1993 Mechanical-thermal noise in micromachined acoustic and vibration sensors *IEEE Trans. Electron Devices* **40** 903–909.
- [Gao et al., 2009] Gao Z, Zhou J, Gu Y, Fei P, Hao Y, Bao G and Wang Z L 2009 Effects of piezoelectric potential on the transport characteristics of metal-ZnO nanowire-metal field effect transistor *J. Appl. Phys.* **105** 113707.
- [Gerberich et al., 2009] Gerberich W W, Michler J, Mook W M, Ghisleni R, Östlund F, Stauffer D D and Ballarini R 2009 Scale effects for strength, ductility, and toughness in “brittle” materials *J. Mater. Res.* **24** 898–906.
- [Gilles et al., 2008] Gilles J P, Megherbi S, Raynauda G, Parrain F, Mathias H, Leroux X and Bosseboeuf A 2008 Scanning electron microscopy for vacuum quality factor measurement of small-size MEMS resonators *Sensors Actuators A* **145-146** 187–193.
- [Goldstein et al., 2007] Goldstein J, Newbury D E, Joy D C, Lyman C E, Echlin P, Lifshin E, Sawyer L C and Michael J R 2007 *Scanning Electron Microscopy and X-ray Microanalysis* (New York : Springer).
- [Gordon et al., 2009] Gordon M J, Baron T, Dhalluin F, Gentile P and Ferret P 2009

Size effects in mechanical deformation and fracture of cantilevered silicon nanowires
Nano Lett. **9** 525–529.

[[Han et al., 2006](#)] Han J H and Saif M T A 2006 In situ microtensile stage for electromechanical characterization of nanoscale freestanding films *Rev Sci Instrum* **77** 045102.

[[Haque et al., 2001](#)] Haque M A and Saif M T A 2001 Microscale materials testing using MEMS actuators *J. Microelectromech. Syst.* **10** 146–152.

[[Haque et al., 2005](#)] Haque M A and Saif M T A 2005 Thermo-mechanical properties of nano-scale freestanding aluminum films *Thin solid films* **484** 364–368.

[[Haque et al., 2006](#)] Haque M A and Saif M T A 2006 A review of MEMS-based microscale and nanoscale tensile and bending testing *Exp. Mech.* **43** 248–255.

[[Hazra et al., 2009](#)] Hazra S S, Baker M S, Beuth J L and de Boer M P 2009 Demonstration of an in situ on-chip tensile tester *J. Micromech. Microeng.* **19** 082001.

[[He et al., 2006](#)] He R and Yang P 2006 Giant piezoresistance effect in silicon nanowires *Nature Nanotech.* **1** 42–46.

[[He et al., 2008](#)] He J and Lilley C M 2008 Surface effect on the elastic behavior of static bending nanowires. *Nano Lett.* **8** 1798–1802.

[[Hoffmann et al., 2006](#)] Hoffmann S, Utke I, Moser B, Michler J, Christiansen S, Schmidt V, Senz S, Werner P, Gosele U and Ballif C 2006 Measurement of the bending strength of vapor-liquid-solid grown silicon nanowires *Nano Lett.* **6** 622–625.

[[Hoffmann et al., 2007](#)] Hoffmann S, Östlund F, Michler J, Fan H J, Zacharias M, Christiansen S and Ballif C 2007 Fracture strength and Young's modulus of ZnO nanowires *Nanotechnology* **18** 205503.

[[Hoffmann et al., 2009](#)] Hoffmann S, Bauer J, Ronning C, Stelzner Th, Michler J, Ballif C, Sivakov V and Christiansen S 2009 Axial p-n junctions realized in silicon nanowires by ion implantation *Nano Lett.* **9** 1341–1344.

[[Holzapfel et al., 1992](#)] Holzapfel B, Roas B, Schultz L, Bauer P and Saemann-Ischenko G 1992 Off-axis laser deposition of $\text{YBa}_2\text{Cu}_3\text{O}_{7-\delta}$ thin films *Appl. Phys. Lett.* **61** 3178.

[[Hooge 1969](#)] Hooge F N 1969 1/f noise is no surface effect *Phys. Lett. A* **29** 139–140.

[[Huang et al., 2001](#)] Huang Y, Duan X, Wei Q and Lieber C M 2001 Directed assembly of one-dimensional nanostructures into functional networks *Science* **291** 630–633.

- [Huang et al., 2002] Huang C, Christophorou C, Najafi, K, Naguib A and Nagib H M 2002 An electrostatic microactuator system for application in high-speed jets *J. Microelectromech. Syst.* **11** 222–235
- [Ishihara et al., 1999] Ishihara K, Yung C, Ayon A A and Schmidt M A 1999 An inertial sensor technology using DRIE and wafer bonding with interconnecting capability *J. Microelectromech. Syst.* **8** 403–408.
- [Jaecklin et al., 1992] Jaecklin V P, Linder C, de Rooij N F and Moret J M 1992 Micromechanical comb actuators with low driving voltage *J. Micromech. Microeng.* **2** 250–255.
- [Jeong et al., 2003] Jeong S, Oh S, Park S and Lee H 2003 Phase transformation of single crystalline silicon by scratching *Jpn. J. Appl. Phys.* **42** 2773–2774.
- [Jing et al., 2006] Jing G Y, Duan H L, Sun X M, Zhang Z S, Xu J, Li Y D, Wang J X and Yu D P 2006 Surface effects on elastic properties of silver nanowires: Contact atomic-force microscopy *Phys. Rev. B* **73** 235409.
- [Johnson et al., 1995] Johnson W A and Warne L K 1995 Electrophysics of micromechanical comb actuators *J. Microelectromech. Syst.* **4** 49–59.
- [Johnson et al., 2000] Johnson G T, Jones P T, Howe R T 2000 Materials characterization for MEMS: a comparison of uniaxial and bending tests *Proc. SPIE* **3874** 94–101.
- [Karimpoor et al., 2006] Karimpoor A A and Erb U 2006 Mechanical properties of nanocrystalline cobalt *Phys. stat. sol. (a)* **203** 1265–1270.
- [Kempa et al., 2008] Kempa T J, Tian B, Kim D R, Hu J, Zheng X and Lieber C M 2008 Single and tandem axial p-i-n nanowire photovoltaic devices *Nano Lett.* **8** 3456–3460.
- [Khanna et al., 2001] Khanna R, Zhang X, Protz J and Ayon A A 2001 Microfabrication protocols for deep reactive ion etching and wafer-level bonding *Sensors (Peterborough, NH)* **18** 51–60.
- [Kiuchi et al., 2007] Kiuchi M, Matsui S and Isono Y 2007 Mechanical characteristics of FIB deposited carbon nanowires using an electrostatic actuated nano tensile testing device *J. Microelectromech. Syst.* **16** 191–201.
- [Kraft et al., 2001] Kraft O and Volkert C A 2001 Mechanical testing of thin films and small structures *Advanced Engineering Materials* **3** 99–110.
- [Krijnen et al., 2003] Krijnen G, Haanstra R, Potters E, Berenschot J W, von Harrach S and Elwenspoek M 2003 Protruding microgripper with force amplification and parallel jaw motion for in-situ sample manipulation in SEM and FIB-machines *Proc. Transducers* 2003 pp. 268–271.

- [Kovacik, 1999] Kovacik J 1999 Correlation between Young's modulus and porosity in porous materials *J. Mater.Sci. Lett.* **18** 1007–1010.
- [Kumar et al., 2003] Kumar K S, Van Swygenhoven H and Suresh S 2003 Mechanical behavior of nanocrystalline metals and alloys *Acta Materialia* **51** 5743–5774.
- [Leamy, 1982] Leamy H J 1982 Charge collection scanning electron microscopy *J. Appl. Phys.* **53** R51–80.
- [Lee et al., 1998] Lee K B and Cho Y-H 1998 A triangular electrostatic comb array for micromechanical resonant frequency tuning *Sens. Actuators. A* **70** 112–117.
- [Legtenberg et al., 1996] Legtenberg R, Groeneveld A W and Elwenspoek M 1996 Comb-drive actuators for large displacements *J. Micromech. Microeng.* **6** 320–329.
- [Li et al., 2003] Li X, Gao H, Murphy C J and Caswell K K 2003 Nanoindentation of silver nanowires *Nano Lett.* **3** 1495–1498.
- [Li et al., 2005] Li X, Wang X, Chang W, Chao Y and Chang M 2005 Effect of tensile offset angles on micro/nanoscale tensile testing *Rev Sci Instrum* **76** 033904.
- [Li et al., 2007] Li Q, Koo S-M, Richter C A, Edelstein M D, Bonevich J E, Kopanski J J, Suehle J S and Vogel E M 2007 Precise alignment of single nanowires and fabrication of nanoelectromechanical switch and other test structures *IEEE Trans. Nanotechnology* **6** 256–262.
- [Liu et al., 2006] Liu K H, Wang W L, Xu Z, Liao L, Bai X D and Wang E G 2006 In situ probing mechanical properties of individual tungsten oxide nanowires directly grown on tungsten tips inside transmission electron microscope *Appl. Phys. Lett.* **89** 221908.
- [Lu et al., 2005] Lu S, Chung J and Ruoff R S 2005 Controlled deposition of nanotubes on opposing electrodes *Nanotechnology* **16** 1765–1770.
- [Lu et al., 2006] Lu S, Guo Z, Ding W and Ruoff R S 2006 In situ mechanical testing of templated carbon nanotubes *Rev Sci Instrum* **77** 125101.
- [Lu et al., 2006B] Lu W and Lieber C M 2006 Semiconductor nanowires *J. Phys. D: Appl. Phys.* **39** R387–R406.
- [Maluf, 2004] Maluf N 2004 *An Introduction to Microelectromechanical Systems Engineering* (Boston: Artech House) pp. 13–18.
- [Meirovich, 1986] Meirovich L 1986 *Element of Vibration Analysis* (McGraw-Hill: NewYork) pp. 235.

- [[McDowell et al., 2008](#)] McDowell M T, Leach A M and Gall K 2008 On the elastic modulus of metallic nanowires *Nano Lett.* **8** 3613–3618.
- [[Meyers et al., 2006](#)] Meyers M A, Mishra A and Benson D J 2006 Mechanical properties of nanocrystalline materials *Prog. Mater. Sci.* **51** 427–556.
- [[Michler et al., 2007](#)] Michler J, Wasmer K, Meier S, Östlund F and Leifer K 2007 Plastic deformation of gallium-arsenide micropillars under uniaxial compression at room temperature *Appl. Phys. Lett.* **90** 043123.
- [[Namazu et al., 2000](#)] Namazu T, Isono Y and Tanaka T 2000 Evaluation of size effect on mechanical properties of single crystal silicon by nanoscale bending test using AFM *J. Microelectromech. Syst.* **9** 450–459.
- [[Ni et al., 2006](#)] Ni H and Li X 2006 Young's modulus of ZnO nanobelts measured using atomic force microscopy and nanoindentation techniques *Nanotechnology* **17** 3591–3597.
- [[Nielson et al., 2006](#)] Nielson G N and Barbastathis G 2006 Dynamic pull-in of parallel-plate and torsional electrostatic MEMS actuators *J. Microelectromech. Syst.* **15** 811–821.
- [[Nyquist, 1928](#)] Nyquist H 1928 Thermal agitation of electric charge in conductors *Phys. Rev.* **32** 110–113.
- [[Östlund et al., 2009](#)] Östlund F, Rzepiejewska-Malyska K, Leifer K, Hale L M, Tang Y, Ballarini R, Gerberich W W and Michler J 2009 Brittle-to-ductile transition in uniaxial compression of silicon pillars at room temperature *Adv. Funct. Mater.* **19** 2439–2444.
- [[Overstolz et al., 2004](#)] Overstolz T, Clerc P A, Noell W, Zickar M and de Rooij N F 2004 A clean wafer-scale chip-release process without dicing based on vapor phase etching *Proc. IEEE MEMS 2004* pp. 717–720.
- [[Peng et al., 2002](#)] Peng K Q, Yan Y J, Gao S P and Zhu J 2002 Synthesis of large-area silicon nanowire arrays via self-assembling nanoelectrochemistry *Adv. Mater.* **14** 1164–1167.
- [[Peng et al., 2005](#)] Peng K Q, Xu Y, Wu Y, Yan Y, Lee S T and Zhu J 2005 Aligned single-crystalline Si nanowire arrays for photovoltaic applications *Small* **1** 1062.
- [[Philippe et al., 2007](#)] Philippe L, Kacem N and Michler J 2007 Electrochemical deposition of metals inside high aspect ratio nanoelectrode array: analytical current expression and multidimensional kinetic model for Cobalt nanostructure synthesis *J. Phys. Chem. C* **111** 5229–5235.
- [[Philippe et al., 2009](#)] Philippe L, Cousin B, Wang Z, Zhang D and Michler J 2010 Mass density of individual cobalt nanowires *Appl. Phys. Lett.* **96** 051903.

- [Prasanna et al., 2007] Prasanna S and Spearing S M 2007 Materials selection and design of microelectrothermal bimaterial actuators *J. Microelectromech. Syst.* **16** 248–259.
- [Prasanna et al., 2008] Prasanna S and Spearing S M 2008 Optimal materials selection for biomaterial piezoelectric microactuators *J. Microelectromech. Syst.* **17** 462–472.
- [Rangelow et al., 2003] Rangelow I W 2003 Critical tasks in high aspect ratio silicon dry etching for microelectromechanical systems *J. Vac. Sci. Technol. A* **21** 1550–1562.
- [Ryuichi et al., 1992] Ryuichi S and Ding Z 1992 Monte Carlo modelling of electron-solid interactions *Rep. Prog. Phys.* **55** 487–531.
- [Qu et al., 2007] Qu H and Xie H 2007 Process development for CMOS-MEMS sensors with robust electrically isolated bulk silicon microstructures *J. Microelectromech. Syst.* **16** 1152–1161.
- [Rouki et al., 2003] Rouki C, Westerberg L and the CHICSi development group 2003 Ultra-high vacuum compatibility measurements of materials for the CHICSi detector system *Physica Scripta*. **T104** 107–108.
- [Sakai et al., 1998] Sakai S, Tanimoto H and Mizubayashi H 1998 Mechanical behavior of high-density nanocrystalline gold prepared by gas deposition method *Acta Materialia* **47** 211–217.
- [Samuel et al., 2006] Samuel B A, Desai A V and Haque M A 2006 Design and modeling of a MEMS pico-Newton loading/sensing device *Sens. Actuators. A* **127** 155–162.
- [Samuel et al., 2007] Samuel B A, Haque M A, Yi B, Rajagopalan R and Foley H C. Mechanical testing of pyrolysed poly-furfuryl alcohol nanofibres *Nanotechnology* **18** 115704.
- [Sarajlic, 2006] Sarajlic E 2006 Electrostatic microactuators fabricated by vertical trench isolation technology *PhD Thesis, Univ. of Twente*.
- [Sehr et al., 2001] Sehr H, Brunnschweiler A, Evans A, Ensell G and Niblock T 2001 Fabrication and test of thermal vertical bimorph actuators for movement in the wafer plane *J. Micromech. Microeng.* **11** 311–318.
- [Seeger et al., 2003] Seeger J I, Boser B E 2003 Charge control of parallel-plate, electrostatic actuators and the tip-in instability *J. Microelectromech. Syst.* **12** 656–671.

- [Sivakov et al., 2009] Sivakov V, Andrae G, Gawlik A, Berger A, Plentz J, Falk F and Christiansen S 2009 Silicon nanowire-based solar cells on glass: synthesis, optical properties, and cell parameters *Nano Lett.* **9** 1549–1554.
- [Smith et al., 2000] Smith PA, Nordquist CD, Jackson TN, Mayer TS, Martin BR, Mbindyo J and Mallouk TE 2000 Electric-field assisted assembly and alignment of metallic nanowires *Appl. Phys. Lett.* **77** 1399–1401.
- [Soboyejo et al., 2007] Soboyejo W O and Srivatsan T S 2007 *Advanced Structural Materials: Properties, Design Optimization, and Applications* (Boca Raton: CRC) pp. 192–218.
- [Song et al., 2005] Song J, Wang X, Riedo E and Wang Z L 2005 Elastic property of vertically aligned nanowires *Nano Lett.* **5** 1954–1958.
- [Spencer et al., 1988] Spencer R R, Fleischer B M, Barth P W and Angell J B 1988 A theoretical study of transducer noise in piezoresistive and capacitive silicon pressure sensors *IEEE Trans. Electron Devices* **35** 1289–1297.
- [Stan et al., 2008] Stan G, Krylyuk S, Davydov A V, Vaudin M, Bendersky L A and Cook R F 2008 Surface effects on the elastic modulus of Te nanowires *Appl. Phys. Lett.* **92** 241908.
- [Stelzner et al., 2008] Stelzner Th, Pietsch M, Andrä G, Falk F, Ose E and Christiansen S 2008 Silicon nanowire-based solar cells *Nanotechnology* **19** 295203.
- [Stelzner et al., 2010] Stelzner Th, Sivakov V, Berger A, Hoffmann B, de Wolf S, Ballif C, Zhang D, Michler J and Christiansen S 2010 Structural, optical, and electrical properties of silicon nanowire solar cells *IEEE International NanoElectronics Conference (INEC)*, 3th-8th Jan. 2010, HongKong, China, oral presentation.
- [Stratakis et al., 2008] Stratakis E, Misra N, Spanakis E, Hwang D, Grigoropoulos C P, Fotakis C and Tzanetakis P 2008 Imaging dielectric properties of Si nanowire oxide with conductive atomic force microscopy complemented with femtosecond laser illumination *Nano Lett.* **8** 1949–1953.
- [Su, 2001] Su X.-P. S. 2001 Compliant leverage mechanism design for MEMS applications *Ph.D. dissertation, University of California, Berkeley.*
- [Sun et al., 2005] Sun Y, Fry S N, Potasek D P, Bell D J and Nelson B J 2005 Characterizing fruit fly flight behavior using a microforce sensor with a new comb-drive configuration *J. Microelectromech. Syst.* **14** 4–11.
- [Sun et al., 2008] Sun L, Wang J, Rong W, Li X and Bao H 2008 A silicon integrated micro nano-positioning XY-stage for nano-manipulation *J. Micromech. Microeng.* **18** 125004.

- [[Suster et al., 2006](#)] Suster M, Guo J, Chaimanonart N, Ko W H and Young D J 2006 A high-performance MEMS capacitive strain sensing system *J. Microelectromech. Syst.* **15** 1069–1077.
- [[Tang et al., 1989](#)] Tang W C, Nguyen T-C H and Howe R T 1989 Laterally driven polysilicon resonant microstructures *Sensors Actuators A* **20** 25–32.
- [[Tang, 1990](#)] Tang W C 1990 Electrostatic comb drive for resonant sensor and actuator applications *Ph.D. Thesis, University of California at Berkeley* pp. 50–57.
- [[Tang et al., 1992](#)] Tang W C, Lim M G and Howe R T 1992 Electrostatic comb drive levitation and control method *J. Microelectromech. Syst.* **1** 170–178.
- [[Taylor, 1997](#)] Taylor J R 1997 *An Introduction to Error Analysis: the Study of Uncertainties in Physical Measurements* (Sausalito, California: University Science Books) pp. 73–77.
- [[Thong, 1993](#)] Thong J T L 1993 *Electron Beam Testing Technology* (New York: Plenum) pp. 175–195.
- [[Tian et al., 2007](#)] Tian B, Zheng X, Kempa T J, Fang Y, Yu N, Yu G, Huang J and Lieber C M 2007 Coaxial silicon nanowires as solar cells and nanoelectronic power sources *Nature* **449** 885–890.
- [[Utke et al., 2000](#)] Utke I, Hoffmann P, Dwir B, Leifer K, Kapon E and Doppelt P 2000 Focused electron beam induced deposition of gold *J. Vac. Sci. Technol. B* **18** 3168–3171.
- [[Utke et al., 2002](#)] Utke I, Luisier A, Hoffmann P, Laub D and Buffat P A 2002 Focused-electron-beam-induced deposition of freestanding three-dimensional nanostructures of pure coalesced copper crystals *Appl. Phys. Lett.* **81** 3245–3247.
- [[Utke et al., 2008](#)] Utke I, Hoffmann P and Melngailis J 2008 Gas-assisted focused electron beam and ion beam processing and fabrication *J. Vac. Sci. Technol. B* **26** 1197–1276.
- [[Varghese et al., 2008](#)] Varghese B, Zhang Y, Dai L, Tan V B C, Lim C and Sow C 2008 Structure-mechanical property of individual cobalt oxide nanowires *Nano Lett.* **8** 3226–3232.
- [[Wang et al., 1999](#)] Wang Q-M, Du X-H, Xu B and Cross L E 1999 Electromechanical coupling and output efficiency of piezoelectric bending actuators *IEEE Transactions on Ultrasonics, Ferroelectrics and Frequency Control* **46** 638–646.
- [[Wang, 2006](#)] Wang Z L 2006 *Nanowires and Nanobelts: Materials, Properties and Devices* (Boston, MA: Kluwer Academic).

[Wang et al., 2007] Wang Z, Hu J, Suryavanshi A P, Yum K and Yu M-F 2007 Voltage generation from individual BaTiO₃ nanowires under periodic tensile mechanical load *Nano Lett.* **7** 2966–2969.

[Wang et al., 2008] Wang Z, Miao J, Tan C and Xu T 2008 Fabrication of piezoelectric MEMS devices—from thin film to bulk PZT wafer *J. Electroceram.* Available: doi:10.1007/s10832-008-9454-x.

[Weaver et al., 1990] Weaver W, Timoshenko S and Young D H 1990 *Vibration Problems in Engineering* (New York: Wiley-Interscience) pp. 24–39.

[Williams et al., 2002] Williams P A, Papadakis S J, Falvo M R, Patel A M, Sinclair M, Seeger A, Helser A, Taylor R M, Washburn S and Superfine R 2002 Controlled placement of an individual carbon nanotube onto a microelectromechanical structure *Appl. Phys. Lett.* **80** 2574–2576.

[Wu et al., 2004] Wu J, Feeder G K and Carley L R 2004 A low-noise low-offset capacitive sensing amplifier for a 50 $\mu\text{g}(\text{Hz})^{-1/2}$ monolithic CMOS MEMS accelerometer *IEEE J. Solid-State Circuits* **39** 722–730.

[Wu et al., 2006] Wu B, Heidelberg A, Boland J J, Sader J E, Sun X and Li Y 2006 Microstructure-hardened silver nanowires *Nano Lett.* **6** 468–472.

[Yamada et al., 1982] Yamada K, Nishihara M, Shimada S, Tanabe M, Shimazoe M and Matsuoka Y 1982 Nonlinearity of the piezoresistance effect of p-type silicon diffused layers *IEEE Tran. Electron Devices* **29** 71–77.

[Ye et al., 1998] Ye W, Mukherjee S, MacDonald N C 1998 Optimal shape design of an electrostatic comb drive in microelectromechanical systems *J. Microelectromech. Syst.* **7** 16–26.

[Yeh et al., 2000] Yeh J L A, Hui C Y and Tien N C 2000 Electrostatic model for an asymmetric comb drive *J. Microelectromech. Syst.* **9** 126–135.

[Young et al., 2001] Young W C and Budynas R 2001 *Roark's Formulas for Stress and Strain* (New York: McGraw-Hill).

[Yu et al., 2000] Yu M F, Lourie O, Dyer M J, Moloni K, Kelly T F and Ruoff R S 2000 The strength and breaking mechanism of multiwalled carbon nanotubes under tensile load *Science* **40** 637–640.

[Zhang et al., 2009a] Zhang D, Drissen W, Breguet J-M, Clavel R and Michler J 2009 A high-sensitivity and quasi-linear capacitive sensor for nanomechanical testing applications. *J. Micromech. Microeng.* **19** 075003.

[Zhang et al., 2009b] Zhang D, Breguet J-M, Clavel R, Phillippe L, Utke I and Michler J 2009 In situ tensile testing of individual Co nanowires inside a scanning electron microscope *Nanotechnology* **20** 365706.

[Zhang et al., 2009c] Zhang D, Breguet J-M, Clavel R, Sivakov V, Christiansen S and Michler J 2009 *In situ* electron microscopy mechanical testing of silicon nanowires using electrostatically actuated tensile stages, submitted to *J. Microelectromech. Syst.*

[Zhang et al., 2010] Zhang D, Eisenhauer B, Clavel R, Christiansen S and Michler J 2010 Electron beam induced current imaging of doped Si nanowires. In preparation.

[Zhu et al., 2005] Zhu Y and Espinosa H D 2005 An electromechanical material testing system for in situ electron microscopy and applications *Proc. Natl Acad. Sci.* **102** 14503.

[Zhu et al., 2006] Zhu Y, Corigliano A and Espinosa H D 2006 Thermal actuator for nanoscale *in situ* microscopy testing: design and characterization *J. Micromech. Microeng.* **16** 242–253.

[Zhou et al., 2007] Zhou W and Wang Z L 2007 *Scanning Microscopy for Nanotechnology: Techniques and Applications* (New York: Springer) pp. 192–224.

[Zhu et al., 2007] Zhu Y, Ke C-H and Espinosa H D 2007 Experimental techniques for the mechanical characterization of thin films and one-dimensional nanostructures *Exp. Mech.* **47** 7–24.

Curriculum Vitae

Personal Data

Name: Dongfeng ZHANG

Date of Birth: Aug., 1982

Place of Birth: Anhui, China

Nationality: Chinese

Education

2008 ~ present Laboratory for Mechanics of Materials and Nanostructures,
Swiss Federal Laboratories for Materials Testing and Research
PhD student.

2006 ~ 2008 Laboratory of Robotic System (**LSRO**), Institute of Microengineering,
Ecole Polytechnique Fédérale de Lausanne (**EPFL**), Switzerland
PhD student.

2004 ~ 2006 MEMS Lab, Center for Biomimetic Sensing and Control Research,
Institute of Intelligent Machines (**IIM**), Chinese Academy of Sciences (**CAS**)
MEng in microsensor and microsystem technology.

2003 ~ 2004 Department of Physics (1st phase of Master study),
University of Science and Technology of China (**USTC**), China.

1999 ~ 2003 College of Sciences,
Hefei University of Technology (**HFUT**), China
BEng in Electronic Science & Technique.

This page intentionally left blank

List of Patents and Publications

Patent

1. Issued Patent: Deyi Kong, **Dongfeng Zhang**, Tao Mei, Lin Ni, Zhengyong Zhang, Yongchun Tao, Jianhua Shan and Lei Sun. A magnetosensitive sensors array and its fabrication method. *Chinese patent number: ZL 2005 1 0040154.4.*
2. Issued Patent: Tao Mei, Jianhua Shan, Zhengyong Zhang, Lei Sun, Lin Ni, Shirong Chen, **Dongfeng Zhang**, Yongchun Tao, Deyi Kong and Qinghu Meng. Fabrication method of a flexible temperature sensors array. *Chinese patent number: ZL 2004 1 0065901.5.*

Peer reviewed journal paper

1. **Dongfeng Zhang**, Björn Eisenhawer, Reymond Clavel, Silke Christiansen and Johann Michler. Electron beam induced current imaging of doped Si nanowires. In preparation, 2010.
2. **Dongfeng Zhang**, Jean-Marc Breguet, Reymond Clavel, Vladimir Sivakov, Silke Christiansen and Johann Michler. *In situ* electron microscopy mechanical testing of silicon nanowires using electrostatically actuated tensile stages. Submitted to *J. Microelectromech. Syst.*, 2009.
3. **Dongfeng Zhang**, Jean-Marc Breguet, Reymond Clavel, Laetitia Phillippe, Ivo Utke and Johann Michler. *In situ* tensile testing of individual Co nanowires inside a scanning electron microscope. *Nanotechnology* 20 (2009) 365706.
4. **Dongfeng Zhang**, Walter Drissen, Jean-Marc Breguet, Reymond Clavel and Johann Michler. A high-sensitivity and quasi-linear capacitive sensor for nanomechanical testing applications. *J. Micromech. Microeng.* 19 (2009) 075003.
5. Laetitia Phillippe, Barbara Cousin, Zhao Wang, **Dongfeng Zhang** and Johann Michler. Mass density of individual cobalt nanowires. *Appl. Phys. Lett.* 96 (2010) 051903.

6. **Dongfeng Zhang**, Deyi Kong, Tao Mei and Yongchun Tao. Present status and prospect of miniaturized Ion Mobility Spectrometry. *Chinese Journal of Scientific Instrument* 27(2005) 199-204 (in Chinese).
7. Yongchun Tao, Deyi Kong, Tao Mei, Tao Zhang, Wei Lu and **Dongfeng Zhang**. Development of an explosive detector with a MEMS sensor array. *International Journal of Information Acquisition* 1(2004) 337-343.
8. Deyi Kong, Tao Mei, Yongchun Tao, **Dongfeng Zhang**, Wei Lu and Zhengyong Zhang. Research on a portable explosive detector based on MEMS technology. *China Mechanical Engineering* 16 (2005) 163-165 (in Chinese).

Conference paper, poster, and oral presentation

1. Thomas Stelzner, Vladimir Sivakov, Andreas Berger, Björn Hoffmann, Stefaan De Wolf, Christophe Ballif, **Dongfeng Zhang**, Johann Michler and Silke Christiansen. Structural, optical, and electrical properties of silicon nanowire solar cells. **Oral presentation** in the 3rd *IEEE International NanoElectronics Conference (INEC)*, 3th-8th, Jan. 2010, HongKong, China.
2. **Dongfeng Zhang**, Jean-Marc Breguet, Reymond Clavel, Silke Christiansen, Laetitia Phillippe, Ivo Utke and Johann Michler. *In-situ* nanotensile testing of nanowires. **Poster** in *Engineering Conferences International: Nanomechanical Testing in Materials Research and Development*, 11th-16th Oct. 2009, Barga, Italy.
3. Barbara Cousin, Mikhael Bechelani, Dongfeng Zhang, Rudy Ghisleni, William Mook, Johann Michler and Laetitia Phillippe. Mechanical properties of free-standing nanostructure using in-situ method. **Poster** in the 1st *Transalpine conference on nanoscience and nanotechnologies*. 27th-29th, Oct. 2008, Lyon, France.
4. **Dongfeng Zhang**, Jean-Marc Breguet, Reymond Clavel, Laetitia Phillippe and Johann Michler. *In-situ* nanomechanical testing of nanowires. **Oral presentation** in *2008 MRS Fall meeting*. 1th-5th Dec. 2008, Boston, USA.
5. Deyi Kong, Max Q.-H. Meng, **Dongfeng Zhang** and Tao Mei. Biomimetic design of two microsensor systems. **Oral presentation** in the 1st *IEEE Int. Conf. on Nano/Micro Engineered and Molecular Systems*. Jan. 2006, Zhuhai, China.
6. **Dongfeng Zhang**, Deyi Kong, Youngchun Tao and Jianhua Shan. Design of a silicon magnetodiodes array with self-compensation for temperature drift. **Proceedings** of the

2005 *IEEE Int. Conf. on information acquisition*. Hong Kong and Macau, China, 2005, 140-144.

7. **Dongfeng Zhang** and Deyi Kong. Research on designing and application of a magnetodiodes array chip. **Proceedings** of the 9th *Conf. of sensitive devices and transducers of China*. Xi'an, 2005, 547-549 (in Chinese).
8. Deyi Kong, Shengjun Hu, Tao Mei, Jianhua Shan, Lei Sun, **Dongfeng Zhang** and Lin Ni. Design and fabrication of a probe-based force sensor with six-degree freedom. **Proceedings** of the 9th *Conf. of sensitive devices and transducers of China*. Xi'an, 2005, 113-116 (in Chinese).

This page intentionally left blank